

ON THE EFFECTS OF INFLOW CONDITIONS ON THE WAKE OF WIND
TURBINE MODELS AND POROUS DISCS

A THESIS SUBMITTED TO
THE GRADUATE SCHOOL OF NATURAL AND APPLIED SCIENCES
OF
MIDDLE EAST TECHNICAL UNIVERSITY

BY

ABDELRAHMAN HISHAM AHMED SABRI HASSANEIN

IN PARTIAL FULFILLMENT OF THE REQUIREMENTS
FOR
THE DEGREE OF MASTER OF SCIENCE
IN
AEROSPACE ENGINEERING

JANUARY 2023

Approval of the thesis:
**ON THE EFFECTS OF INFLOW CONDITIONS ON THE WAKE OF
WIND TURBINE MODELS AND POROUS DISCS**

submitted by **ABDELRAHMAN HISHAM AHMED SABRI HASSANEIN** in
partial fulfillment of the requirements for the degree of **Master of Science in
Aerospace Engineering, Middle East Technical University** by,

Prof. Dr. Halil Kalıpçılar
Dean, Graduate School of **Natural and Applied Sciences** _____

Prof. Dr. Serkan Özgen
Head of the Department, **Aerospace Eng.** _____

Assist. Prof. Dr. Mustafa Perçin
Supervisor, **Aerospace Eng., METU** _____

Examining Committee Members:

Prof. Dr. Serkan Özgen
Aerospace Eng., METU _____

Assist. Prof. Dr. Mustafa Perçin
Aerospace Eng., METU _____

Assoc. Prof. Dr. Halil Ersin Söken
Aerospace Eng., METU _____

Prof. Dr. Metin Yavuz
Mechanical Eng., METU _____

Prof. Dr. Onur Baş
Mechanical Eng., TEDU _____

Date: 18.01.2023

I hereby declare that all information in this document has been obtained and presented in accordance with academic rules and ethical conduct. I also declare that, as required by these rules and conduct, I have fully cited and referenced all material and results that are not original to this work.

Name Last name : ABDELRAHMAN

HISHAM AHMED SABRI HASSANEIN

Signature :

ABSTRACT

ON THE EFFECTS OF INFLOW CONDITIONS ON THE WAKE OF WIND TURBINE MODELS AND POROUS DISCS

Hassanein, Abdelrahman Hisham Ahmed Sabri
Master of Science, Aerospace Engineering
Supervisor: Asst. Prof. Mustafa Perçin

January 2023, 95 pages

The study investigates the effect of two inflow conditions on the wake of a model wind turbine, namely, homogenous isotropic turbulence intensity and streamwise gust. For the effect of the freestream turbulence intensity, the wake of a porous disc with a comparable thrust coefficient was used to further highlight the differences in their wakes and decay characteristics. Results show that the wake of a wind turbine model has a faster decay rate than porous discs under both freestream turbulence intensities. In addition, the wake of both models was scaled to show a collapsing self-similar wake profile. Furthermore, the decay of the maximum velocity deficit was curve fitted using a logarithmic fit where the slope of the fit was used to provide a new way to quantify the wake growth. Consequently, this could be used as a basis for a new analytical model for the far wake of wind turbines. The effects of a streamwise gust with a triangular temporal distribution on the wake of a wind turbine model were studied for three tip speed ratios. Results reveal different wake evolutions for the three cases. Furthermore, the wake profiles under gust were scaled to collapse on self-similar profiles. Moreover, the wake of the wind turbine model at

a tip speed ratio of two and under triangular gust was compared to a top hat gust profile to investigate the effects of gust profiles. It was shown that the wake flow and, thus, the thrust generation mechanism of the turbine respond similarly during the rising edges of both gust profiles.

Keywords: Wake, Gust, Wind turbine, Wind tunnel, active grid

ÖZ

MODEL RÜZGAR TÜRBİNLERİNİN VE GÖZENEKLI DISKLERİN ARKASINDAKI AKIŞ KOŞULLARININ ETKİLERİ ÜZERİNE

Hassanein, Abdelrahman Hisham Ahmed Sabri
Yüksek Lisans, Havacılık ve Uzay Mühendisliği
Tez Yöneticisi: Asst. Prof. Mustafa Perçin

Ocak 2023, 95 sayfa

Bu çalışmada, iki farklı giriş akış koşulunun model rüzgar türbininin iz bölgesi üzerindeki etkileri incelenmektedir. Araştırmaya konu olan farklı akış koşulları, homojen izotropik türbülanslı akış ve akım doğrultusundaki sağanaklı akıştır. Serbest akış türbülansı etkisinin araştırılmasında, model türbin iz bölgesi ile benzer sürüklenme katsayısına sahip bir gözenekli disk modelinin iz bölgesi karşılaştırılmıştır. Bu sayede türbin ve diskin iz bölgesi akışlarının ve iz bölgesi sönümlenme karakteristiklerinin farkı net olarak ortaya konmuştur. Çalışılan farklı serbest akış türbülans seviyelerinde rüzgar türbininin iz bölgesinin disk iz bölgesine göre daha hızlı sönümlendiği gösterilmiştir. Buna ek olarak, iki modelin de iz bölgesi hız profillerinin uygun bir şekilde ölçeklendirildiği durumda öz-benzer bir akış profiline yakınsadıkları gösterilmiştir. Ayrıca, akış doğrultusundaki hız noksanlığının en büyük değerinin logaritmik bir düşüş gösterdiği ve bu değişime uydurulan eğrinin eğiminin iz bölgesi genişlemesini niceliksel olarak ölçebilmek amacıyla kullanılabilceği gösterilmiştir. Bu sonuç, rüzgar türbinlerinin uzak iz bölgelerindeki akışın elde edilmesi amacıyla kullanılabilcek bir analitik modele temel oluşturabilir. Türbin iz bölgesinin üçgen profile sahip bir sağanağa dinamik cevabı üç farklı uç hız oranı için çalışılmış ve üç farklı durum için iz bölgesinin farklı gelişimi gözlemlenmiştir. Üç farklı durumdaki iz bölgesi hız profillerinin öz-benzer profillerde çakışacak şekilde normalize edilebileceği gösterilmiştir. Türbin uç hız

oranı iki için, türbin iz bölgesinin üçgen ve kare biçimli sağanağa dinamik cevabı mukayeseli olarak incelenmiştir. İz bölgesi akış ve dolayısıyla da itki üretim mekanizması değişimlerinin sağanak profillerinin yükselen kenar bölümünde benzer olduğu gözlemlenmiştir.

Anahtar Kelimeler (İz bölgesi, Sağanak, Rüzgar türbini, Rüzgar tüneli, Aktif ızgara)

To my family

ACKNOWLEDGMENTS

I am deeply indebted to Asst. Prof. Mustafa Perçin for his invaluable support, guidance, and patience throughout my research journey. It has been an absolute privilege to work with him, and I am forever grateful for his unwavering support. I would also like to extend my heartfelt thanks to Prof. Dr. Oğuz Uzol for his valuable suggestions, guidance, and critical feedback.

I am grateful to Dr. Anas Abdulrahim for his guidance, support, and camaraderie throughout this process. I would like to express my appreciation to Tuğrul Akpolat and Buğrahan Öztürk for their support, guidance, and friendship from the start of the journey till its end. I am also grateful to my friends Mahdi Yazdanpanah and Mert Ali Andırın for their constant support and kindness.

I would like to extend gratefulness to Fatimah Safieh for her patience and endless support.

I would want to convey my appreciation to the ODTÜ RÜZGEM personnel for their support.

I would also like to thank the Scientific and Technological Research Council of Turkey (TÜBİTAK) for their assistance with project number 120M497 and the METU Center for Wind Energy (RÜZGEM). Their efforts are immensely valued.

Finally, I would like to thank my family and parents, Hisham Ahmed Sabri, Mona Abu el Khair, and my brothers Ahmed and Yousef. for their patience, support, and endless love. They are the backbone of my success.

TABLE OF CONTENTS

| | |
|--|-------|
| ABSTRACT..... | v |
| ÖZ..... | vii |
| ACKNOWLEDGMENTS | x |
| TABLE OF CONTENTS..... | xi |
| LIST OF TABLES | xiii |
| LIST OF FIGURES | xiv |
| LIST OF ABBREVIATIONS | xviii |
| LIST OF SYMBOLS | xix |
| 1 INTRODUCTION | 1 |
| 1.1 Understanding the Challenges of Wind Gusts | 2 |
| 1.1.1 Gust certification | 2 |
| 1.1.2 Gust generation in experimental facilities..... | 4 |
| 1.2 Overview of Active Grids | 6 |
| 1.3 Porous disc and wind turbine models | 8 |
| 1.4 Thesis Objective and Outline..... | 10 |
| 2 Methodology | 13 |
| 2.1 Wind Tunnel & Active grid | 13 |
| 2.1.1 Wind tunnel | 13 |
| 2.1.2 Active grid design | 14 |
| 2.1.3 Active grid validation..... | 16 |
| 2.2 Active grid and the wind tunnel control system | 22 |
| 2.2.1 Wind tunnel control..... | 24 |

| | | |
|-------|---|----|
| 2.2.2 | Active grid control | 25 |
| 2.2.3 | Additional measurements programs | 26 |
| 2.3 | Experimental details | 28 |
| 2.3.1 | Wind turbine | 28 |
| 2.3.2 | Porous Disc | 29 |
| 2.3.3 | Experimental setup for freestream turbulence intensity study..... | 30 |
| 2.3.4 | Experimental setup for the gusty inflow study | 32 |
| 2.3.5 | Experimental setup for the PIV measurements..... | 37 |
| 2.3.6 | Uncertainty analysis..... | 42 |
| 3 | Results | 47 |
| 3.1 | Effects of freestream turbulence intensity | 47 |
| 3.1.1 | Mean Wake Flow Field..... | 47 |
| 3.1.2 | Wake scaling and decay characteristics | 53 |
| 3.2 | Effects of a streamwise gust on the wake of a wind turbine | 58 |
| | Conclusion..... | 75 |
| | REFERENCES | 79 |
| | APPENDICES | 85 |
| A. | Appendix Title..... | 85 |

LIST OF TABLES

TABLES

| | |
|--|----|
| Table 1.1 Basic parameters for wind turbine classes [11] | 4 |
| Table 2.1 Design specifications of the active grid | 16 |
| Table 2.2 Comparison of active grid validation antecedent tests with turbulence intensity values presented by Hearst et al. [26]. | 18 |
| Table 2.3 Properties of the used wind turbine model. | 29 |
| Table 2.4 Porous disc properties | 29 |
| Table 2.5 The thrust coefficient of the test cases. | 31 |
| Table 2.6 PIV parameters | 38 |
| Table 2.7 The normalized uncertainty estimates for inflow turbulence cases | 43 |
| Table 2.8 The normalized uncertainty estimates for the hotwire measurements of the streamwise gust inflow..... | 44 |
| Table 2.9 The normalized uncertainty estimates for the PIV measurements of the streamwise gust inflow. | 44 |
| Table 2.10 The normalized uncertainty estimates for the PIV wake measurements under streamwise gust cases. | 45 |
| Table 2.11 The normalized uncertainty estimates for the dynamic thrust coefficient. | 45 |
| Table 3.1 Summary of the wake growth rate parameter A for porous disc and wind turbine model under different freestream turbulence intensities. | 55 |
| Table 3.2 Summary of the wake spread rate parameter k^* and the wake width intercept ϵ for porous disc and wind turbine model under different freestream turbulence intensities. | 58 |
| Table 3.3 Summary of the wake spread rate parameter A and the deficit intercept b for different tip speed ratio and different instances with the gust..... | 71 |

LIST OF FIGURES

FIGURES

| | |
|--|----|
| Figure 1.1 Example of extreme operational gust for $V_{hub}=25$ m/s, Class IA, and $D=42$ m [9]. | 4 |
| Figure 1.2. Schematic of the active grid developed by Makita (1991) [24]. | 8 |
| Figure 2.1. METU C3 open-return boundary layer wind tunnel facility at the center for Wind Energy Research (METUWIND). | 14 |
| Figure 2.2. Active grid in the closed configuration (on the left) and the open configuration (on the right). | 15 |
| Figure 2.3. The rendered drawing of the active grid integrated into the wind tunnel facility. | 15 |
| Figure 2.4. The experimental setup employed to validate the active grid. | 18 |
| Figure 2.5. Variation of dimensionless test section velocity with flaps angle: Measurements were made at motor fan speeds corresponding to 8.5 m/s (using pitot-static tube and hotwire) and 12.1 m/s when the blades were fully open and compared to the results of Knebel et al. [43]. | 20 |
| Figure 2.6. Variation of the total pressure loss coefficient according to the angle of the flaps: Measurements were made at motor fan speeds corresponding to 8.5 m/s and 12.1 m/s when the blades were fully open ($\alpha = 0^\circ$). | 21 |
| Figure 2.7. Variation of the test-section velocity on the left y-axis and turbulence intensity on the right y-axis according to the angle of the flaps: Measurements were made at motor fan speeds corresponding to 8.5 m/s when the blades were fully open. | 22 |
| Figure 2.8. Active grid - wind tunnel integrated control system connection diagram | 23 |
| Figure 2.9 The communication flow between programs. | 28 |
| Figure 2.10 The porous disc and the wind turbine model used in the experiment. | 30 |
| Figure 2.11 Static and total pressure profiles for both models under low freestream turbulence intensity. | 32 |

| | |
|---|----|
| Figure 2.12 Picture of a passive turbulence grid installed at the test section inlet. | 32 |
| Figure 2.13 The setup used to measure the gust profiles. | 34 |
| Figure 2.14 The produced gust profile in comparison with the scaled EOG. The right Y axis is the vane's angular positions in degrees. The Y-axis on the left is the normalized velocity. | 34 |
| Figure 2.15 a) shows the triangular temporal gust profile and the corresponding vane's angular position in time. b) shows the top hat temporal gust profile and the corresponding vane's angular position in time. | 35 |
| Figure 2.16 Streamwise velocity contour and transverse velocity contour for the triangular gust at different instances relative to the gust. | 36 |
| Figure 2.17 The variation of the thrust coefficient with tip speed ratio under a uniform inflow of 6.5 m/s. | 37 |
| Figure 2.18 PIV setup used for the wake measurements under uniform freestream turbulence intensity. | 39 |
| Figure 2.19 PIV measurements domain under different freestream turbulence intensities. | 40 |
| Figure 2.20 PIV setup used to characterize the inflow as well as to perform wake measurements. | 41 |
| Figure 2.21 PIV measurements domain for the inflow characterization under different gust inflow. | 41 |
| Figure 2.22 PIV measurements domain for the wake measurements under different gust inflow. | 42 |
| Figure 3.1 Velocity deficit contours in streamwise direction: (a) Wind turbine-low turbulence intensity, (b) Wind turbine-medium turbulence intensity, (c) Porous disc-low turbulence intensity, and (d) Porous disc-medium turbulence intensity. Dashed black lines mark the centerline of the rotor. | 49 |
| Figure 3.2. Vorticity contour in the out-of-plane direction (a) Wind turbine-low turbulence intensity, (b) Wind turbine-medium turbulence intensity, (c) Porous disc-low turbulence intensity, and (d) Porous disc-medium turbulence intensity. Dashed black lines mark the centerline of the wind rotor. | 50 |

| | |
|---|----|
| Figure 3.3. Streamwise velocity profile for the two models under different freestream turbulence intensities. | 52 |
| Figure 3.4. Out-of-plane vorticity profile for the two models under different freestream turbulence intensities. | 52 |
| Figure 3.5. A sketch that shows the scaling parameters on the wake profile..... | 53 |
| Figure 3.6. (a) Wind Scaled wake velocity profiles using wake half width and the maximum velocity deficit..... | 55 |
| Figure 3.7. The wake decay and wake deficit parameters for the two models at different downstream locations. | 55 |
| Figure 3.8. The variation of the standard deviation of the Gaussian velocity deficit profiles downstream of porous disc and wind turbine model and different freestream turbulence intensity..... | 57 |
| Figure 3.9. The normalized temporal gust profile of the triangular gust and top hat gust. The dashed black line indicates the instances selected to phase lock the PIV measurements. | 59 |
| Figure 3.10. The dynamic response of the thrust coefficient of the wind turbine model under triangular gust distribution for different tip speed ratios..... | 60 |
| Figure 3.11. The dynamic response of the thrust coefficient of the wind turbine model under triangular gust distribution and top hat gust distribution for the same tip speed ratio. | 61 |
| Figure 3.12. velocity contour in the streamwise direction for different tip speed ratios under triangular gust at different instances..... | 63 |
| Figure 3.13. Normalized out-of-plane vorticity contour for different tip speed ratios under triangular gust at different instances..... | 64 |
| Figure 3.14 Streamwise velocity profile for different tip speed ratios under triangular gust at different instances..... | 66 |
| Figure 3.15 The center wake velocity at $x/D=3$ for different tip speed ratios compared with the inflow velocity. | 67 |

| | |
|--|----|
| Figure 3.16 A sketch showing the parameters used to scale the wake of a wind turbine under streamwise gust. on the right the wind turbine's inflow velocity during the gust..... | 67 |
| Figure 3.17 Scaled wake profile of a wind turbine with different tip speed ratios at different instances relative to the gust and different downstream locations. | 69 |
| Figure 3.18 Variation of the maximum velocity deficit downstream for different tip speed ratios under triangular gust. | 70 |
| Figure 3.19 Variation of the wake half width downstream of the wind turbine model for different tip speed ratios under triangular gust..... | 70 |
| Figure 3.20 Streamwise velocity contour in the wake of a model wind turbine operating with a tip speed ratio of 2 under a top hat and a triangular gust profile. | 72 |
| Figure 3.21 Streamwise velocity profile for the same tip speed ratio under a triangular gust and a top hat gust at different instances. | 73 |
| Figure A.1 The graphical user interface of the wind tunnel control software. | 85 |
| Figure A.2 The Tunnel Real-time control software..... | 86 |
| Figure A.3 The PID loop within the Real-time tunnel control software..... | 87 |
| Figure A.4 The graphical user interface of the active grid motion control software for the random asynchronous modes. | 88 |
| Figure A.5 The graphical user interface of the active grid motion control software for the step gust. | 89 |
| Figure A.6 The graphical user interface of the Hotwire calibration software. | 90 |
| Figure A.7 The graphical user interface of the Hotwire measurement software. ... | 91 |
| Figure A.8 The graphical user interface of the Load measurement software. | 92 |
| Figure A.9 The graphical user interface of the Flaps monitoring software. | 93 |
| Figure A.10 The graphical user interface of the Automation software. | 94 |
| Figure A.11 Normalized stream wise and transverse velocity contour for top hat gust at different instances relative to the gust. | 95 |

LIST OF ABBREVIATIONS

ABBREVIATIONS

| | |
|----------|---|
| 2D2C PIV | Two-dimensional Two-component Particle Image Velocimetry |
| AEP | Annual Energy Production |
| EOG | Extreme Operational Gust |
| FOV | Field of View |
| HW | Hotwire Anemometry |
| LES | Large Eddy Simulation |
| Nd: YAG | Neodymium-Doped Yttrium Aluminum Garnet (Nd:Y ₃ Al ₅ O ₁₂) |
| PIV | Particle Image Velocimetry |
| TI | Turbulence Intensity |
| Ro | Rossby number |
| RE | Reynolds number |

LIST OF SYMBOLS

SYMBOLS

| | |
|------------|---|
| D | Disc/wind turbine model diameter |
| H | Test section height (m) |
| I_a | Ambient Turbulence Intensity |
| k^* | Wake spread rate |
| L | Length of the test section (m) |
| U_∞ | Freestream velocity |
| U_{hub} | Hub velocity |
| x,y,z | Coordinate system |
| σ | Standard deviation of the Gaussian velocity profile |
| ϵ | Wake width intercept |
| Ω | Vorticity in out-of-plane direction (s^{-1}) |
| ω_f | Angular velocity of the flap |

CHAPTER 1

INTRODUCTION

In 2021 the world witnessed a significant increase in wind-generated electricity to a record of 273 TWh Which, amounted to the highest growth among renewable power technologies [1]. Furthermore, climate change led to several global movements aiming toward a world with zero net emissions [2]. Although the wind capacity has seen a significant increase in response over the past decade, maintaining this growth will require significantly more dedication and effort. Among such efforts is building more durable wind turbines with long life cycles.

The durability and sustainability of wind turbines are essential factors in driving the levelized cost of electricity down [3], which, in turn, improves wind energy competitiveness without subsidies. However, wind turbines are subjected to extreme inflow conditions that hinder the durability of various components. Among such conditions is a gust, which can be defined as a short-term coherent disturbance in a turbulent wind field that manifests as a sudden increase in the mean velocity [4] [5]. Moreover, wind gusts can cause substantial fatigue loads through gust slicing, which occurs when the blade encounters the gust several times due to rotation. Additionally, gust slicing causes significant power production fluctuations, further burdening the electrical grid [8]. Moreover, length and time scales are important characteristics of gusts, as gusts with length scales of the same order of magnitude as the structure's characteristic length can cause severe damage [4]. Thus, arises the importance of understanding and simulating such phenomena and the effect it imposes on wind turbines. The IEC (International Electrotechnical Commission) defines simplified extreme gust profiles as standardized cases for the gust experienced by wind turbines. Although such simplified models do not fully represent the real-world gust due to the nature of complex terrains the gust evolves in [4], simulating such

conditions offers insight into the complex unsteady wake interaction as well as the unsteady blade responses. In addition, wind turbines operate within atmospheric boundary layers that come with an inherently high turbulence intensity which negatively impacts the power produced by the wind turbine [5]. The effects of turbulence intensity have been shown to affect power production by up to 2.4% under ambient turbulence intensities higher than 7% and by 3.5% for turbulence intensities lower than 5%. Furthermore, Turbulence intensity increases the extreme fatigue loading on the wind turbine blades, which significantly impacts the lifetime of wind turbines [6]. Hence, it is imperative to understand the effects of such inflow conditions on wind turbines and their wakes.

1.1 Understanding the Challenges of Wind Gusts

1.1.1 Gust certification

Due to the complex terrains surrounding wind farms, the gust impinging on commercial wind turbines has a complex spatial and temporal nature [4]. Nevertheless, it is a common practice to assume that a gust has canonical Mexican top hat temporal variation [9][10][11], as it is easier to identify critical wind speeds for a symmetrical gust variation. The IEC 61400-1 [11] defines several extreme operational conditions for wind turbines, among which is the extreme operational gust (EOG). It can be described as a pre-dip in streamwise velocity followed by a sudden steep increase in the velocity; after that, the velocity drops again with the same steepness followed by a slight increase to the initial velocity (will be discussed in detail below). Additionally, extreme directional change (EDC), as the name suggests an extreme change in the wind direction following a cosine variation. Furthermore, extreme wind shear (EWS) is a transient change of the velocity gradient across the rotor where it goes steep and then decreases again following a cosine temporal variation.

EOG is a classic example of the canonical Mexican top hat temporal distribution. The equations describing this gust are shown below [11].

$$V_{gust} = \min \left\{ 1.35(V_{e1} - V_{hub}); 3.3 \left(\frac{\sigma_1}{1 + 0.1 \left(\frac{D}{\Lambda_1} \right)} \right) \right\} \quad (1.1)$$

$$V(z, t) = \begin{cases} V(z) - 0.37V_{gust} \sin\left(\frac{3\pi t}{T}\right) \left(1 - \cos\left(\frac{2\pi t}{T}\right)\right) & \text{for } 0 \leq t \leq T \\ V(z) & \text{otherwise} \end{cases} \quad (1.2)$$

where $V(z) = V_{hub} \left(\frac{z}{z_{hub}}\right)^\alpha$; V_{e1} is the extreme wind speed with a recurrence period of one year ($V_{e1}(z) = 0.8 V_{e50}(z)$); V_{e50} is the extreme wind speed with a recurrence period of 50 years ($V_{e50}(z) = 1.4 V_{ref} \left(\frac{z}{z_{hub}}\right)^{0.11}$); D is the rotor diameter; $\sigma_1 = I_{ref}(0.75V_{hub} + 5.6)$. The turbulence scale parameter (Λ_1) can be expressed as follows:

$$\Lambda_1 = \begin{cases} 0.7 z & \text{for } z \leq 60m \\ 42 & \text{for } z \geq 60m \end{cases} \quad (1.3)$$

V_{ref} and I_{ref} are the reference values summarized in Table 1.1 for different wind turbine classes.

Table 1.1 Basic parameters for wind turbine classes [11]

| WIND TURBINE CLASS | | I | II | III |
|--------------------|---------------|------|------|------|
| V_{REF} (m/s) | | 50 | 42.5 | 37.5 |
| A | I_{ref} [-] | 0.16 | | |
| B | | 0.14 | | |
| C | | 0.12 | | |

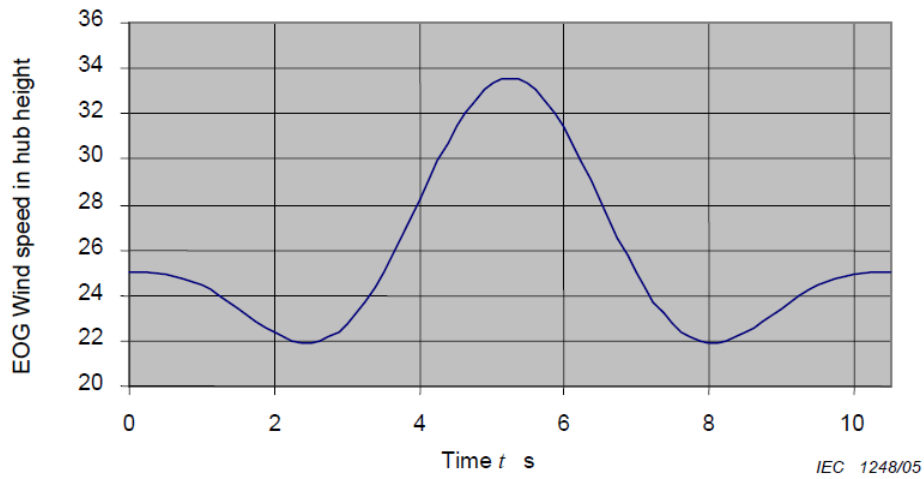


Figure 1.1 Example of extreme operational gust for $V_{hub}=25$ m/s, Class IA, and $D=42$ m [9].

1.1.2 Gust generation in experimental facilities

Wind tunnels are controlled environments as they operate with low turbulence intensity and uniform flows. However, real-life conditions are far more chaotic and involve different phenomena, such as atmospheric boundary layers, which are characterized by high turbulence intensities as well as extreme gust conditions. Several devices have been produced to generate such extreme conditions within the

wind tunnels. NASA pioneered the field of gust generation in experimental facilities in 1945, where a model airplane drove into a uniform air condition using a catapult and then encountered a transverse gust generated by a blower [12]. The work done there paved the road for understanding the gust effect and offered insight into the problem of gust generation experimentally.

Consequently, gust generation within experimental facilities took another turn where another approach was used, Vane-type gust generators were used yet again by NASA Langley. The vanes oscillated upstream of the test section, generating a sinusoidal transverse gust [13]. This method of gust generation produces 2D gust profiles with different amplitudes and frequencies [14]. This study emphasized the effects of reduced frequency as well as phase lag and amplitude attenuation of the generated gust. Active grids, on the other hand, are a far more intricate system that can produce a variety of complex flows, particularly gusty flows. For instance, Quin et al. [15] showed that streamwise gusts could be generated by fixing the angular position of the vertical vanes and oscillating the horizontal vanes. Moreover, Traphan et al. [16] showed that active grids could generate highly 3-dimensional gusts that vary across different reduced frequencies. In Addition, Neuhaus et al. [17] implemented a transfer function to generate Atmospheric gusts in a wind tunnel. This was simply done by varying the local blockage ratio through the deflection angle of a selected group of rods in a quasi-steady regime. In contrast, the other group of rods is varied to maintain a constant global blockage. This procedure is done several times with various configurations of selected groups. The resulting change in the mean velocity in response to variation of local blockage can be used later to generate the desired flow function. Results show that the desired velocity can be imprinted on the flow for low reduced frequencies and sufficiently high amplitudes. The desired velocity can still be implemented for high reduced frequency by increasing the amplitudes further due to the observed damping effect. A further interesting observation was that the positive and negative velocity increments imprint themselves differently on the flow. Furthermore, Shirzadeh et al. [19] produced extreme wind conditions comparable

with IEC 61400-1[11] standard using fan arrays. The results show how an array of fans can be used to produce extreme wind shear as well as extreme operational gusts.

1.2 Overview of Active Grids

Prior to using active grids, passive methods are used to increase the level of turbulence intensities or to generate boundary layers within wind tunnels. For instance, passive grids are employed to generate isotropic homogenous turbulent flows [20] [21]. However, the Reynolds number generated using passive grids is characterized by a lower Reynolds number than flows found in nature, typically $Re_\lambda \leq 10^2$ [21]. Several studies have tried to address this problem by grid jet injection [22] or having an array of jets [23]. However, they have not fared with the desired results. Until Makita [24] generated a high Reynolds number $Re_\lambda \sim 400$. This was achieved by using an active grid of 15 horizontal and 15 vertical bars with triangular vanes. The cross-section of the wind tunnel was $0.7 \times 0.7 \text{ m}^2$ and the inflow velocity was 5m/s. Furthermore, the protocol used for generating this turbulence is known as a single random mode. Figure 1.2 shows the schematic of the active grid used by Makita in 1991 [24]. Nevertheless, the isotropy of the flow produced later was far from ideal conditions. Several studies have followed trying to generate homogeneous isotropic turbulence and trying different algorithms. The modes of rotation are classified into three categories [21].

- Synchronous mode, where the magnitude angular velocity of the bars is constant. However, adjacent bars rotate in opposite directions.
- Single random mode, where the angular velocity of the bars is constant but each bar change direction after a random time independently.
- Double random mode, where the magnitude of the angular velocity of each bar change randomly (within a pre-set range), and the direction of rotation change after random time as well.

Moreover, Larssen et al. [25] and Hearst et al. [26] studied the effect of the Rossby number on the generated turbulence intensities from different protocols. Results show that increasing the Rossby number increases the turbulence intensities as well as the length scale. Additionally, results show that increasing the Rossby number results in increasing the anisotropy ratio, which suggests that there is a compromise to be made when trying to generate high turbulence intensities. This was also observed by Shet et al. [27]; in their study, they did a deep investigation of the isotropy of the flow generated by active grids. Results show that the double random mode is more effective than the single random mode in generating isotropic turbulence. In addition, the time where flaps reverse direction in double random mode should be limited in such a way that flaps do not cover more than 180° to avoid a spike in the power spectrum. They further added that high Rossby numbers do generate high turbulence intensities, but they come at the expense of isotropy of the generated turbulence. Active grids have also been used to generate atmospheric boundary layers. Celik et al. [27] have done so by varying the distribution of angular positions of the bars and oscillating the flaps to control the flow characteristics. Hearst et al. [29] generated atmospheric boundary layers with high turbulence. They did so by decoupling the horizontal and vertical rods; the vertical bars oscillated with different amplitudes to vary the effective local blockage. Thus, generating shear. The horizontal rods were actuated using the double random mode to generate high turbulence. Results show that decoupling the shear generation and the turbulence can generate the same shear profile with different turbulence intensity profiles.

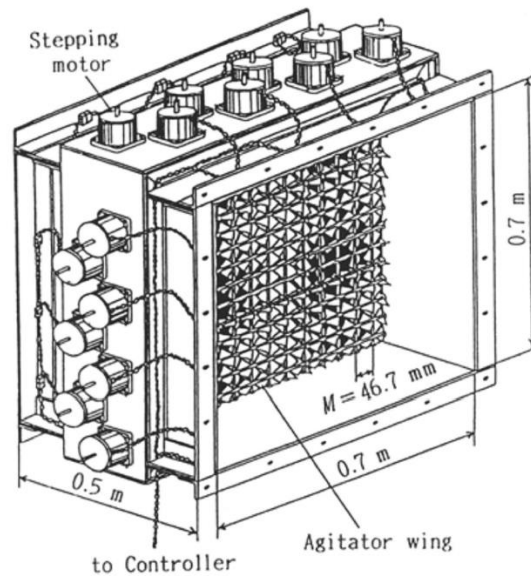


Figure 1.2. Schematic of the active grid developed by Makita (1991) [24]

1.3 Porous disc and wind turbine models

Several studies have examined the impact of various inflow conditions on the wake of wind turbines. Starting with field measurements, Fuertes et al. [30] studied the effects of several freestream turbulence intensities on the wake of 2.5 MW wind turbines by using two Doppler lidars mounted on the nacelle that use pulse scanning technology. Results show that the increase of freestream turbulence intensities enhances the wake recovery and yields a shorter wake length. In addition, using lidar technology, Bardal et al. [30] found that a 3 MW onshore wind turbine experienced a 1.2% rise in annual energy production under low shear and turbulent inflow conditions. As for wind tunnel studies, various studies have studied the effects of different inflow on wind turbine models. For instance, Zhang et al. [32] used a stereoscopic particle image velocimetry technique and a customized triple-wire system to study the effects of convective and neutral boundary layers on wind turbine wakes. The results showed that in the case of a convective boundary layer, the wake deficit was reduced. Moreover, Ozturk et al. [33] studied the effects of freestream

turbulence intensities on the wake of a wind turbine model as well as porous disc. Results were obtained using two-dimensional two-component particle image velocimetry. Results show that increasing the freestream turbulence increases the wake spread rate significantly for wind turbine models as well as porous discs. However, the porous disc failed to match the wake deficit of the wind turbine model in the case of low freestream turbulence intensity. On the other hand, the high freestream turbulence intensity case showed that the porous disc's wake deficit gets significantly close to the wake decay rate of wind turbine models. Aubrun et al. [34] conducted an experimental study under decaying isotropic turbulence and atmospheric boundary layer conditions and discovered that the porous disc reflects the characteristics of a wind turbine wake under atmospheric boundary layer conditions at three diameters downstream. Lignarolo et al. [35] used Particle Image Velocimetry in another investigation and discovered that by matching the diameter and thrust coefficient, the models produce equivalent wake expansion and energy extraction. Camp and Cal [36] investigated the mean kinetic energy transmission across the wind farm using wind tunnel testing using an array of model wind turbines and porous discs and discovered that the porous disc array could approximate the mean kinetic energy transport. Neunaber [37] also evaluated the wake characteristics of a porous disc and a model wind turbine under different inflow conditions with varied turbulence intensity levels and discovered that the porous disc and model wind turbine exhibit identical wake characteristics up to 4 diameters downstream. Nakashima et al. [38] studied the effects of tip speed ratio on the wake of wind turbines using LiDAR. Results show that a lower tip speed ratio has faster wake recovery than higher ones. Furthermore, Berger et al. [39] studied the effects of dynamic inflow due to gust. A 1.8 m diameter wind turbine was subjected to a uniform gust using an active grid. Dynamic load data were obtained using strain gauges as well as radially resolved axial velocities 2D LDA. Results show that the amplification of the induced velocity caused by gust causes reduced load amplitudes, thus, lowering the fatigue load. In addition, Yigili et al. [40] investigated the effects of transverse gust generated using a vane-type gust generator on the wake of the

porous disc as well as wind turbine models. Results were obtained using phase-locked two-dimensional two-component particle image velocimetry. Findings suggest that the difference between the wake of the porous disc and wind turbines is small in the near wake. However, the difference increases as the flow develops further downstream. El Makdah et al. [41] studied the effect of an axial gust on a low inertia rotor using time-resolved particle image velocimetry. Results show that the power output of the rotor increased under gust in comparison to steady-state power output. The results further indicate the tip and trailing edge vortices circulation increases during the gust.

1.4 Thesis Objective and Outline

This study aims to study the effects of different inflow conditions on the wake of wind turbines, namely, freestream turbulence intensity and gust. Furthermore, the near wake response of a wind turbine model under stream-wise gust is studied for three different tip speed ratios. Two-dimensional two-component (2D2C) particle image velocimetry (PIV) was used to characterize the effects of freestream turbulence intensity on the wake of a wind turbine model and a porous disc. A passive grid was used to generate the turbulence for the medium turbulence intensity case. EOG was generated using an active grid to understand further the effects of EOG on the wake of a wind turbine model. A single-wire hotwire was used to characterize the temporal variation of the EOG gust fully; then, the 2D2C PIV technique was used to characterize the spatial characteristics of the flow at selected instances relative to the gust event. The inflow was characterized at the rotor position 5.2 m downstream from the active grid. In addition, the wake measurements were conducted using Two-dimensional two-component (2D2C) particle image velocimetry (PIV) to cover a range from 0.35 diameters to 3.5 diameters downstream of the rotor at the selected time instances for the inflow.

Chapter 2 entails information about the active grid and the experimental facility. Furthermore, it explains the programs developed to obtain the measurements. Finally, it describes the wind turbine model and porous disc and gives information about the experimental setup. In addition, Chapter 3 discusses the results of the wake measurements under gust. Finally, the conclusions are stated in Chapter 4.

CHAPTER 2

Methodology

2.1 Wind Tunnel & Active grid

This subsection provides information about the wind tunnel where the measurements were conducted. It further entails the active grid design details. In addition, it will discuss the validation of the active grid.

2.1.1 Wind tunnel

Measurements were performed in the C3 open-return suction-type boundary layer wind tunnel located at the METU Center for Wind Energy Research (METUWIND), shown in Figure 2.1. This wind tunnel has a cross-sectional area of $1 \times 1 \text{ m}^2$, with an 8 m long test section made of Plexiglass to allow for optical access. The contraction ratio of the wind tunnel inlet is 1:5. Air suction is provided by using a 1.2 m diameter axial fan, which is driven by a 45 kW electric motor. The tunnel has a maximum inflow velocity of 25 m/s. The baseline turbulence intensity within the test section (without the active grid) is below 0.35%.



Figure 2.1. METU C3 open-return boundary layer wind tunnel facility at the center for Wind Energy Research (METUWIND).

2.1.2 Active grid design

The active grid used in this experiment is designed in the Makita style with a mesh-to-wind tunnel width ratio of $M/W=10$ to ensure a uniform flow. It consists of ten horizontal and ten vertical rods, with nine diamond-shaped flaps mounted in the center and two half flaps mounted on the edges of the rods. The flaps are made of aluminum (5000 series) and measure 94.75 mm in diagonal length and 2 mm in thickness. The rods are 1000 mm in length, 10 mm in diameter, and made of 1.2210 steel for added rigidity. The active grid chassis is made of aluminum (5000 series) and features sigma profiles made of aluminum attached to the outside to support the chassis and integrate it into the wind tunnel. The rods are actuated by 20 servo motors with a rated torque of 1.27 Nm, allowing them to rotate independently. The active grid has a minimum blockage of 21% in the open configuration (i.e., all flaps are wide open) and a maximum blockage of 89% (i.e., all flaps are closed), both of which are displayed in Figure 2.2. Table 2.1 summarises the design specifications of the active grid. Figure 2.3 shows the computer-aided drawing (CAD) of the integrated active grid in the C3 wind tunnel. A detailed study of the preliminary design of the active grid and the motor sizing is included in [42].

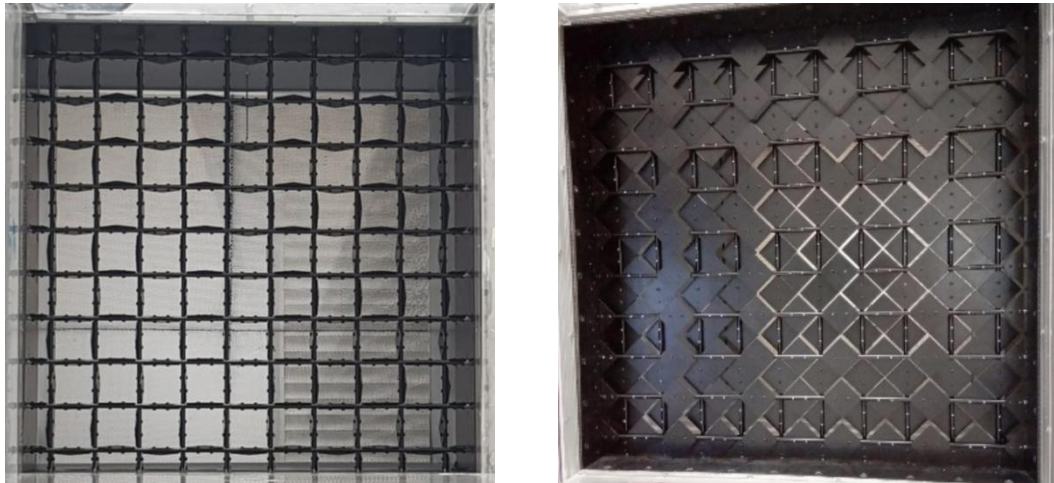


Figure 2.2. Active grid in the closed configuration (on the left) and the open configuration (on the right)

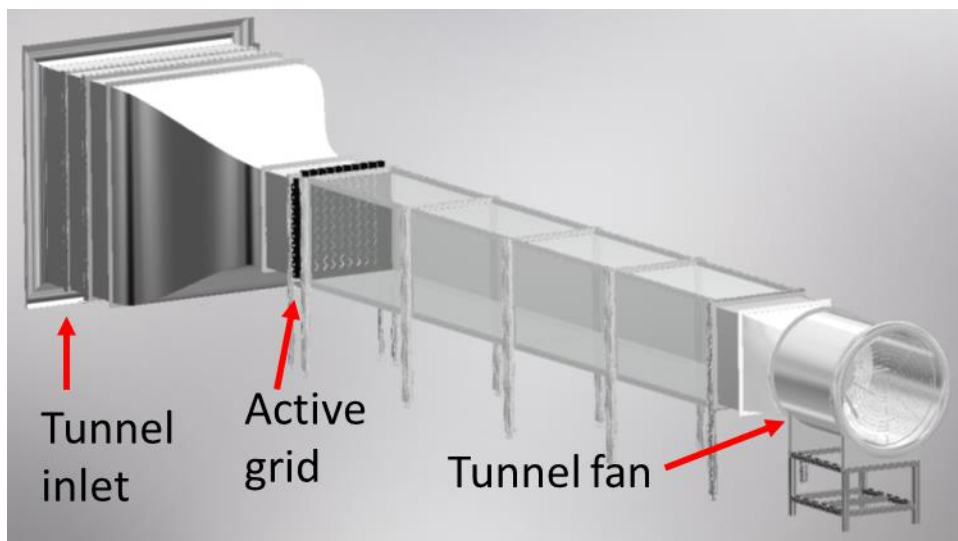


Figure 2.3. The rendered drawing of the active grid integrated into the wind tunnel facility.

Table 2.1 Design specifications of the active grid

| | |
|------------------------------------|-------|
| Minimum blockage [-] | 21% |
| Maximum blockage [-] | 89% |
| Rod diameter [mm] | 10 |
| Flaps thickness [mm] | 2 |
| Flaps diagonal length [mm] | 94.75 |
| Length of active grid's frame [mm] | 1120 |
| Active grid frame depth [mm] | 300 |
| Aluminum plate thickness [mm] | 15 |

2.1.3 Active grid validation

2.1.3.1 Protocols to generate high turbulence intensity

The active grid was validated by reproducing the result obtained from other active grids available in the literature. The experimental setup shown in Figure 2.4 was set up for the preliminary measurements made with a single wire hot wire sensor. In this setup, a pitot-static tube and a single-wire hot wire sensor are placed at a distance of $42.2M$ to be compared with Hearst et al. [26] as the measurements were conducted at a distance of $40M$ in his study (M represents the width of a pore of the active grid) from the active grid in the wind tunnel test section where $M \cong 100$ mm. The dynamic pressure values obtained from the pitot-static tube and the air density value obtained by using the temperature/humidity sensor and absolute pressure sensors were used to obtain the flow velocity in the tunnel test section. Calibration of the hot wire sensor was also carried out using velocity measurements made with a pitot-static tube in the tunnel to avoid large differences in freestream temperatures between the calibration and the actual measurement. Pitot-static tube measurements were made at 2 Hz data

acquisition frequency, and hot wire measurements were made at 10 kHz data collection frequency. The total measurement time was determined as 60 seconds.

$$T_q = \frac{(\langle u^2 \rangle + 2\langle v^2 \rangle)^{1/2}}{3^{1/2} \langle U \rangle} \quad (2.1)$$

Equation 2.1, taken from Hearst et al. [26], is used to calculate the resultant turbulence intensity using an X-wire hotwire sensor. In this equation, u and v are the velocities in the x and y directions of the measured turbulence velocities, and $\langle U \rangle$ refers to the temporal mean. The upwash velocity in the y direction and velocity in the z direction is also assumed to be equal to the upwash velocity in the y direction using the isotropic flow assumption, so the denominator in the above equation is multiplied by two and included in the calculation. A single hot-wire sensor was used to conduct the measurements. The single hot-wire sensor used in the current study measures the resultant of the two perpendicular velocity components acting perpendicular to the wire. Equation 2.2 is used to calculate the turbulence intensity for a single hot-wire sensor based on the assumptions that turbulence has an isotropic character at the measurement point and that the fluctuations in different directions generated by the active grid system are highly correlated in time. The factor in the denominator is for two velocity components so that the turbulence intensity values obtained from the single-wire sensor are taken into account in order to be compared with the overall average values presented by Hearst et al. [26].

$$T_{q,sw} = \frac{(\langle u^2 \rangle + \langle v^2 \rangle)^{1/2}}{2^{1/2} \langle U \rangle} \quad (2.2)$$

The comparison of the total turbulence intensity values obtained after these assumptions is presented in Table 2.2. As a result of this comparison, it is observed that approximate values are obtained in terms of turbulence intensity despite the strong assumptions. Although there are larger differences in some cases, the fact that the turbulence intensity changes according to the Rossby number ($Ro = U/\omega_f M$) and Re numbers are the same as those presented in the literature is considered a strong indicator that the active grid system works properly.

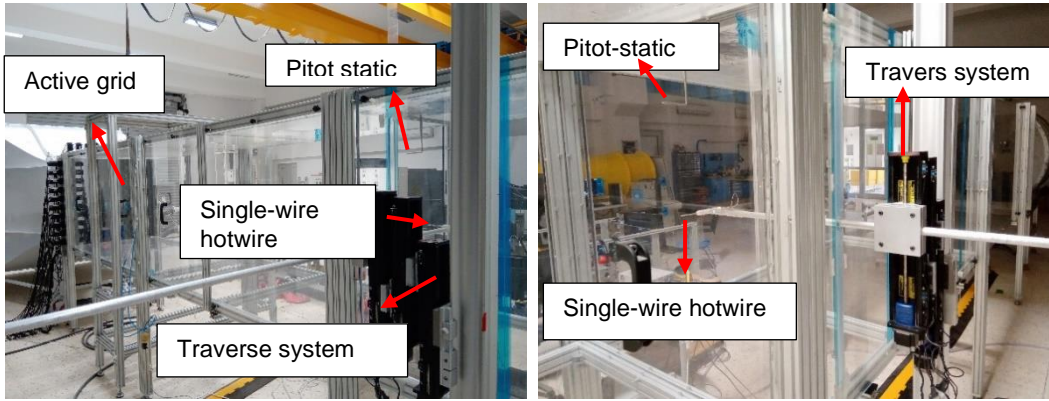


Figure 2.4. The experimental setup employed to validate the active grid.

Table 2.2 Comparison of active grid validation antecedent tests with turbulence intensity values presented by Hearst et al. [26].

| Test Case | Active Grid | Ro | $Re_M \times 10^3$ | $\Omega \pm \omega$ [rpm] | $T \pm t$ [s] | T_q |
|-----------|---------------------|------|--------------------|------------------------------|------------------|-------|
| 1 | Hearst et al. [26]. | 98 | 23.7 | 37.5 ± 22.5 | 2.1 ± 2.0 | 8.8 |
| | Current study | 98 | 23.6 | 25.85 ± 15.54 | 2.1 ± 2.0 | 10.1 |
| 2 | Hearst et al. [26]. | 122 | 29.5 | 37.5 ± 22.5 | 2.1 ± 2.0 | 8.7 |
| | Current study | 122 | 29.7 | 25.85 ± 15.54 | 2.1 ± 2.0 | 10.2 |
| 3 | Hearst et al. [26]. | 152 | 36.8 | 37.5 ± 22.5 | 2.1 ± 2.0 | 8.7 |
| | Current study | 152 | 36.8 | 25.85 ± 15.54 | 2.1 ± 2.0 | 11.3 |
| 4 | Hearst et al. [26]. | 182 | 44.1 | 37.5 ± 22.5 | 2.1 ± 2.0 | 8.6 |
| | Current study | 182 | 44.6 | 25.85 ± 15.54 | 2.1 ± 2.0 | 12.3 |

Table 2.2 (continued) Comparison of active grid validation antecedent tests with turbulence intensity values presented by Hearst et al. [26].

| | | | | | | |
|---|---------------------|-----|------|-------------------|---------------|------|
| 5 | Hearst et al. [26]. | 198 | 47.9 | 37.5 ± 22.5 | 2.1 ± 2.0 | 8.8 |
| | Current study | 198 | 48.0 | 25.85 ± 15.54 | 2.1 ± 2.0 | 13.3 |
| 6 | Hearst et al. [26]. | 20 | 23.2 | 180 ± 120 | 2.1 ± 2.0 | 7.4 |
| | Current study | 20 | 23.6 | 124 ± 82.5 | 2.1 ± 2.0 | 7.2 |
| 7 | Hearst et al. [26]. | 25 | 29.5 | 180 ± 120 | 2.1 ± 2.0 | 8.0 |
| | Current study | 25 | 29.7 | 124 ± 82.5 | 2.1 ± 2.0 | 7.6 |
| 8 | Hearst et al. [26]. | 32 | 36.8 | 180 ± 120 | 2.1 ± 2.0 | 8.3 |
| | Current study | 32 | 36.1 | 124 ± 82.5 | 2.1 ± 2.0 | 8.4 |

2.1.3.2 Blockage characterization

One of the most critical parameters in active grid systems is the changing blockage and the corresponding tunnel test section flow rate. For this reason, Knebel et al. [43] changed the fin angles in a quasi-static manner in the active grid system; they designed and measured the tunnel velocity corresponding to the angles of the flaps using a hotwire sensor placed in the middle of the test section. In this context, the attack angle of the flaps α was changed at a certain angle ranging between -20 degrees and 120 degrees. The measurements were conducted at 12 mesh lengths downstream. A similar experiment was carried out at two different tunnel flow rates in the RÜZGEM active grid system. By utilizing pitot-static tubes placed at 4.2m upstream and 41.4M downstream positions of the active grid, total, static, and dynamic pressure measurements were performed at these points. The angles of all flaps were changed at 4-degree intervals, and pressure data were collected for 50 s at a data acquisition frequency of 10 Hz for each flap angle. The pressure data were collected to characterize the pressure loss coefficient at each flap angle. Furthermore, a single-wire hotwire was used to characterize the velocity variation as well as turbulence intensity in response to the angular variations of the flaps. The sampling

frequency of the hotwire measurements was 10 kHz, and it was taken for 50 s. In these tests, the flow velocity in the tunnel test chamber was defined as the reference velocity (V_{ref}) when the wings were fully open and were set as 8.5 m/s and 12.1 m/s, respectively. In order to make a proper comparison, the measured test chamber velocity values are normalized with the test section flow velocity when the flaps are fully open. The variation of the dimensionless flow velocity in the test chamber according to the flaps angle is shown in Figure 2.5. In this graph, the zero-degree flaps angle ($\alpha=0^\circ$) corresponds to the case in which all flaps are fully open.

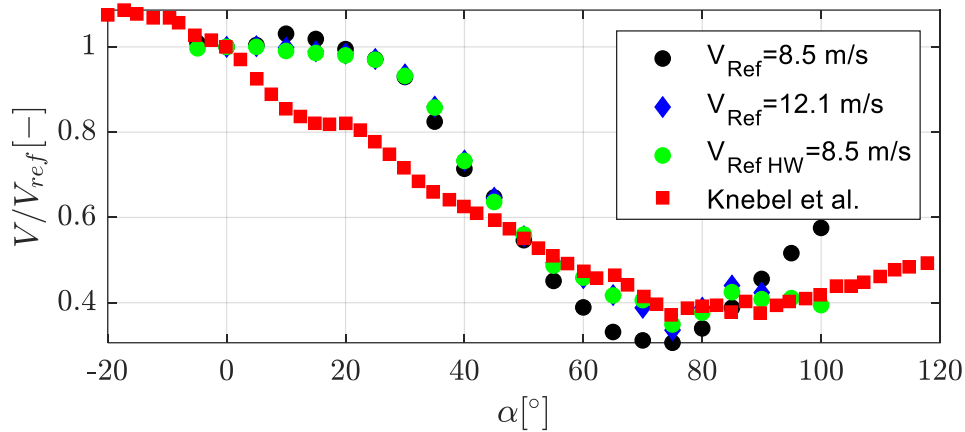


Figure 2.5. Variation of dimensionless test section velocity with flaps angle: Measurements were made at motor fan speeds corresponding to 8.5 m/s (using pitot-static tube and hotwire) and 12.1 m/s when the blades were fully open and compared to the results of Knebel et al. [43].

Experiments at different speeds give approximately identical speed drop values at the same blade angles. However, the characteristics of the open-loop suction-type wind tunnel used in this study are inherently different from the closed-loop open-test section wind tunnel used by Knebel et al.[43]. Furthermore, the total pressure loss created by the active grid at different flaps angles is expressed as the total pressure loss coefficient and calculated as follows.

$$C_{p,loss} = \frac{P_{t,inlet} - P_{t,test\ section}}{\frac{1}{2}\rho V_{test\ section}^2} \quad (2.3)$$

The total pressure loss coefficient at different angles is shown in Figure 2.6.

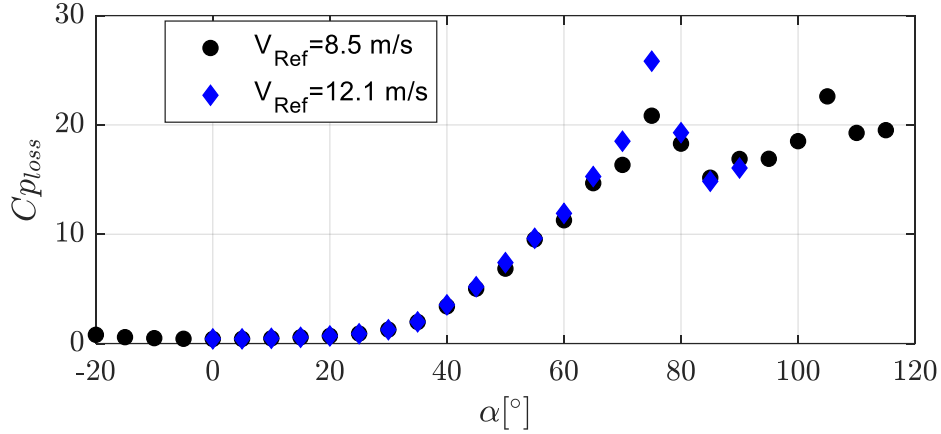


Figure 2.6. Variation of the total pressure loss coefficient according to the angle of the flaps: Measurements were made at motor fan speeds corresponding to 8.5 m/s and 12.1 m/s when the blades were fully open ($\alpha = 0^\circ$).

While the variation of the blade angle does not cause a significant loss in the first 20 degrees, it increases exponentially after this angle. This increase lasts up to approximately 75 degrees, then a relatively irregular change, first decreasing and then rising, is observed. A similar trend was found by Knebel et al. [43], as shown in Figure 2.6. In their active grid system, this irregular behavior is observed after 78 degrees. This is likely due to the efficiency of the tunnel fan dropping while operating under such high blockage conditions. The pressure loss coefficient can be used to estimate the effective angle for different active grid protocols. This could be helpful in an open-loop suction-type wind tunnel. Additionally, the velocity variation, as well as the turbulence intensity in response to the variation of the angular position, can be implemented in the form of a transfer function to tailor the flow. Knebel et al.[43] and Neuhaus et al. [17] used a similar method to tailor the flow and generate several temporal gust profiles. Figure 2.7 shows the variation of

the turbulence intensity and the normalized test-section velocity as a function of the angle of the flaps. One can see that the turbulence intensity starts increasing with the decrease in test-section velocity as the turbulence intensity. In the fully open position i.e., $\alpha = 0^\circ$, the turbulence intensity is 2%. The turbulence intensity increases sharply after $\alpha = 35^\circ$ to reach the maximum value of 30% at $\alpha = 75^\circ$. the turbulence intensity decreases again to reach 6%.

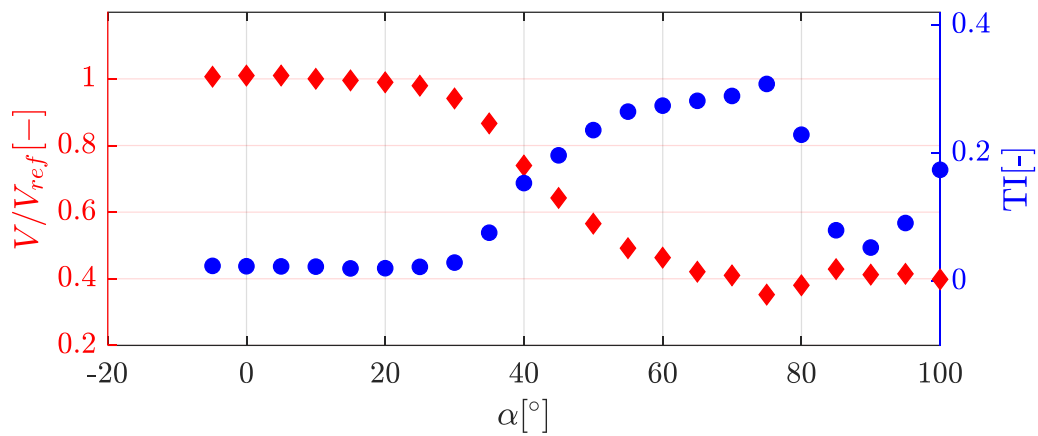


Figure 2.7. Variation of the test-section velocity on the left y-axis and turbulence intensity on the right y-axis according to the angle of the flaps: Measurements were made at motor fan speeds corresponding to 8.5 m/s when the blades were fully open.

2.2 Active grid and the wind tunnel control system

The active grid motor drivers are connected to a CompactRIO-9047 real-time controller via EtherCAT communication protocol. This allows for a swift and accurate control of the motors at high frequencies, which are needed for the active grid application. There are two modules mounted on the CompactRIO-9047 real-time controller; the first is an analog current input module, which is connected to the temperature & humidity sensor, the absolute pressure sensor, and the differential pressure sensor. The second is an analog current output module which is connected

to the fan driver. Figure 2.8 shows the connection diagram for the active grid-wind tunnel integrated control system.

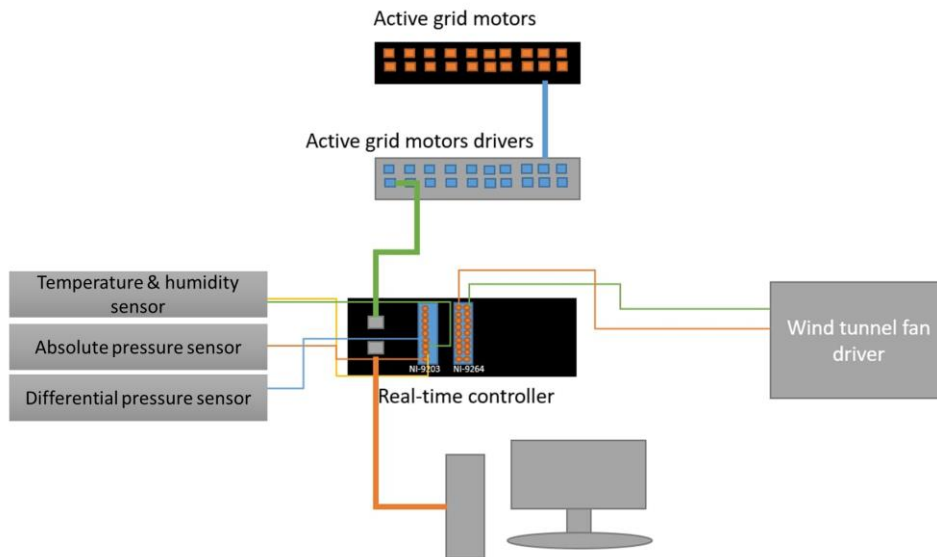


Figure 2.8. Active grid - wind tunnel integrated control system connection diagram

Additionally, two pitot-static tubes are connected to a pressure scanner which is connected to the wind tunnel operating computer. One of the pitot-static tubes is placed 1 m upstream of the grid, and the other is placed 4 m downstream of the grid. LabVIEW 2021 32 bits was used to develop the software that runs the wind tunnel, the active grid as well as additional acquisition software. The software are grouped in one LabVIEW project so that global variables can be shared between different programs running simultaneously. This feature allowed for the digital synchronization of several measurements and the use of several parameters in other codes.

2.2.1 Wind tunnel control

The aforementioned configuration allows for five different modes of operation of the wind tunnel.

- Fan RPM control

This mode corresponds to an open loop mode of control designed to rotate the wind tunnel fan at a constant rpm.

- Constant inlet velocity

This mode of control ensures that the specified velocity of the active grid inflow is constant.

- Constant inlet Reynolds number

This control mode ensures that the chosen Reynolds number of the active grid inflow is constant.

- Constant test-section velocity

This control mode ensures that the specified velocity within the test section is constant.

- Constant test-section Reynolds number

This control mode ensures that the specified Reynolds number within the test section is constant.

Error! Reference source not found. shows the user interface of the wind tunnel control software which is developed using LabVIEW 2021 32 bits. This program sends the inputs to the embedded code running on the real-time controller. The real-time controller code has a PID control loop that allows the aforementioned modes of control. The PID control loop is shown in Figure A.3. Furthermore, this software sends the tunnel parameters to be displayed or saved in the GUI of the tunnel and other software.

2.2.2 Active grid control

For the active grid software, there are three defined control modes: the "servo on" mode, which allows the servo motors to stay in a fixed position by applying the required amount of torque; the "servo off" mode, which allows the motors to be released by cutting the power from the driver; and the "position trigger" option, which enables the realization of motion protocols, that are also embedded in the LABVIEW software interface. The interface is capable of controlling each motor position, which can be used for blockage manipulation. The zero position of the motors (fully open configuration) was aligned using precise laser measurements. This position is embedded in the absolute encoder to ensure that the motor's zero position does not get lost. Additionally, the interface has different motion protocols, which are taken from the literature

- Single random asynchronous motion mode

In this protocol, each motor rotates at constant angular velocity for a random period of time, then rotates in the opposite direction with the same angular velocity for another random period of time. The random period of time has an upper and lower limit which can be prescribed in the software.

- Double random asynchronous motion mode

In this protocol, each motor rotates at random angular velocity for a random period of time, then turns in the opposite direction with a random angular velocity for another random period of time. The random period of time has an upper and lower limit which can be prescribed in the software. On the other hand, the angular velocity has a Gaussian distribution. The mean of the angular velocity and the standard deviation are required inputs in the software. The graphical user interface of the active grid motion control software for the random asynchronous modes can be seen in **Error! Reference source not found.**

- Step gust

In this protocol, the motors go from their prescribed initial positions to the prescribed final positions. However, there are three different time parameters to be defined, the first being the time between cycles which determines the time between each square pulse. This parameter determines the time between the flap's actuation from the initial position to the final position. There are two boolean buttons in the user interface. The first one is "Gust On," which triggers the flaps actuation and sends a trigger signal to other measurement programs -to be discussed in the upcoming subsection-. The second button is "Enable external trigger"; this button is used to enable another software to trigger the gust events. The graphical user interface of the active grid motion control software for the random asynchronous modes can be seen in Figure A.5.

2.2.3 Additional measurements programs

The measurements needed for this study required the development of additional programs, some of which are essential to the measurements; the rest serve the purpose of automating the measurement process in order to save time and eliminate human error.

2.2.3.1 Calibration of hot-wire anemometer

The software was developed to calibrate the hot-wire anemometer within the tunnel. The software does so by simply curve-fitting the velocity from the pitot tube with the measured voltage from the hotwire. The hotwire is connected to a multichannel CTA, which in turn is connected to a NI voltage analog input card mounted onto NI-DAQ that allows the software to acquire the voltage measured. The software sends the desired velocity to the real-time controller software, which ensures that the velocity measured by the pitot-static tube is reached. Consequently, the software waits until the velocity reaches a steady state, then starts collecting the voltage from the hot-wire with a frequency of 10 kHz for the 60 s, then moves to the second point.

The number of points required is an input in the software as well, and the distribution of the given velocity is logarithmic to ensure more points at lower velocities than at higher ones. The interface can be seen in Figure A.6.

2.2.3.2 Hot-wire measurement software

This software was developed specifically to measure the velocity using hotwire in parallel to the active grid motion. This is achieved by sending a digital trigger signal via a global variable that triggers the motion of the active grid and the signal acquisition of the hotwire. The software uses the calibration polynomial equation from the hotwire calibration software. The interface can be seen in Figure A.7.

2.2.3.3 Load cell measurement software

This software was developed to enable taking synchronized load measurements with the active grid motion. This was achieved using the same digital trigger signal used for the hot-wire measurement software. This software is compatible with ATI load cell FT17967, which is connected to a NI voltage analog input card mounted to NI-DAQ that allows the software to acquire the voltage measured. This voltage is converted to forces using the calibration file matching the aforementioned load cell. The interface can be seen in Figure A.8.

2.2.3.4 Flaps monitoring software

This software allows the monitoring of the selected rod's angular position as well as angular velocity. Additionally, it allows the user to monitor the tunnel parameter, such as the inlet velocity as well as the test section velocity. This software saves the values either by use of the digital trigger or the save button in the interface. The interface can be seen in Figure A.9.

2.2.3.5 Measurements automating software

This software allows for the automating process of the hotwire measurements. The software first sends a trigger signal to the active grid control software that should have the external trigger enabled. Followingly, it sends another trigger to stop the measurements after the prescribed time, which depends on the frequency as well as the number of samples in the aforementioned programs. The software then proceeds to move the traverse with a prescribed distance. Subsequently, the software triggers the measurements again and the loop runs until the number of required traverses is achieved. The interface can be seen in Figure A.10. Figure 2.9 elucidates how the coded programs communicate with each other.

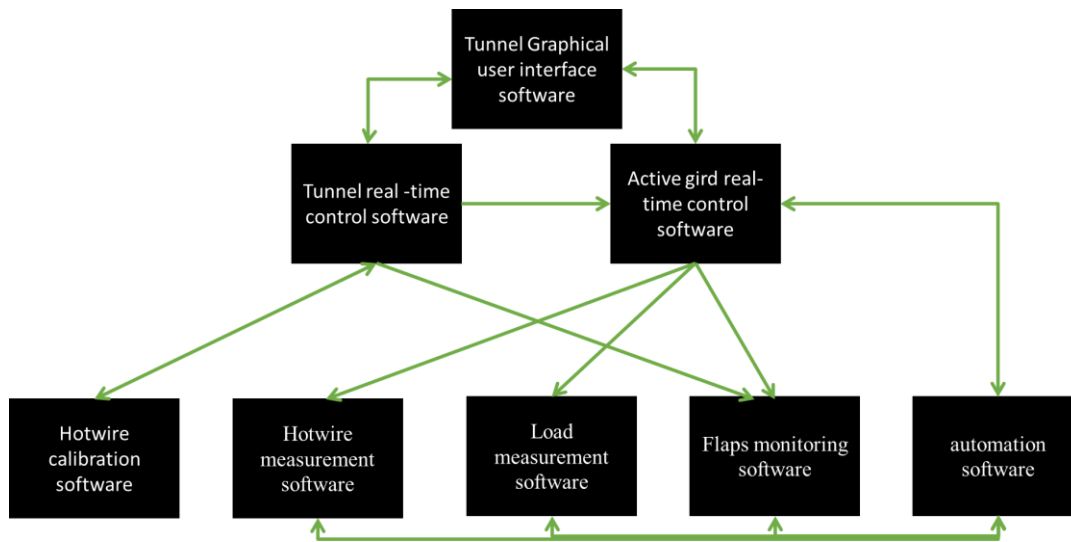


Figure 2.9 The communication flow between programs.

2.3 Experimental details

2.3.1 Wind turbine

The wind turbine model used in this experiment has a diameter of 120 mm. The blades of the wind turbine model are fabricated from aluminum and have a constant

thickness of 0.5 mm. Furthermore, the blades have a root twist of 22° that varies to reach 15° at the tip. The wind turbine model runs employing a brushless DC motor which is controlled by an Arduino controller. The motor is placed within the nacelle for angular velocity control. Both the nacelle and the hub were printed using a 3D printer with PLA+ filament. Table 2.3 elucidates the wind turbine properties.

Table 2.3 Properties of the used wind turbine model.

| | |
|--------------------|-------------------------------------|
| Radius | 60 mm |
| Hub Radius | 5.4 mm |
| Taper distribution | Linear |
| Material | Aluminum |
| Twist Angle | 15° - 22° root to tip |

2.3.2 Porous

Disc

The porous disc utilized in this experiment is a radially non-uniform porous disc. The reason behind the non-uniformity of the disc is to replicate the twist as well as the taper ratio of a wind turbine model. The porous disc has a diameter of 120 mm, a thrust coefficient of 0.64, and an axial induction factor of 0.2. Table 2.4 summarizes the porous disc properties, and Figure 2.10 shows the models used in the experiments.

Table 2.4 Porous disc properties

| | |
|------------|-------------|
| Radius | 60 mm |
| Hub Radius | 5.4 mm |
| Porosity | Non-uniform |
| Material | Plywood |



Figure 2.10 The porous disc and the wind turbine model used in the experiment.

2.3.3 Experimental setup for freestream turbulence intensity study

In order to study the effects of freestream turbulence intensity on the wake of wind turbine models as well as porous discs, two inflow conditions were selected. The first is under uniform inflow, where the inflow Reynolds number is kept constant at 100k, and the freestream turbulence intensity is 0.5%. This case is labeled as low ambient turbulence intensity (LTI). The second is under homogenous isotropic-generated turbulence by using a passive grid. The ambient turbulence intensity generated is 4.5%, and the inflow Reynolds number is kept at 100k. This case is labeled as medium ambient turbulence intensity (MTI). Figure 2.12 shows the used passive grid integrated within the C3 wind tunnel. The inflow was characterized using single-wire hotwire measurements with a 10 kHz sampling frequency for a duration of 30 s. The integral length scale in the MTI cases is estimated to be 0.071m. The thrust coefficient of the resulting four cases is kept constant. This was achieved by varying the tip speed ratio of the wind turbine model. The resultant tip speed ratio is 1.9.

The thrust was obtained by use of a control volume analysis and force sensor measurements. For the control approach, a Pitot-static tube was traversed vertically

at a downstream distance of $x=6.2D$ and $x=6.7D$ for the wind turbine model and porous disc, respectively, to measure the velocity as well as the static pressure. The static pressure and the total pressure profiles for both models can be seen in Figure 2.11. The pitot-static tube within the test section (mentioned in sec. 2.2.1) was used to achieve the inflow velocity and the static pressure. For the direct measurement of thrust, an ATI Omega load cell was used. Consequently, the thrust coefficient was calculated using the following equation.

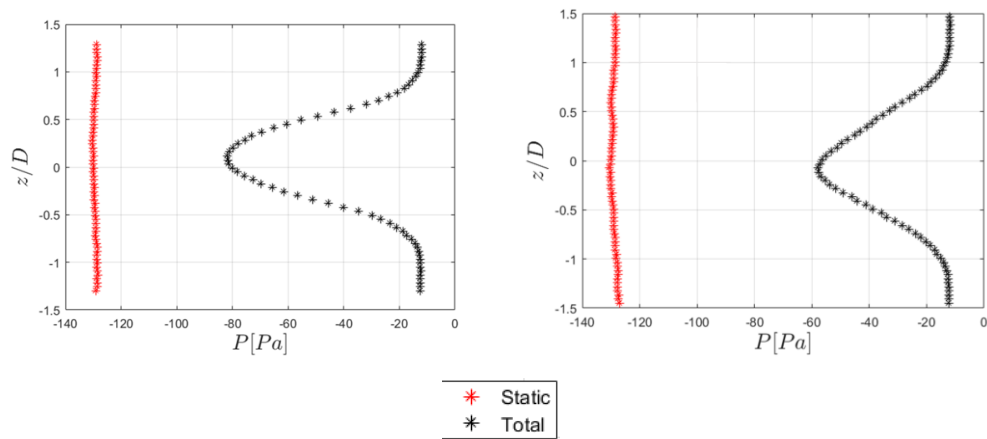
$$C_T = \frac{T}{\frac{1}{2}\rho U_\infty^2 A} \quad (2.4)$$

where T is the thrust force of the rotor, ρ is the density of air, U_∞ is the inflow velocity, and A is the area of the rotor. The thrust coefficient of the porous disc and the wind turbine model under both inflow conditions are summarized in Table 2.5.

Table 2.5 The thrust coefficient of the test cases.

| Test Cases | <i>Thrust Coefficient (C_T)-(loadcell)</i> | <i>Thrust Coefficient (C_T)</i> |
|------------|---|--|
| WT-L_TI | 0.6 | 0.51 |
| WT-M_TI | 0.6 | 0.51 |
| PD-L_TI | 0.62 | 0.59 |
| PD-M_TI | 0.59 | 0.59 |

The discrepancies between the thrust from the control volume approach and the loadcell measurements are likely to arise from the interaction between the tower wake and disc wake, which cannot be completely eliminated due to the inherent physical requirements of the experiment.



PD_L_TI

WT_L_TI

Figure 2.11 Static and total pressure profiles for both models under low freestream turbulence intensity.

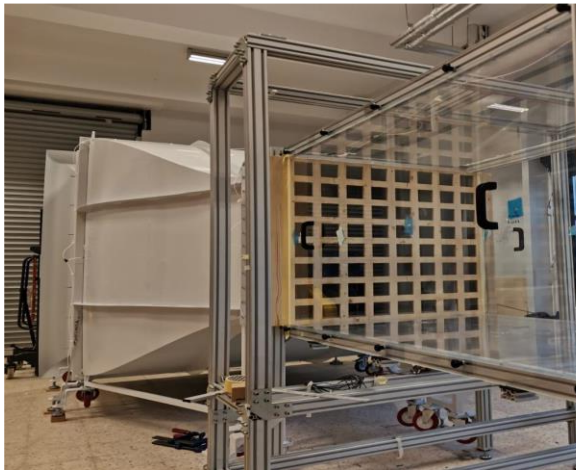


Figure 2.12 Picture of a passive turbulence grid installed at the test section inlet.

2.3.4 Experimental setup for the gusty inflow study

To generate the inflow gust, the wind tunnel controller was set to operate at constant RPM that corresponds to an inflow velocity of 6.5 m/s to the active grid. The vane's angular positions were varied from 52° to 31.5° where adjacent flaps will be pointing in opposite directions to avoid flow directionality. The angular positions were chosen

based on the blockage characterization in section 2.1.3. The vanes have a uniform angular distribution of local blockage. This allows the flow to be uniform except for regions close to the wall. Consequently, a single-wire hot-wire sensor was placed 5.2 m (i.e., $x/M=52.2$) downstream of the active grid and 500 mm from the bottom wall. The sampling frequency of the hot-wire probe was 1 kHz, and 600k samples were taken. This corresponded to 120 Gust events in the case of the triangular gust temporal distribution (discussed in the next paragraph). Figure 2.13 shows the setup used to take the measurements. In addition, phase-locked two-dimensional two-component (2D2C) particle image velocimetry (PIV) was used to characterize the spatial evolution of the gust upstream of the wind turbine model and to perform the wake measurements.

The temporal profile of the EOG gust was simplified to a triangular gust with a matching gust ratio. The gust selected is representative of a gust incident on a class A-I commercial HAWT with a diameter of 90 m and a hub height of 100 m. The width of the produced gust is 2s. This value is in the same order of magnitude as the EOG gust of a period of 4s. The reason behind the discrepancy is that the temporal profile of the EOG includes a pre-dip of the gust, which was eliminated in the simplified case. Figure 2.14 shows the produced gust profile with the scaled EOG profile. The time between consecutive gust events was set to 4 s to ensure that the flow returned to a steady state before perturbing the flow again. The study includes a top hat temporal distribution with a 5s width as well. The time between two consecutive gust events in this temporal distribution is set to be 5 s to ensure symmetry and that a steady state is achieved before flow perturbation. The aim behind studying such a profile is to first understand the effects of such temporal distribution on the wake of the wind turbine model. Furthermore, it will be used to compare the effects of gust profiles with a matching rise and dip time on the wake of the wind turbine model. Hence, the instances chosen to phase-lock the particle image velocimetry measurements in both gust profiles correspond to each other. In other words, they are at the same time relative to the start of the gust event. Figure 2.15 shows the temporal distribution of the two gust profiles for 20 seconds. The

dashed lines show the selected instances to phase-lock the inflow as well as the wake measurements.

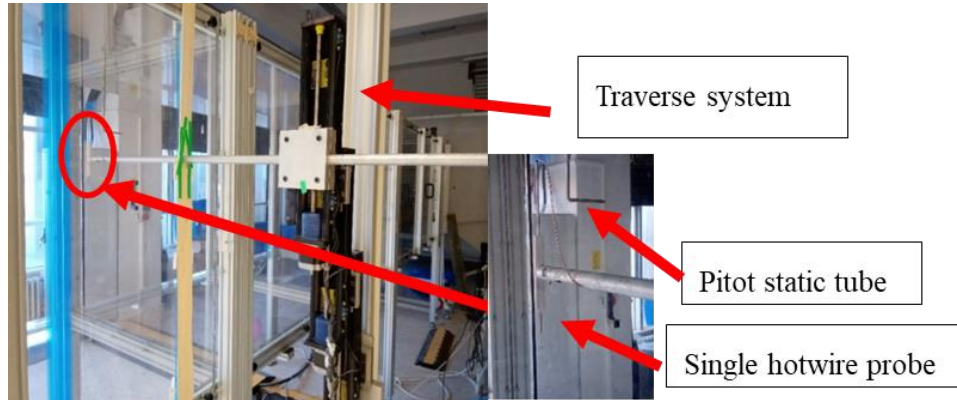


Figure 2.13 The setup used to measure the gust profiles.

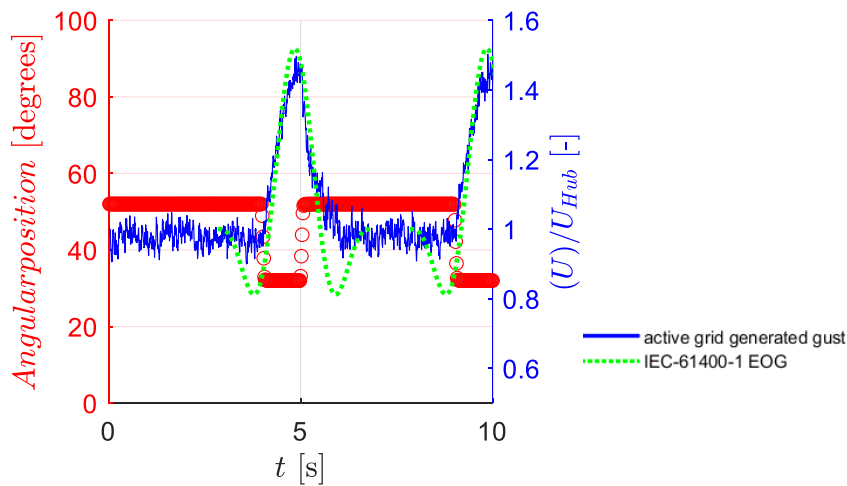
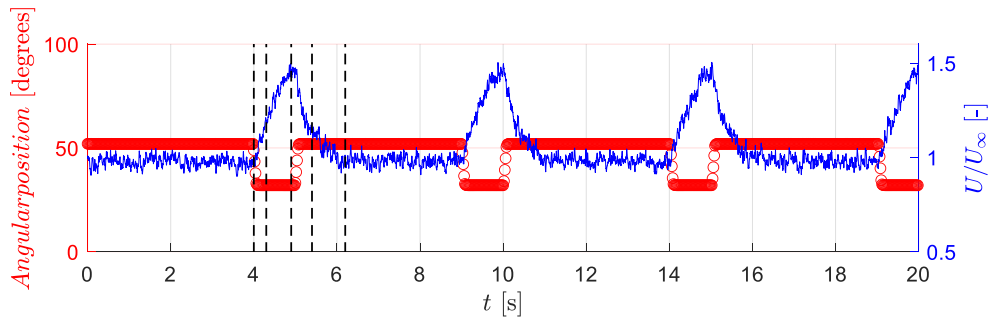


Figure 2.14 The produced gust profile in comparison with the scaled EOG. The right Y axis is the vane's angular positions in degrees. The Y-axis on the left is the normalized velocity.

a)



b)

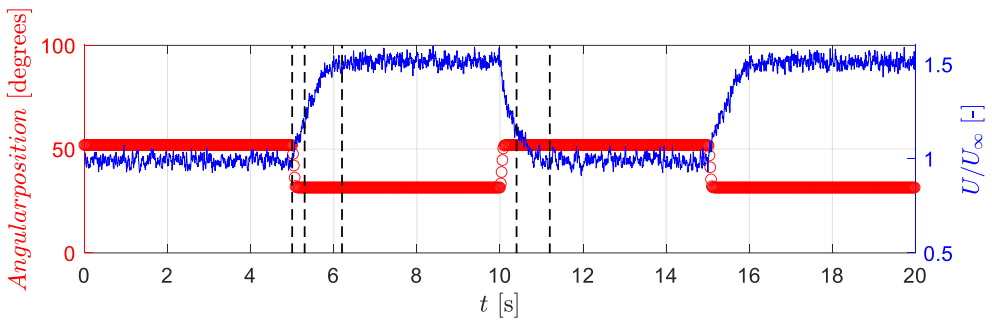


Figure 2.15 a) shows the triangular temporal gust profile and the corresponding vane's angular position in time. b) shows the top hat temporal gust profile and the corresponding vane's angular position in time.

The normalized streamwise and transverse velocity fields for the triangular gust at the prescribed instances are presented in Figure 2.16. In addition, Figure A.11 shows the streamwise and transverse velocity contours for the top hat gust. The field of view of the measurements covers from $-1D$ to $-0.6D$ relative to the position of the rotor in the streamwise direction and from $-0.8D$ to $0.8D$ in the vertical direction. Consequently, one can see that the two generated gust profiles by the active grid are pure streamwise gusts without transverse components, which were achieved by having adjacent flaps pointing in opposite directions and having the measurements at a sufficient distance downstream of the active grid. Furthermore, the resulting generated gust profiles have a gust ratio of $GR=1.5$. where $GR=U/U_{\infty}$.

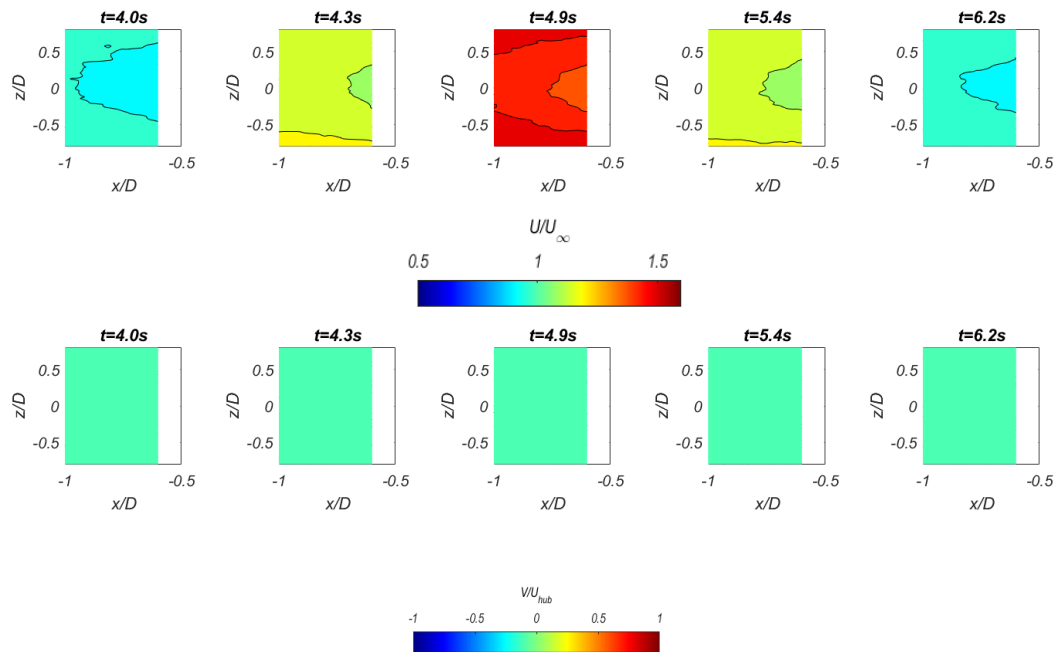


Figure 2.16 Streamwise velocity contour and transverse velocity contour for the triangular gust at different instances relative to the gust.

The effects of streamwise gust with a triangular temporal distribution on a wind turbine were studied using different tip speed ratios corresponding to three comparable thrust coefficients, namely, $C_{T \text{ TSR}=1.0}=0.905$, $C_{T \text{ TSR}=2.0}=0.885$ and $C_{T \text{ TSR}=3.1}=0.812$. An ATI load cell was placed at the bottom of the tower to measure the thrust of the wind turbine with the tower effects. The selected tip speed ratios are shown in Figure 2.17. The wind turbine was operated with a tip speed ratio of 2 under the top hat gust profile to be compared with the corresponding triangular gust case at the same tip speed ratio. The PID controller of the wind turbine was set to operate at a constant angular velocity under gust inflow. Additionally, the load cell was used to measure the dynamic effects on the thrust coefficient. The acquisition frequency was set to 10 kHz and the data were collected for 100 s. A moving average filter was applied with a window size of 50 ms and the force data was then averaged for 20 gust events.

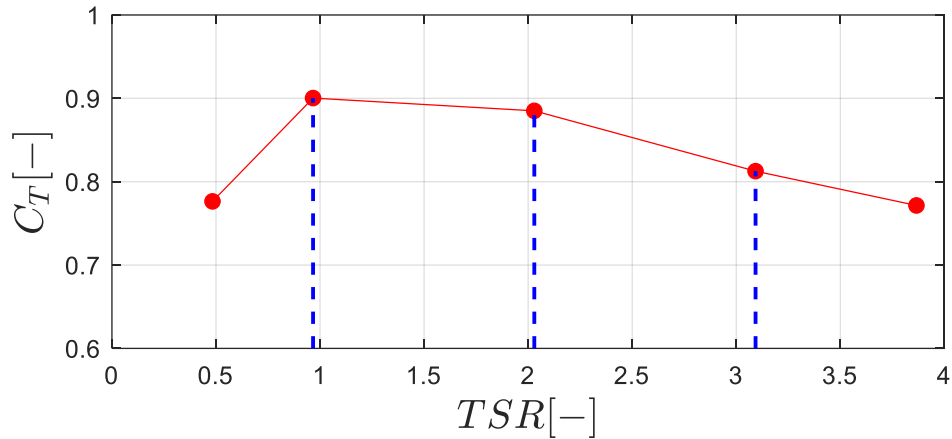


Figure 2.17 The variation of the thrust coefficient with tip speed ratio under a uniform inflow of 6.5 m/s.

2.3.5 Experimental setup for the PIV measurements

Two-dimensional two-component (2D2C) particle image velocimetry (PIV) was used for the two measurement campaigns. The same setup was used for both at different locations from the tunnel inlet. However, their field of view is different, as will be discussed in the following paragraphs. For the wake measurement under gust inflow, a NI digital output module was used to trigger the pulses at the desired phase. The Dantec Dynamics timer box is used to synchronize the timing of the laser and the camera. On the other hand, the New Wave Solo PIV Nd: YAG laser produces a laser beam that gets reflected in a mirror and goes through a spherical and a cylindrical lens to be converted into a laser sheet of 2 mm thickness in the flow field. The Phantom v641 high-speed camera and Nikon-NIKKOR 60 mm lens are used to take pictures of the tracer particles, and the DynamicStudio® software processes and analyzes these images to determine the velocity of the flow field. Table 2.6 details the PIV parameters.

Table 2.6 PIV parameters

| | | |
|-------------|-------------------------|---|
| | Laser type | Nd: YAG |
| | Manufacturer | New Wave Research |
| | Model | Solo 120XT |
| Laser Sheet | Maximum energy | 120mJ/pulse |
| | Wavelength | 532 nm |
| | Thickness | ≈ 2 mm |
| | Mirrors | Dielectric Mirror, 532 nm |
| Optics | Spherical Lens | Plano-convex, 750 mm FL |
| | Cylindrical Lens | Plano-concave, -12.4 mm FL |
| | Sensor type | CMOS |
| | Sensor resolution | 2560×1600 <i>pixel</i> ² |
| | Sensor size | 25.6×16.0 <i>mm</i> ² |
| Camera | Pixel pitch (size) | 10 μm |
| | Depth | 12 bits |
| | Maximum repetition rate | 1400 fps @ Full resolution 2500 fps @ 1920×1080 |
| | Internal memory buffer | 16 GB |
| | Manufacturer | Nikon |
| Camera Lens | Focal length | 60 mm |
| | f# (aperture) | 2.8 |
| | Type | Fog |
| Seeding | Nominal diameter | ≈ 1 μm |
| | Seeding generator | Safex Fog generator |

2.3.5.1 Freestream turbulence intensity

Wake measurements under different levels of freestream turbulence intensity were taken downstream of the wind turbine model and the porous disc, covering a range from 0.5 to 7.0 times the diameter of the turbine. The CAD drawing in Figure 2.18 shows the layout of the various components in the system. Multiple fields of view were used to capture the wake, with overlap between adjacent fields to ensure a more accurate measurement, as shown in Figure 2.19. The time between pulses during image acquisition was $80 \mu\text{s}$, and the frequency of the acquisition was 10 Hz. One thousand image pairs were taken for each window to obtain a total averaged vector field. The locations of the models used are shown in the figure as a blue rectangle.

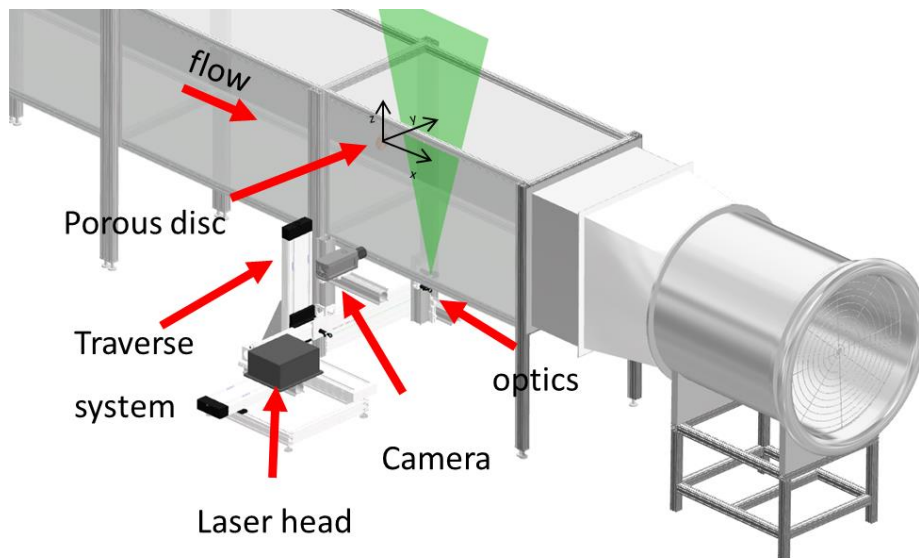


Figure 2.18 PIV setup used for the wake measurements under uniform freestream turbulence intensity.

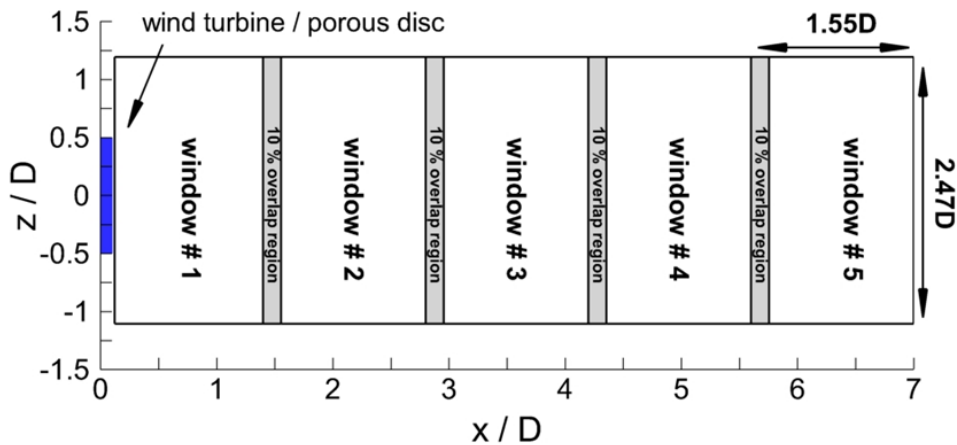


Figure 2.19 PIV measurements domain under different freestream turbulence intensities.

2.3.5.2 Gust inflow

A series of experiments were conducted to measure the wake of a wind turbine model stream-wise temporal gust profiles. The rotor was placed 5.2m (52.2M) downstream of the active grid. Three fields of view were used to capture the flow field, with overlap between the fields to improve accuracy. The domain of the measurements covered a range from 0.35 to 3.5 times the diameter of the turbine downstream of it. The measurements were taken for five instances shown in Figure 2.15. A total of 75 image pairs were taken for each phase at every field of view to obtain an averaged vector field of the wake for each phase. The time between image acquisition pulses was 105 μ s. The location of the wind turbine model is shown in Figure 2.20, and the figure also shows the layout of the various components used in the system. The domain of the PIV measurements for the inflow and wake measurements is illustrated in Figure 2.21 & Figure 2.22, respectively.

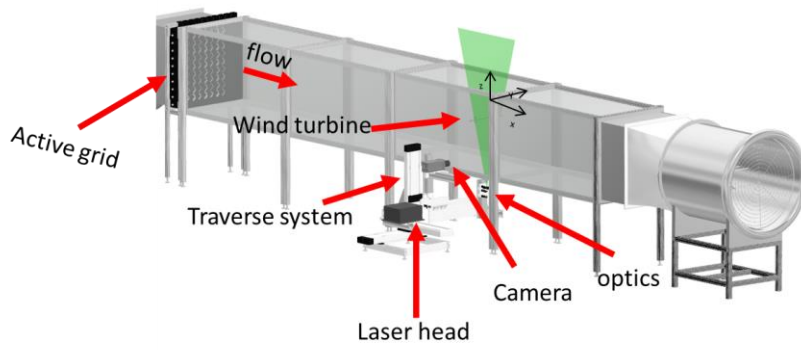


Figure 2.20 PIV setup used to characterize the inflow as well as to perform wake measurements.

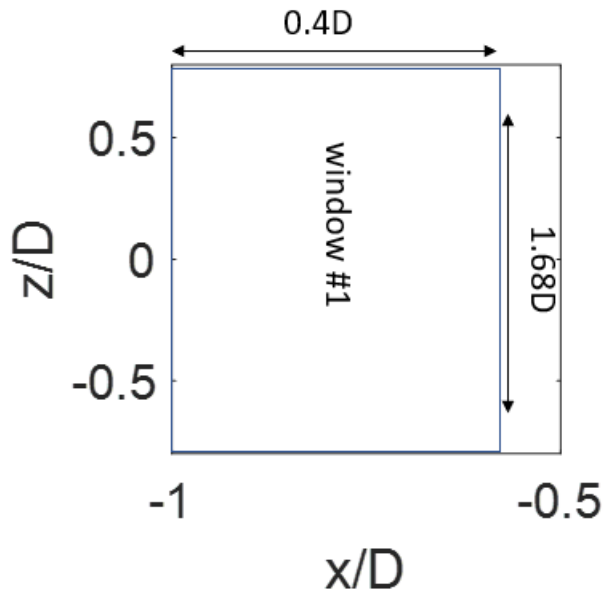


Figure 2.21 PIV measurements domain for the inflow characterization under different gust inflow.

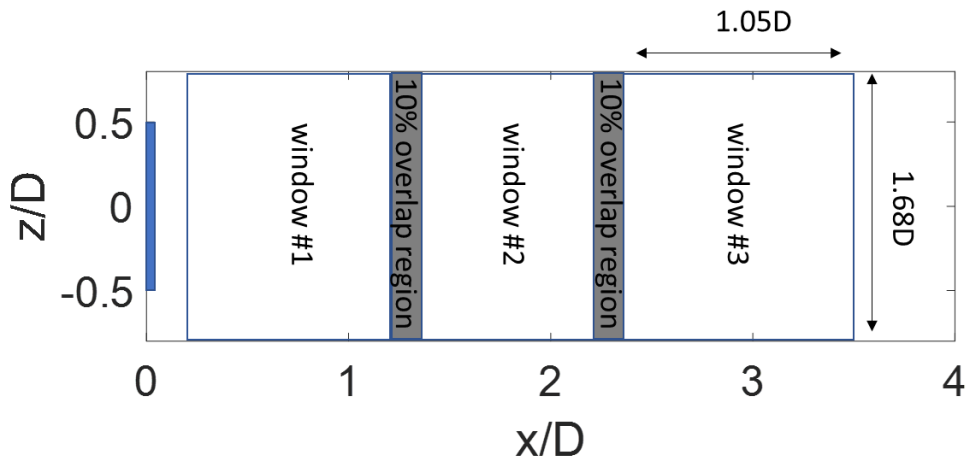


Figure 2.22 PIV measurements domain for the wake measurements under different gust inflow.

2.3.6 Uncertainty analysis

To accurately comment on the flow field variables, it is necessary to evaluate the uncertainty of errors in particle image velocimetry (PIV) observations. These mistakes are classified into two types: systematic and random. Systematic errors are produced by factors such as calibration, temporal particle response, optical aberrations, and synchronization, and they may frequently be fixed or ignored. Random errors, on the other hand, can fluctuate over time and are generally produced by out-of-plane motion, low seeding densities, displacement gradients, and recording noise [46]. While some random mistakes may be negligible, the major source of these errors is the calculation of particle displacement and related gradients. As a result, convergence error, which is dictated by the limited number of samples utilized in the calculations, influences the statistical features of the flow field calculated from PIV measurements.

2.3.6.1 Effect of turbulence intensity

In this investigation, 1000 vector fields were employed for each case under various inflow conditions, with the assumption that these vector fields are independent and have a normal distribution. The following equations were utilized to estimate the uncertainty in the measurements, where $k=1.95$, to achieve 95% confidence in the measurements. Table 2.7 presents the normalized uncertainty approximates of flow quantities for the effect of the turbulence intensity measurement campaign.

$$(\varepsilon_U)_{mean} = \frac{k \sigma}{N^{1/2}} \quad (2.5)$$

$$(\varepsilon_U/U_{hub})_{mean} [\%] = \frac{(\varepsilon_U)_{mean}}{U_{hub}} \quad (2.6)$$

Table 2.7 The normalized uncertainty estimates for inflow turbulence cases

| Test Cases | WT-L- TI | WT- M-TI | PD-L- TI | PD-M- TI |
|---------------------------------------|-------------|-------------|-------------|-------------|
| $(\varepsilon_U/U_{hub})_{mean} [\%]$ | 0.426 | 0.565 | 0.349 | 0.501 |
| $(\varepsilon_W/U_{hub})_{mean} [\%]$ | 0.427 | 0.500 | 0.325 | 0.395 |

2.3.6.2 Gust inflow

- Hotwire inflow measurement

In this investigation, 60 gust events were employed for the top hat gust case and 120 gust events in the case of triangular gust. Equation 2.5 and Equation 2.6 were used to estimate the uncertainty.

Table 2.8 The normalized uncertainty estimates for the hotwire measurements of the streamwise gust inflow.

| Test Cases | TR | TH |
|---------------------------------------|-------|-------|
| $(\varepsilon_U/U_\infty)_{mean}$ [%] | 0.470 | 0.664 |

- Inflow PIV measurements

In this investigation, 75 vector fields were employed for each case under various inflow variables, with the assumption that these vector fields are independent and have a normal distribution. Equation 2.5 and Equation 2.6 were used to estimate the uncertainty under gust inflow at the instance where the gust peak occurs but normalized using U_∞ , which is the inflow velocity before the gust event.

Table 2.9 The normalized uncertainty estimates for the PIV measurements of the streamwise gust inflow.

| Test Cases | TR | TH |
|---------------------------------------|-------|-------|
| $(\varepsilon_U/U_\infty)_{mean}$ [%] | 0.623 | 0.727 |
| $(\varepsilon_W/U_\infty)_{mean}$ [%] | 0.867 | 1.108 |

- Wake PIV measurements

In this investigation, 75 vector fields were employed for each case under various inflow variables, with the assumption that these vector fields are independent and have a normal distribution. Equation 2.5 and Equation 2.6 were used to estimate the uncertainty under gust inflow at the instance where the gust peak occurs but normalized using U_∞ which is the inflow velocity before the gust event.

Table 2.10 The normalized uncertainty estimates for the PIV wake measurements under streamwise gust cases.

| Test Cases | TR _{TSR=1} | TR _{TSR=2} | TR _{TSR=3} | TH _{TSR=2} |
|---------------------------------------|---------------------|---------------------|---------------------|---------------------|
| $(\varepsilon_U/U_\infty)_{mean}$ [%] | 3.14 | 3.04 | 3.13 | 3.26 |
| $(\varepsilon_W/U_\infty)_{mean}$ [%] | 3.30 | 3.21 | 3.29 | 3.45 |

- Time-resolved thrust coefficient measurements

In this investigation, 20 gust events were employed for both gust cases. The mean of the thrust coefficient at the gust peak was used to normalize the error.

Table 2.11 The normalized uncertainty estimates for the dynamic thrust coefficient.

| Test Cases | TR _{TSR=1} | TR _{TSR=2} | TR _{TSR=3} | TH _{TSR=2} |
|------------------------------------|---------------------|---------------------|---------------------|---------------------|
| $(\varepsilon_{Ct}/Ct)_{mean}$ [%] | 7.84 | 7.23 | 5.67 | 8.34 |

CHAPTER 3

Results

This chapter entails the results of the two experimental campaigns. The first subsection discusses the effects of ambient turbulence intensity on the decay characteristics of wind turbine models and porous discs. The second subsection discusses the effects of streamwise gust on the near wake of the wind turbine model for three different tip speed ratios. Furthermore, the chapter discusses the effects of the temporal gust profile on the wake of wind turbines for the same tip speed ratio.

3.1 Effects of freestream turbulence intensity

3.1.1 Mean Wake Flow Field

Figure 3.1 presents the normalized velocity deficit contours in the streamwise direction up to 7 times the diameter downstream for the wind turbine model and the porous disc. The velocity deficit is symmetrical around the centerline, indicated by a dashed black line in Figure 3.1, and decreases downstream from the rotor. One should note that there is a small difference in the thrust coefficient of both models based on the control volume approach, as discussed in section 2.3.3. Thus, the comparison of the decay rate of both models will be discussed with caution. However, one should also note that the wake decay rate is not a strong function of the thrust coefficient based on the wake growth rate's exponent in the new Ishihara model [48]. In the low turbulence intensity case, the near wake of the porous disc diffuses faster than the wind turbine model, specifically between 0.5 and 1.5 times the diameter downstream. This is likely due to the porous disc acting like a passive grid, which allows for better mixing. However, the far wake of the porous disc diffuses slower than that of the wind turbine model. The reason behind that is the

turbulence generated by the breakage of tip vortices in the case of a wind turbine occurs later downstream. This enhances the wake recovery for the wind turbine in the far wake. Moreover, in the case of higher inflow turbulence, both the wind turbine model and the porous disc have faster wake diffusion than in the case with low inflow turbulence due to the turbulence mixing characteristics. In the wake region close rotor, the porous disc has a higher velocity decay rate than the wind turbine model, similar to the case with the lower freestream turbulence. However, the wind turbine model still has faster wake diffusion overall, even though the contour levels of both cases are similar in the far wake region.

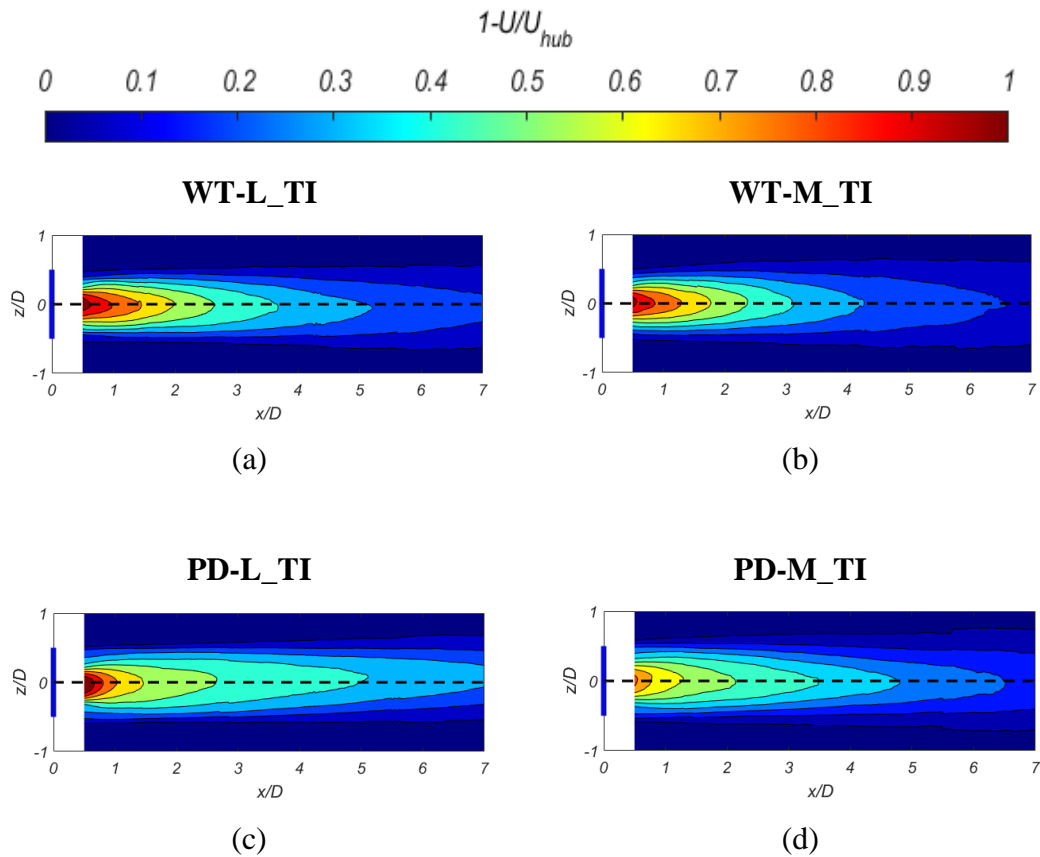


Figure 3.1 Velocity deficit contours in streamwise direction: (a) Wind turbine-low turbulence intensity, (b) Wind turbine-medium turbulence intensity, (c) Porous disc-low turbulence intensity, and (d) Porous disc-medium turbulence intensity. Dashed black lines mark the centerline of the rotor.

Figure 3.2 shows contours of normalized vorticity in the out-of-plane direction in the wake of the wind turbine model as well as the porous disc for various freestream turbulence intensity levels. When the freestream turbulence intensity is low, the two models exhibit a slightly uneven distribution in vorticity. The vorticity in the wind turbine case extends up to 5 diameters downstream in the case of low freestream turbulence intensity. The increase in freestream turbulence enhances the diffusion of the vorticity field so that it diffuses after four diameters downstream in the case of medium turbulence intensity. On the other hand, the vorticity in the porous disc under low freestream turbulence intensity decreases gradually and extends over a larger area. The increases in turbulence intensity diffuse the vorticity after five

diameters downstream. The vorticity in the wake of the wind turbine is higher in the region close to the rotor and lower in the far wake compared to the vorticity in the wake of the porous disc. However, it should be noted that the wind turbine's hub and nacelle contribute to the increased vorticity downstream of the wind turbine model. These factors together lead to higher vorticity in this area.

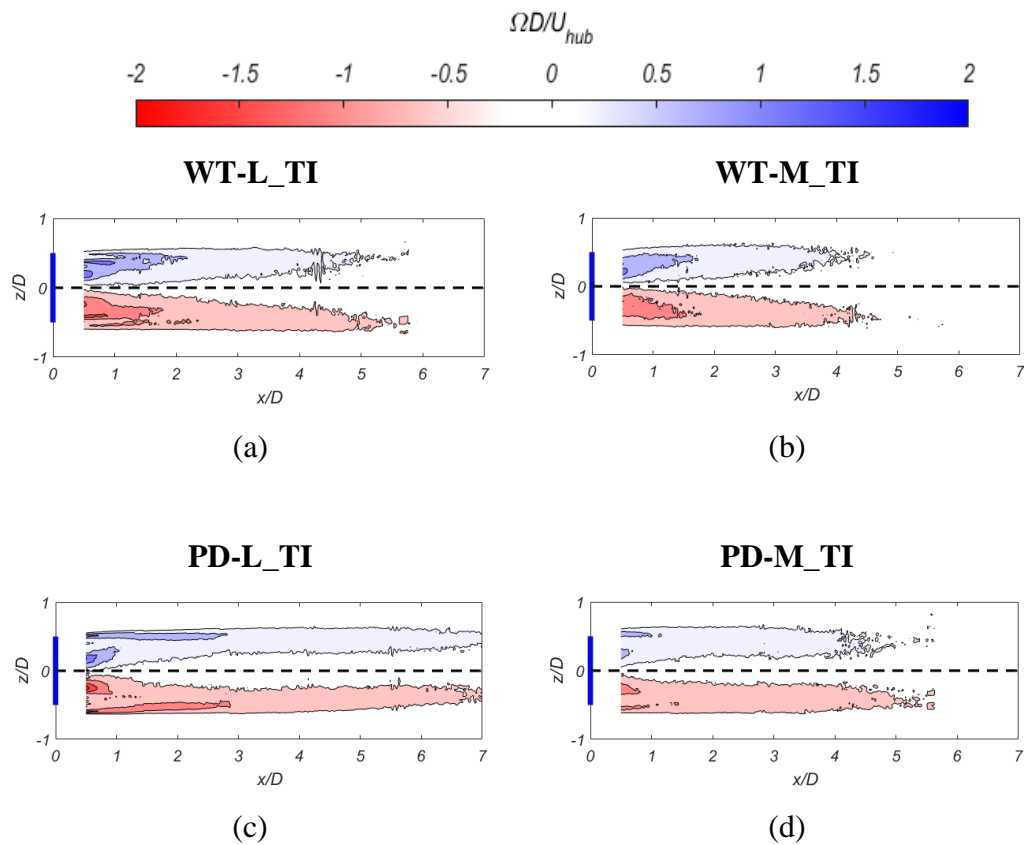


Figure 3.2. Vorticity contour in the out-of-plane direction (a) Wind turbine-low turbulence intensity, (b) Wind turbine-medium turbulence intensity, (c) Porous disc-low turbulence intensity, and (d) Porous disc-medium turbulence intensity. Dashed black lines mark the centerline of the wind rotor.

Figure 3.3 shows the normalized streamwise velocity deficit profiles extracted at different downstream locations ($x=3D$, $5D$, and $7D$) for the porous disc and the wind turbine at two different freestream turbulence intensity conditions. The figures show that when the freestream turbulence intensity level is increased, there is a drop in the

maximum velocity deficit levels for both the turbine and the disc. The figures also show that in the far wake region at $x=5D$ and for the low freestream turbulence intensity condition, the maximum velocity deficit for the wind turbine is reduced to about 33% of its value at $x=3D$, whereas for the disc, it only dropped to about 16% of the value at $x=3D$, indicating that the wind turbine wake decays significantly faster compared to the wake of the porous disc. This result is less pronounced at increased freestream turbulence intensity levels such that the reduction in maximum velocity deficit levels from $x=3D$ to $x=5D$ are 33% and 25% for the wind turbine and the porous disc, respectively, showing again that also under increased freestream turbulence conditions wind turbine wake decays substantially faster. The figures also show that as we go further downstream to $x=7D$, the decay of the disc wake slows down, especially for the low freestream turbulence case. The peak value of the velocity deficit is reduced by only about 37% compared to the value at $x=3D$ for the disc, whereas another 55% reduction is observed for the turbine. These results indicate that even if the disc and the turbine operate at matched Reynolds number and freestream turbulence intensity conditions, their wake development and decay characteristics are significantly different in the near-wake and far-wake regions. This can be further explained by looking at the vorticity profile shown in Figure 3.4. One can see that the decay of vorticity exhibits the same trend. For instance, under low freestream turbulence, at $x=3D$ and $x=5D$, the difference at their respective peaks amounts to 55% and 50% for the wind turbine model and porous disc, respectively. Under higher freestream turbulence intensity at the same location, the difference becomes significantly smaller, amounting to 44% and 43% for the wind turbine and porous disc, respectively.

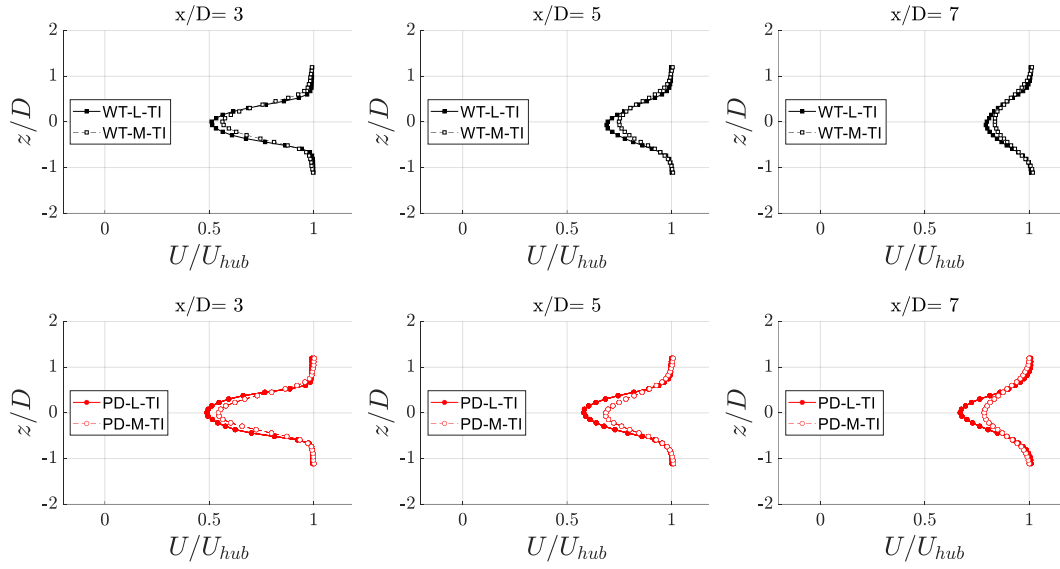


Figure 3.3. Streamwise velocity profile for the two models under different freestream turbulence intensities.

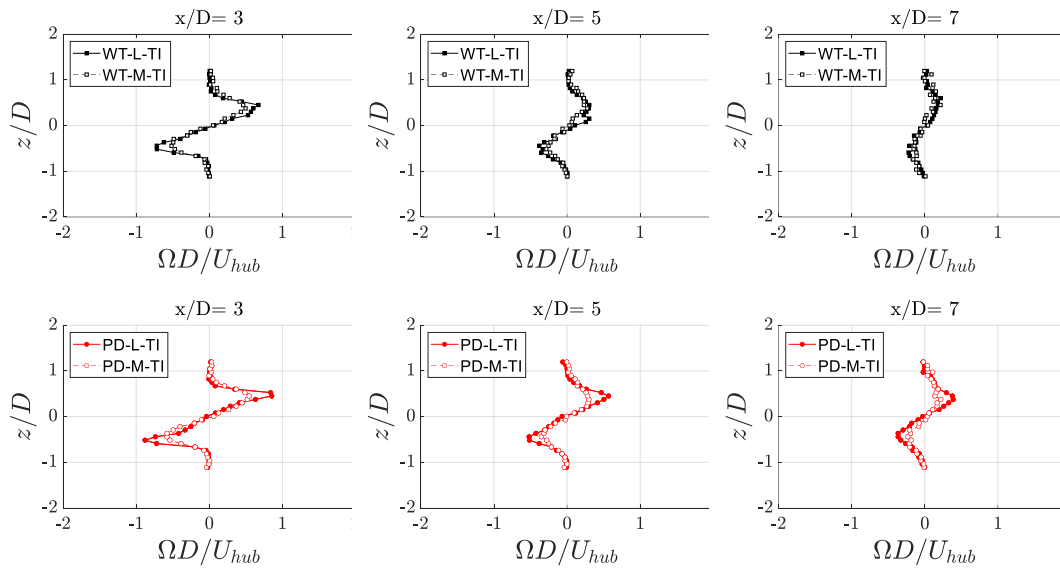


Figure 3.4. Out-of-plane vorticity profile for the two models under different freestream turbulence intensities.

3.1.2 Wake scaling and decay characteristics

The wake of wind turbine model models and porous discs can be scaled to show a collapsing self-similar profile using the wake width and the maximum wake deficit. Furthermore, the wake-spreading characteristics can be quantified using the scaling parameters. In addition, the wake-spreading characteristics will be further quantified using parameters from the Bastankhah wake model [49].

3.1.2.1 Wake scaling

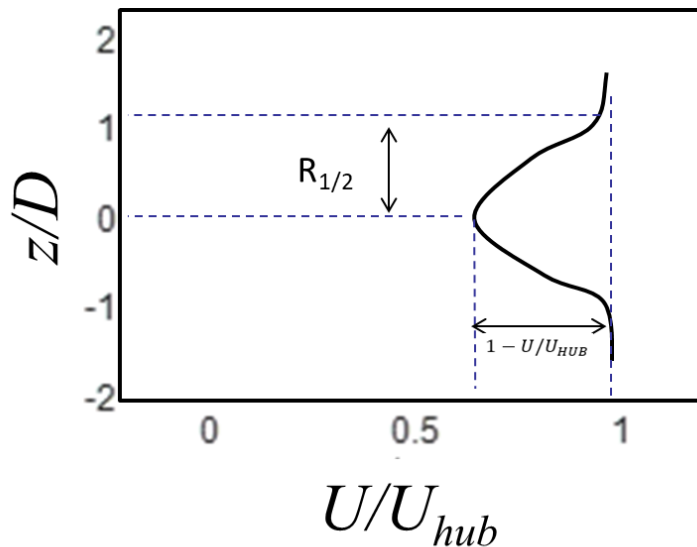


Figure 3.5. A sketch that shows the scaling parameters on the wake profile.

In order to scale the wake profile, the wake half width and the maximum wake deficit have been used as length and velocity scales, respectively. Those parameters are shown in Figure 3.5. Figure 3.6 shows the scaled collapsing wake profiles for the wind turbine model as well as the porous disc for the two freestream turbulence conditions. The wake scaling parameter $1 - U/U_{HUB}$, which is the wake deficit, is shown in Figure 3.7. In this context, U_{HUB} is the inflow velocity at the hub location of the rotor. This scaling parameter seems to behave linearly with a logarithmic x-

axis. This can be used to quantify the wake decay rate by curve fitting the following equation.

$$1 - U/U_{HUB} = A \log\left(\frac{x}{D}\right) + b \quad (2.1)$$

In Equation 2.1, A can be used to quantify the wake decay rate. The curve fitting was done for values greater than $x=3.5D$ to avoid including near-wake effects and to allow for a fair comparison with the porous disc. The wind turbine under medium turbulence intensity has the fastest wake decay, and the porous disc seems to match the wake deficit rate after $x=3.5D$. The wake of the porous disc under low freestream turbulence intensity has the lower decay rate among all. This is all consistent with the findings mentioned in the previous sections. Table 3.1 summarizes the decay rate parameter A for each case. On the other hand, the wake scaling parameter $R_{1/2}$ is the half wake width. The wake width increases as one goes downstream of the rotor, as shown in Figure 3.7. It doesn't seem to get affected by freestream turbulence intensity in the case of porous discs. However, the wind turbine model under low turbulence intensity is only slightly lower than the rest of the cases. The collapsed wake profile can be curve fitted with a gaussian fit, and the scaling parameters can be used to obtain the wake profiles in the far wake. This could be the base for a new analytical model. Nevertheless, a large database of wind turbine's effects of thrust coefficient as well as tip speed ratio effects needs to be established.

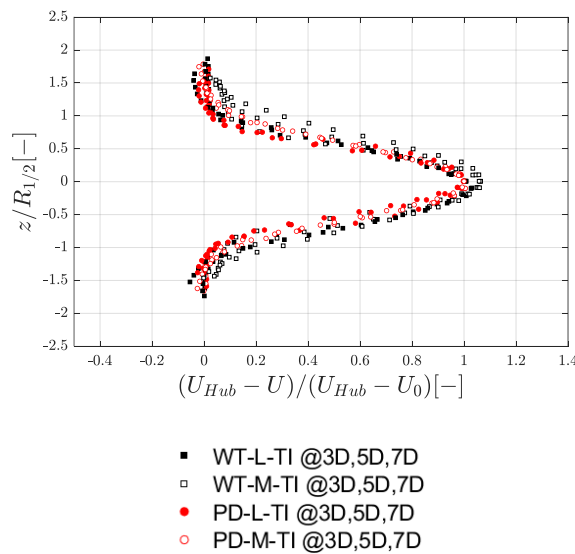


Figure 3.6. (a) Wind Scaled wake velocity profiles using wake half width and the maximum velocity deficit.

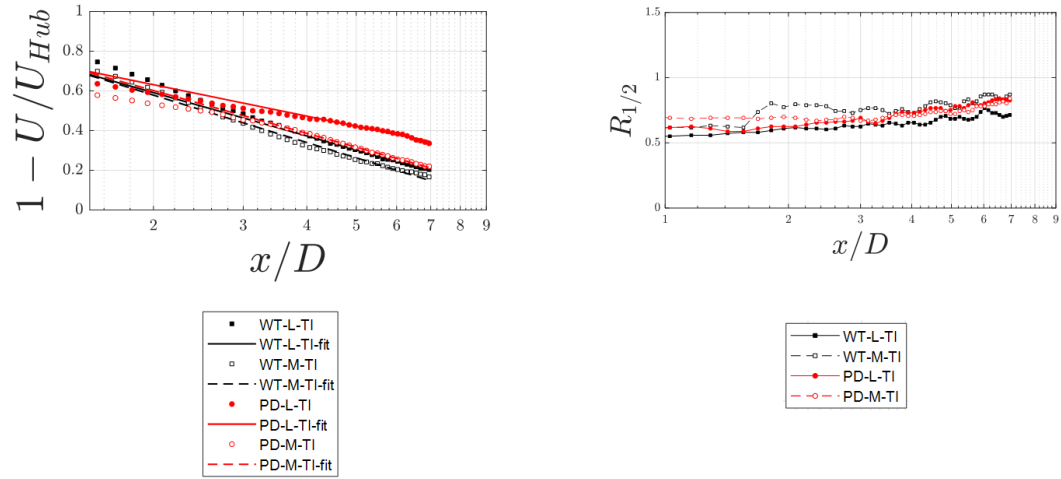


Figure 3.7. The wake decay and wake deficit parameters for the two models at different downstream locations.

Table 3.1 Summary of the wake growth rate parameter A for porous disc and wind turbine model under different freestream turbulence intensities.

| Test Cases | Wake decay rate, A | Initial wake deficit, b |
|--|--------------------|-------------------------|
| Wind turbine-low turbulence intensity (WT-L_TI) | -0.330 | 0.802 |
| Wind turbine-medium turbulence intensity (WT-M_TI) | -0.355 | 0.812 |
| Porous disc-low turbulence intensity (PD-L_TI) | -0.230 | 0.788 |
| Porous disc-medium turbulence intensity (PD-L_TI) | -0.319 | 0.814 |

3.1.2.2 Bastankhah and Porté-Agel Wake Model

The Bastankhah and Porté-Agel wake model [49] is a mathematical model that describes the behavior of wind turbine wakes based on the principles of mass and momentum conservation. In this model, the wake is assumed to be self-similar and have a Gaussian shape, and the rate of wake growth is assumed to be linear. The maximum value of normalized velocity deficit at a particular downstream position (denoted as $C(x)$) can be calculated using the following equation.

$$C(x) = 1 - \sqrt{1 - \frac{C_T}{8\left(\epsilon + \frac{k^*x}{D}\right)^2}} \quad (2.2)$$

$$\frac{\sigma}{D} = k^* \frac{x}{D} + \epsilon \quad (3.2)$$

In this equation, σ represents the standard deviation of the Gaussian-like velocity deficit profiles, k^* is the wake spread rate, D is the diameter of the rotor, and ϵ is the wake width intercept. The velocity profiles are described through the following equation.

$$\frac{\Delta U}{U_\infty} = \left(1 - \sqrt{1 - \frac{C_T}{8\left(\frac{k^*x}{d_0} + \epsilon\right)^2}}\right) \times \exp\left(-\frac{1}{2\left(\frac{k^*x}{d_0} + \epsilon\right)^2} \left\{ \left(\frac{z-z_h}{d_0}\right)^2 + \left(\frac{y}{d_0}\right)^2 \right\}\right) \quad (2.3)$$

Niayifar and Porté-Agel used Large Eddy Simulation (LES) [50] and proposed the following formulation for the wake spread rate and the wake width intercept for the range of 6.5% to 15%.

$$k^* = 0.383I_a + 0.0037 \quad (3.5)$$

$$\epsilon = 0.25\sqrt{\beta}, \quad (3.6)$$

In this equation, I_a is the freestream turbulence intensity and $\beta = \frac{1}{2} \frac{1 + \sqrt{1 - C_T}}{\sqrt{1 - C_T}}$.

Furthermore, Fuertes et al.[30] utilized field measurements and proposed the following formula for the wake width intercept as well as the wake spread rate.

$$k^* = 0.35I_{ambient} \quad (2.4)$$

$$\epsilon = -1.91k^* + 0.34 \quad (2.5)$$

The results variable (σD) was calculated for each case and curve fitted. The variation (σD) with downstream distance for the wind turbine model and the porous disc at different freestream turbulence intensity levels is shown in Figure 3.8

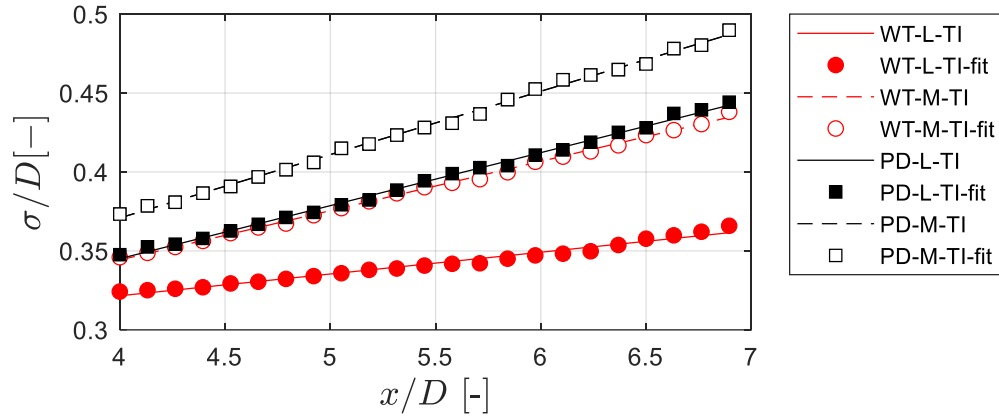


Figure 3.8. The variation of the standard deviation of the Gaussian velocity deficit profiles downstream of porous disc and wind turbine model and different freestream turbulence intensity.

The data in Table 3.1 illustrates how the wake spread rate for the wind turbine model is generally greater than that for the porous disc under the two levels of freestream

turbulence intensity. At a low freestream turbulence intensity, the wake spread rate for the wind turbine model is approximately two times higher than that for the porous disc. However, as the freestream turbulence intensity increases, the variance in the wake spread rate values for the two models becomes smaller. At a high freestream turbulence intensity, the wake spread rate for the wind turbine model is around twice that for the porous disc. Additionally, the wake width intercept for the porous disc is larger than that for the wind turbine model under both freestream turbulence intensity conditions. While the freestream turbulence intensity has little effect on the wake width intercept for the wind turbine model, for the porous disc, it decreases by 18% as the freestream turbulence intensity rises from 0.5% to 4.5%.

Table 3.2 Summary of the wake spread rate parameter k^* and the wake width intercept ϵ for porous disc and wind turbine model under different freestream turbulence intensities.

| Test Cases | Wake spread rate, k^* | Wake width intercept, ϵ |
|--|-------------------------|----------------------------------|
| Wind turbine-low turbulence intensity | 0.033 | 0.287 |
| Wind turbine-medium turbulence intensity | 0.039 | 0.275 |
| Porous disc-low turbulence intensity | 0.014 | 0.302 |
| Porous disc-medium turbulence intensity | 0.031 | 0.223 |

3.2 Effects of a streamwise gust on the wake of a wind turbine

This subsection discusses the effects of a streamwise gust on the dynamic coefficient of thrust. Furthermore, the effects of a streamwise gust on the wind turbine model with different tip speed ratios are discussed qualitatively and quantitatively. The subsection further entails a way to scale a wind turbine wake under streamwise gust. Moreover, the subsection discusses the effects of temporal gust profile on the wake of a wind turbine model. The normalized temporal profiles of the generated gusts are shown in Figure 3.9. The profiles were normalized with a gust width, namely, 2s and

6s for the triangular gust and the top hat gust, respectively. In addition, the profiles were shifted in such a way that $t/T=0$ corresponds to the start of the gust event.

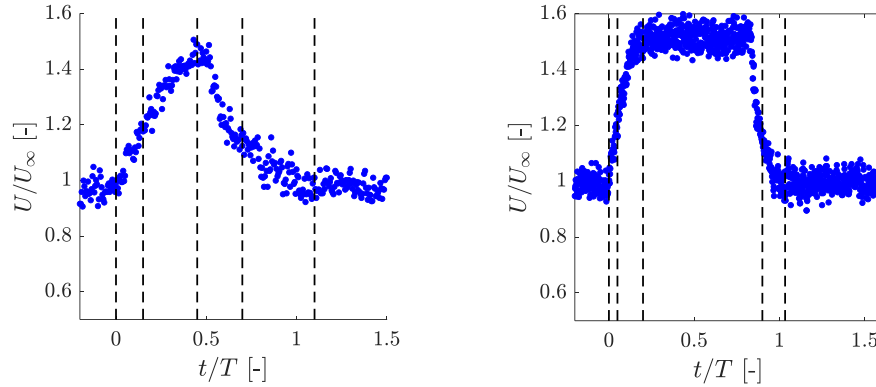


Figure 3.9. The normalized temporal gust profile of the triangular gust and top hat gust. The dashed black line indicates the instances selected to phase lock the PIV measurements.

3.2.1.1 Load measurements

Figure 3.10 shows the dynamic effects of the triangular gust on the thrust coefficient for different tip speed ratios. The thrust coefficient between the gust events matches with the thrust coefficient under uniform inflow, which indicates that the flow settles to a steady state between gust events. The tip speed ratio seems to have little to no effect during the rising edge of the gust. However, during the dip time, the tip speed ratio seems to have an impact on the phase lag of the dynamic response of the thrust coefficient, where the lowest tip speed ratio case seems to have the highest phase lag compared to the other two cases. However, this effect diminishes between the $TR_{TSR=2}$ and $TR_{TSR=3.1}$. Furthermore, the amplitude differences between the cases get more pronounced at the gust peak. For instance, the gust increased the thrust coefficient at the peak by $\sim 135\%$ for the case of $TR_{TSR=1}$, while the increase in thrust coefficient is $\sim 118\%$ for the case of $TR_{TSR=2}$ and $TR_{TSR=3.1}$. Furthermore, one can observe that although the dynamic response of the thrust coefficient reaches the peak

at the same time the gust reaches its peak, the dip time is different. The asymmetry in the rise and dip time is observed in the inflow. However, it is exacerbated by the dynamic response of the thrust coefficient. This can be linked to several factors, one of which is the PID controller, where breaking the turbine during the rise time is easier than controlling the angular velocity during the dip time. In addition, the top hat gust profile seems to reach a slightly higher thrust coefficient at the peak despite having the same gust ratio. This difference in amplitudes is likely due to the wake rotational inertia such that the top hat gust has a higher time scale to overcome this.

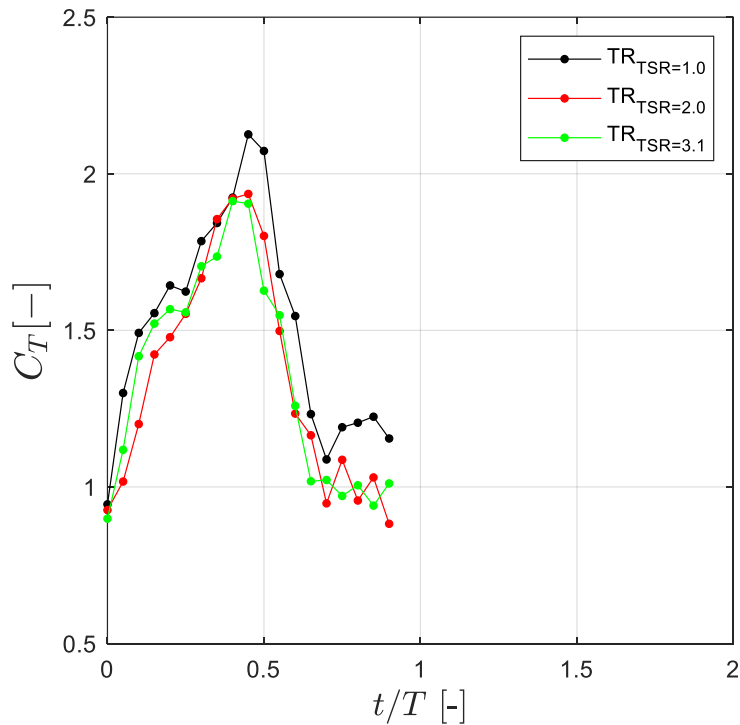


Figure 3.10. The dynamic response of the thrust coefficient of the wind turbine model under triangular gust distribution for different tip speed ratios.

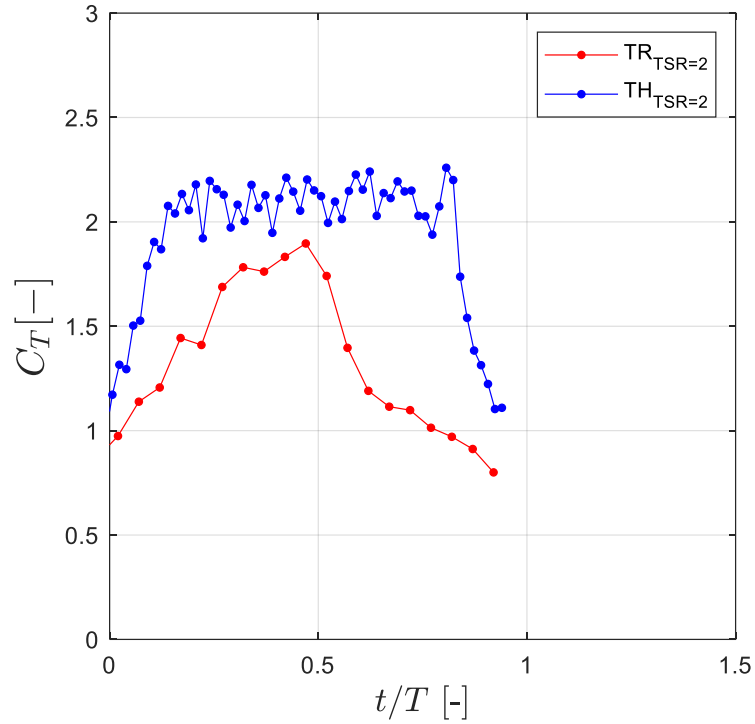


Figure 3.11. The dynamic response of the thrust coefficient of the wind turbine model under triangular gust distribution and top hat gust distribution for the same tip speed ratio.

3.2.1.2 Wake flow field

Figure 3.12 shows the streamwise velocity contours for three different tip speed ratio cases under triangular gust at different instances relative to the gust event. One can observe three different wake evolution mechanisms for the three different tip speed ratios. For example, at 4 s, which is before the gust, although the initial wake deficit for all the cases is almost the same until $x=2D$ after that, case $TR_{TSR=2}$ seems to have the slowest wake decay among the three cases. In contrast, $TR_{TSR=1}$ and $TR_{TSR=3}$ have very comparable wake decay. This pattern stays the same throughout the rising edge of the gust, i.e., until $t/T=0.45$. However, during the dip, there is a noticeable deficit increase in the $TR_{TSR=1}$ case compared with the other two cases, which are consistent

with the behavior of the thrust Figure 3.10. Moreover, the wake deficit gets significantly deeper during the gust event. The reason behind this is the observed increase in the dynamic thrust coefficient due to gust.

The out-of-plane vorticity contours are shown in Figure 3.13, which elucidates the general pattern where increasing the wind turbine tip speed ratio slightly increases the vorticity in the wake of a wind turbine. The difference in the vorticity field decreases as one goes further downstream as tip vortices break down. Furthermore, the gust increases the levels of vorticity in the wake of the wind turbine for all the cases to reach the maximum level at the gust peak, enhancing the differences between the cases in the region below $x=2D$. However, after that, the distinctions in vorticity levels between the cases diminish despite the initial differences.

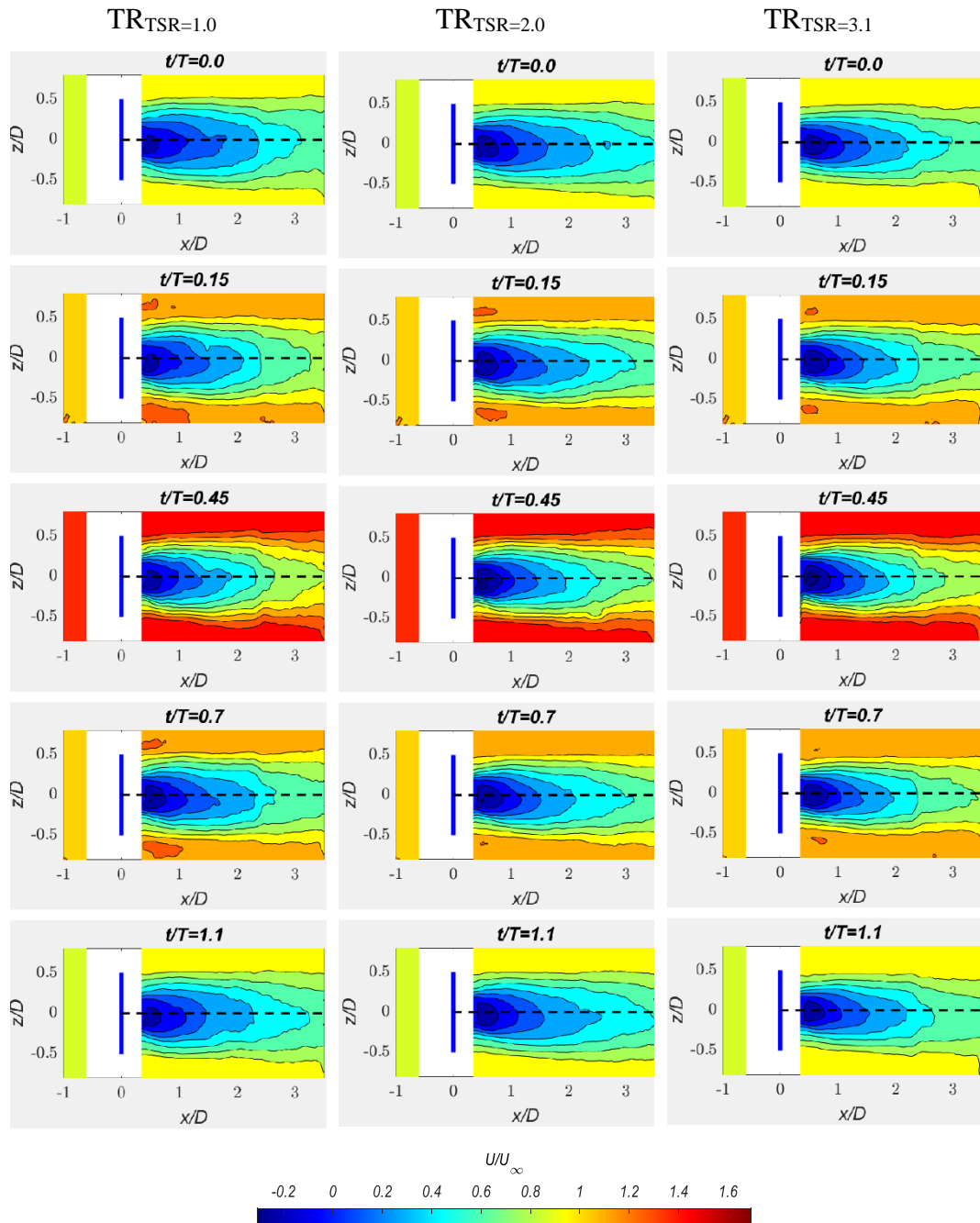


Figure 3.12. velocity contour in the streamwise direction for different tip speed ratios under triangular gust at different instances.

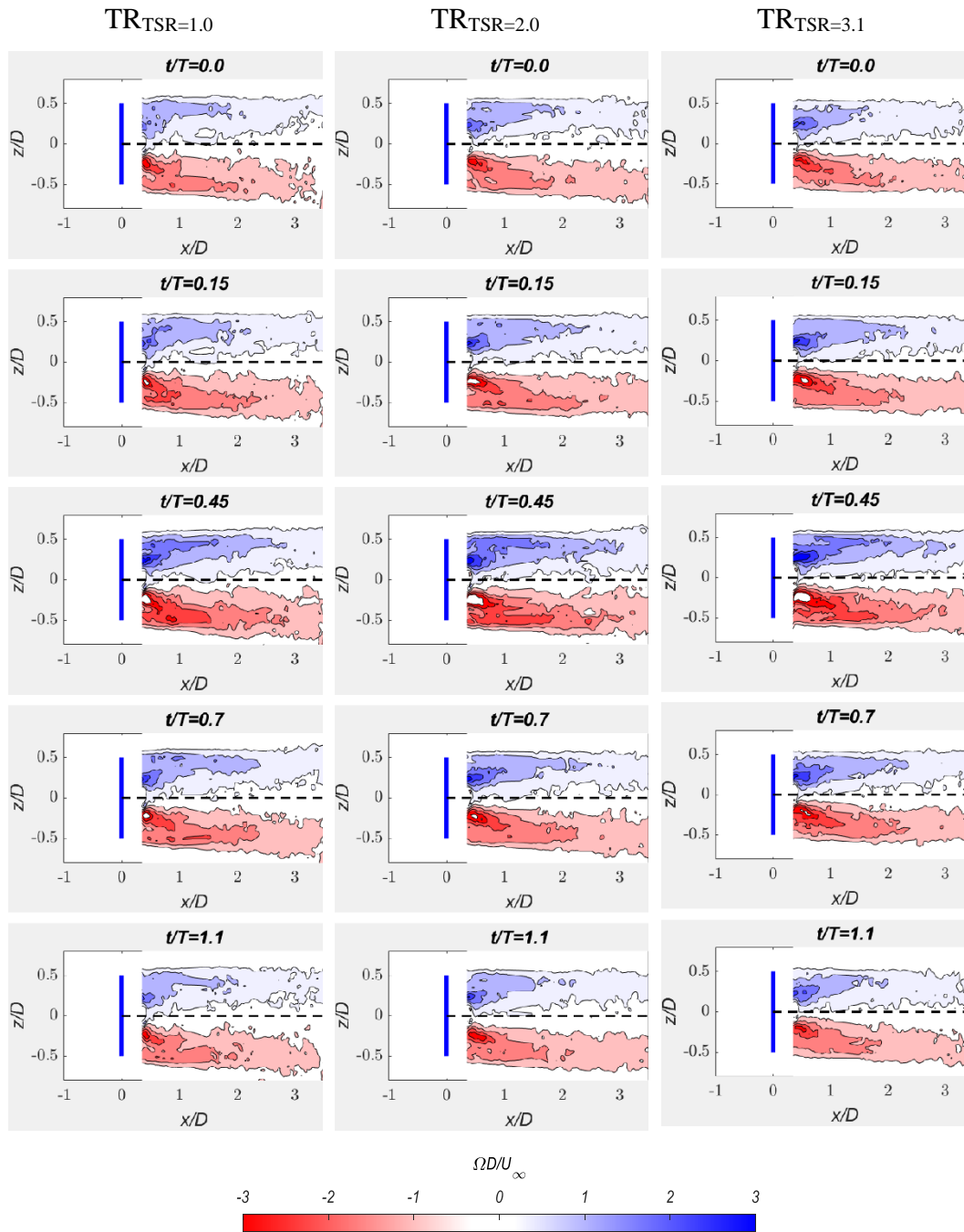


Figure 3.13. Normalized out-of-plane vorticity contour for different tip speed ratios under triangular gust at different instances.

Figure 3.14 shows the velocity profile for different tip speed ratios at different streamwise locations from 0.5 diameters to 3 diameters downstream of the wind turbine model at different instances relative to the gust. One can see that there is little to no difference in the velocity deficit in the very near wake region, i.e., below $x=2D$ during the gust. However, the differences start to appear after $x=2D$. For instance, the case $TR_{TSR=2}$ has the lowest deficit prior to the gust rise by $\sim 52\%$ at $x=3D$, with the other two cases exhibiting a similar velocity deficit of $\sim 44\%$. The differences increase with the rising edge of the gust to reach the maximum at the gust peak amounting to $\sim 84\%$ for the $TR_{TSR=2}$ case and $\sim 73\%$ for the other cases. However, during the dip time of the gust, the center of the wake behaves differently from the region outside the wake. This pattern is clearly shown in Figure 3.15, which shows the temporal change in the velocity at the wake center at $x=3D$ compared to the temporal change in the inflow. One can see that the response of the wake to the inflow perturbation is faster at lower tip speed ratios and flattens as the tip speed ratio increases. For instance, during the dip time, the velocity at the wake center drops faster for the $TR_{TSR=1}$ case. This is likely due to the low rotational inertia of the wake at a low tip speed ratio. In turn, this is translated into the thrust coefficient as the observed phase lag. Furthermore, the reason for the higher wake deficit in $TR_{TSR=2}$ compared to $TR_{TSR=1}$ is likely to be the tip speed ratio effects since their thrust coefficients are very close. This is consistent with the literature where lower tip speed ratios have been shown to enhance the wake recovery in the near wake [38] [52]. On the other hand, $TR_{TSR=3}$ case has a non-negligible lower thrust coefficient which explains the lower velocity deficit at $x=2D$ onwards compared to the $TR_{TSR=2}$ case.

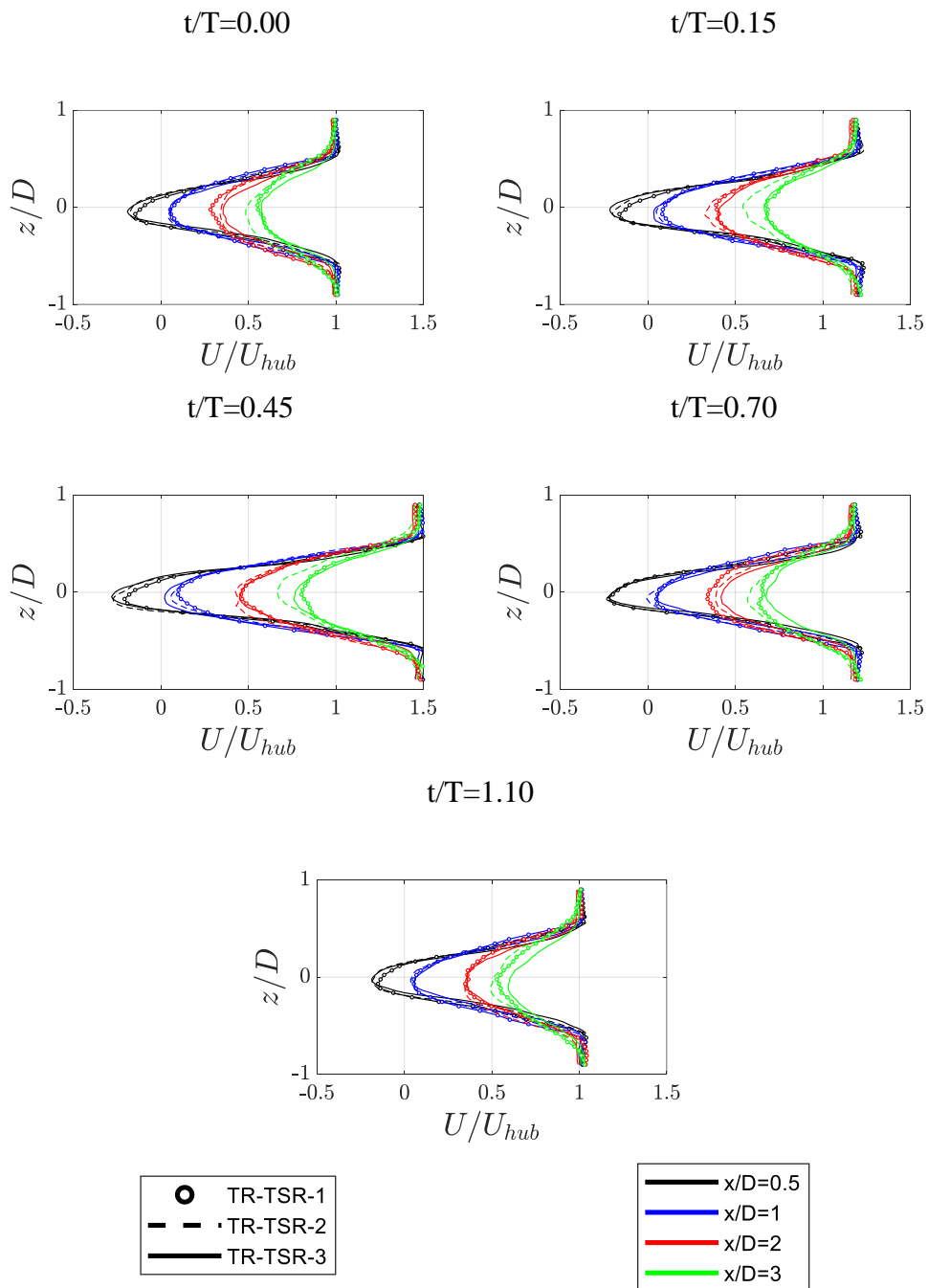


Figure 3.14 Streamwise velocity profile for different tip speed ratios under triangular gust at different instances.

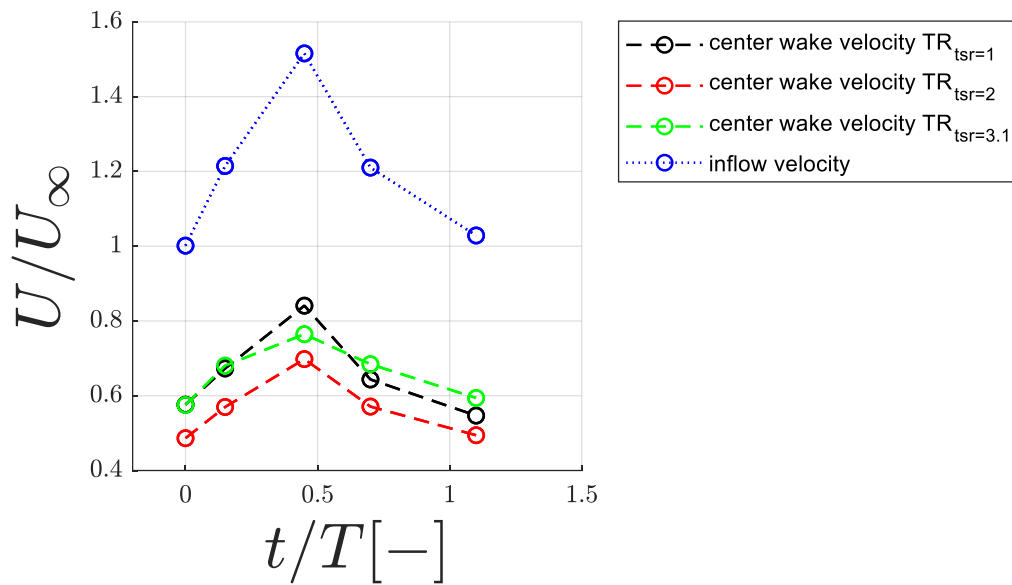


Figure 3.15 The center wake velocity at $x/D=3$ for different tip speed ratios compared with the inflow velocity.

3.2.1.3 Wake scaling under streamwise gust

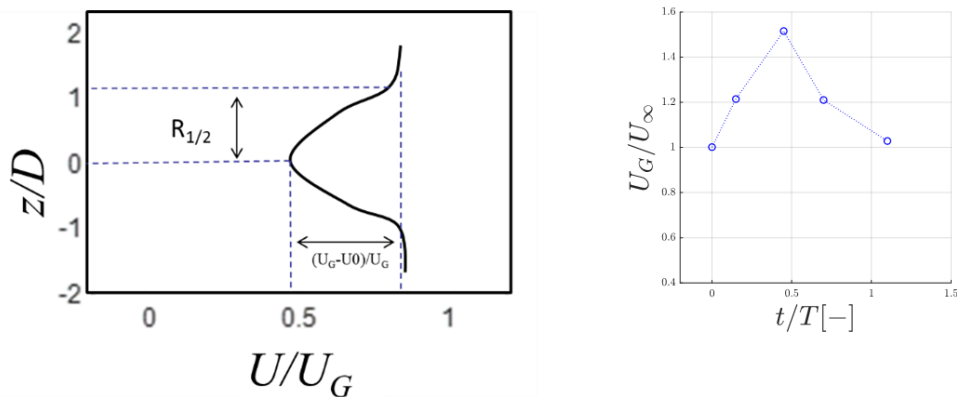


Figure 3.16 A sketch showing the parameters used to scale the wake of a wind turbine under streamwise gust. on the right the wind turbine's inflow velocity during the gust.

In order to scale the wake profile, the wake half width and the maximum gust wake deficit have been used as length and velocity scales, respectively. Those parameters

are shown in Figure 3.16. Figure 3.17 shows the scaled wake profile for the wind turbine with different tip speed ratios at different gust instances. Where U_G is the velocity of the gust at the selected instance, as shown on the right in Figure 3.16, U_o is the minimum velocity in the wake, and $R_{1/2}$ is the wake half-width. Figure 3.18 shows the decay of the normalized velocity scaling parameter $(U_G - U_o)$. One can observe that the parameter behaves linearly in the log-scaled graph after $x=2.4D$ for all tip speed ratio cases. Moreover, the $(U_G - U_o)$ parameter, which represents the wake deficit at the selected instance relative to the gust, behaves differently for different tip speed ratios. This is better demonstrated in Table 3.3, which shows the coefficients for the velocity scaling's parameter log fit. The fit is for values greater than $x/D=2.4$ to ensure that fits are in the linear region. For instance, for the cases $TR_{TSR=1}$ and $TR_{TSR=2}$, the wake decay rate increases initially as the wind turbine progresses through the gust and then slows down to reach the minimum at the gust peak. After that, the wake decay rate increases again. However, the wake decay rate increases as the wind turbine go through the gust and keep increasing after the gust peak for the $TR_{TSR=3.1}$ case. This shows the effects of the tip speed ratio on the wake rotational inertia. Furthermore, the wake width behavior as one moves downstream is shown in Figure 3.19. The gust does not seem to affect the wake width of the wind turbine in the near wake. However, the three cases have a slightly different overall wake width. For instance, $TR_{TSR=1}$ has the highest overall wake width with a wake width $R_{1/2}=0.55$ at $x=2D$. The case $TR_{TSR=2}$ is slightly lower with a wake width of $R_{1/2}=0.52$ at $x=2D$ and the case, $TR_{TSR=3}$ has the lowest wake width overall with about $R_{1/2}=0.45$ at $x=2D$. These differences can be attributed to the differences in the thrust coefficient, as shown in [48][49], that the thrust coefficient impacts the wake expansion of wind turbines. The collapsed profile can be curve-fitted using a Gaussian fit. Coupling that with scaling parameters can provide a model to predict the effects of the gust on the wake. Nevertheless, more data needs to be gathered in regard to the effect of the thrust coefficient as well as the tip speed ratio.

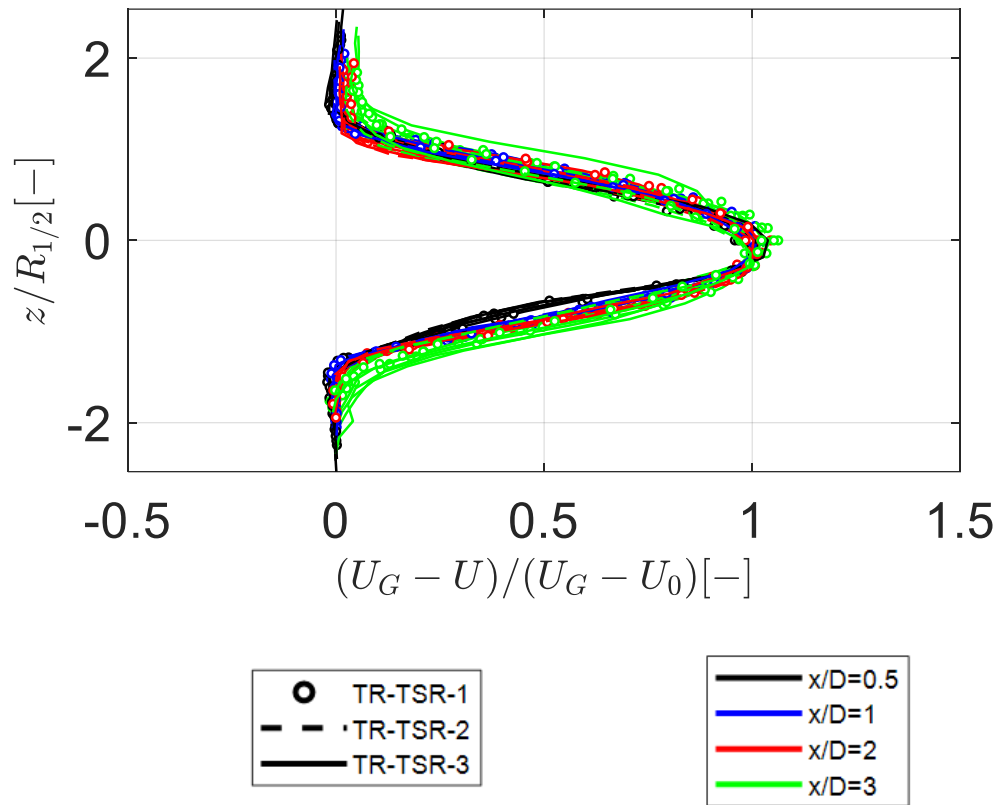


Figure 3.17 Scaled wake profile of a wind turbine with different tip speed ratios at different instances relative to the gust and different downstream locations.

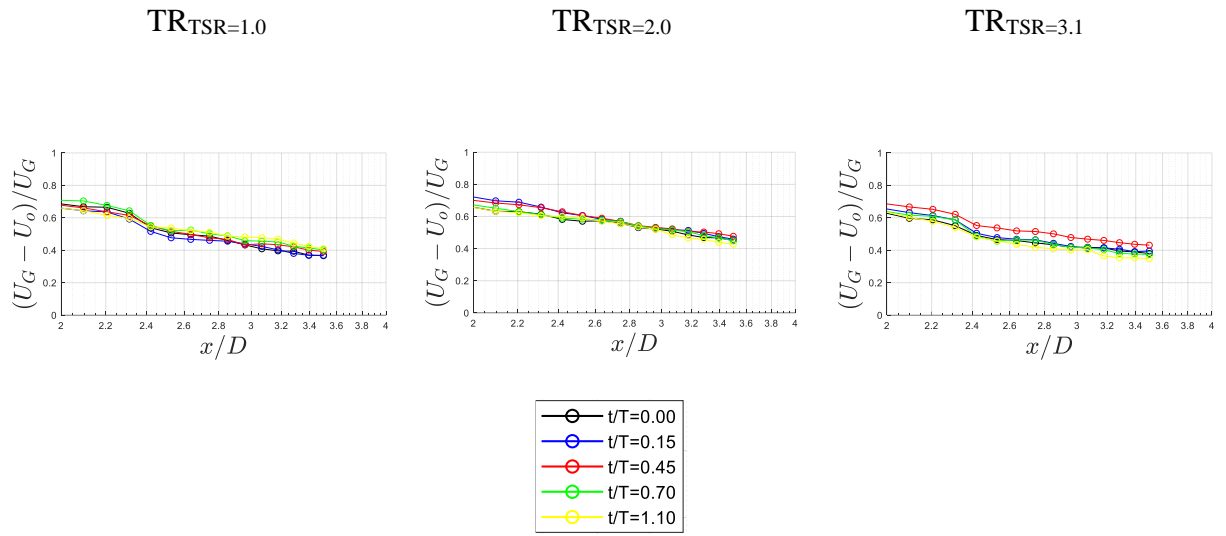


Figure 3.18 Variation of the maximum velocity deficit downstream for different tip speed ratios under triangular gust.

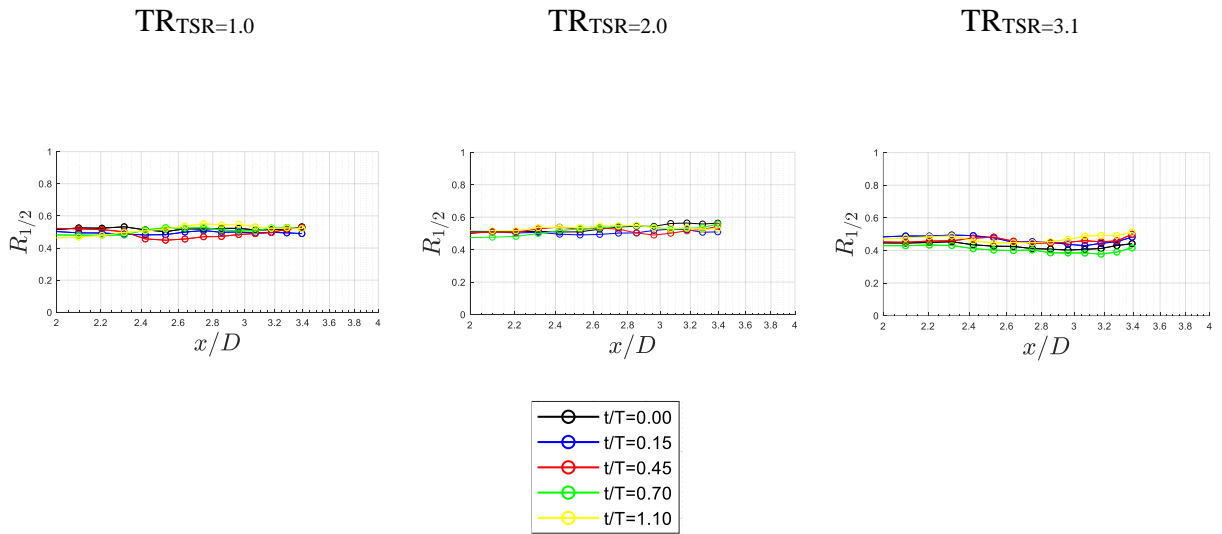


Figure 3.19 Variation of the wake half width downstream of the wind turbine model for different tip speed ratios under triangular gust.

Table 3.3 Summary of the wake spread rate parameter A and the deficit intercept b for different tip speed ratio and different instances with the gust.

| Test cases | [($U_G - U_0$)/ $U_G = A \log(x/D) + b$] | | | | | |
|------------|---|-------|----------------|-------|----------------|-------|
| | $TR_{TSR=1.0}$ | | $TR_{TSR=2.0}$ | | $TR_{TSR=3.1}$ | |
| | A | b | A | b | A | b |
| $t/T=0.00$ | -0.383 | 0.841 | -0.418 | 0.971 | -0.204 | 0.642 |
| $t/T=0.15$ | -0.516 | 1.000 | -0.470 | 1.049 | -0.220 | 0.662 |
| $t/T=0.45$ | -0.291 | 0.760 | -0.321 | 0.882 | -0.344 | 0.856 |
| $t/T=0.70$ | -0.387 | 0.891 | -0.432 | 0.995 | -0.345 | 0.797 |
| $t/T=1.10$ | -0.469 | 1.003 | -0.522 | 1.076 | -0.424 | 0.865 |

3.2.1.4 Gust profile effects

Figure 3.20 shows the streamwise velocity contours in the wake of a wind turbine under two gust profiles with a matching rise and dip time at different instances relative to the gust. By matching the rise and the dip time of the gust one can replicate the effects on the wake as well. This is further elucidated by Figure 3.21, which shows the velocity profiles at different downstream locations. This finding can be useful experimentally by dividing the complex temporal gust profiles into simpler profiles to test them as well as in cases where high cycle loading can be dangerous to the model that will be tested.

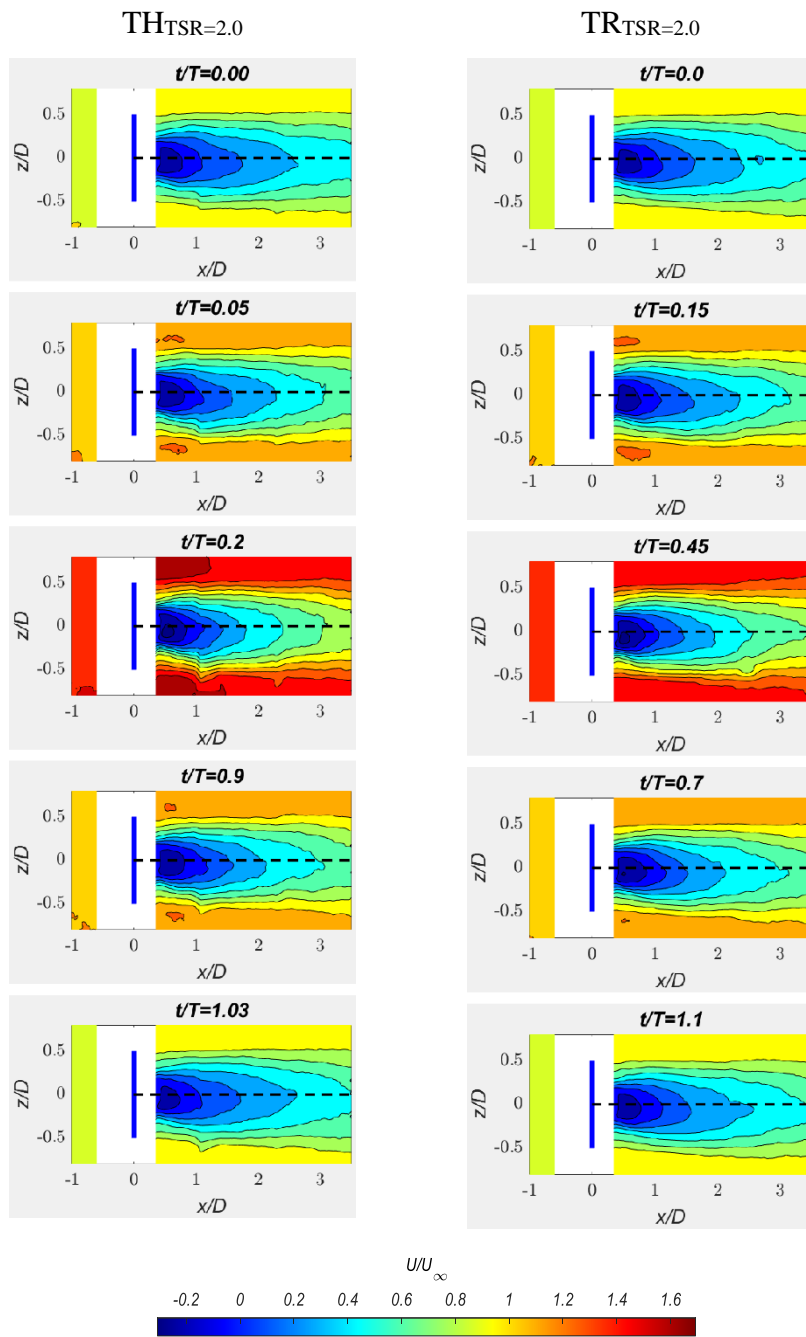


Figure 3.20 Streamwise velocity contour in the wake of a model wind turbine operating with a tip speed ratio of 2 under a top hat and a triangular gust profile.

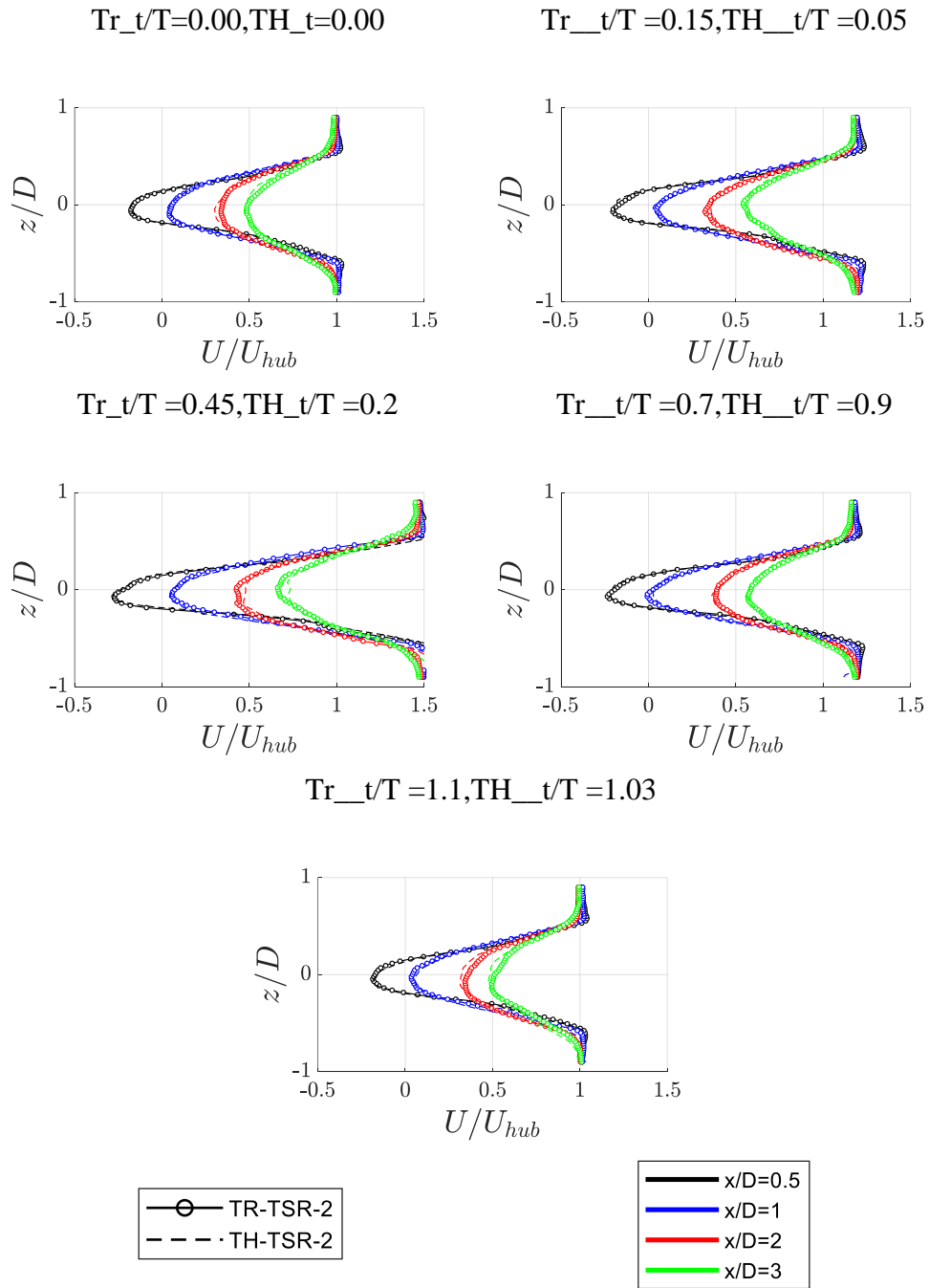


Figure 3.21 Streamwise velocity profile for the same tip speed ratio under a triangular gust and a top hat gust at different instances.

CHAPTER 4

Conclusion

In this study, the wake of a porous disc and a wind turbine model was investigated under two different inflow conditions. The two rotors had a comparable thrust coefficient. For the effect of freestream turbulence intensity, a passive grid was used to generate the turbulence for the medium turbulence intensity, and the low freestream turbulence intensity case was with the tunnel baseline turbulence. Two-dimensional two-component (2D2C) particle image velocimetry (PIV) was used to investigate the impacts of such ambient conditions on the wake of wind turbine models and porous discs. This part of the study will help to understand and highlight the differences between both models. Moreover, the results can help develop a new analytical wake model. For the gust inflow, the active grid was used to generate two different gust profiles with a matching gust ratio of 0.5. Namely, a triangular temporal distribution and a top hat temporal distribution. The study compares the temporal effects of the generated gust profiles on the wake of the wind turbine model operating with different tip speed ratios. Single-wire hotwire as well as phased locked Two-dimensional two-component (2D2C) particle image velocimetry (PIV) to characterize the temporal and spatial gust generated by the active grid. In addition, phased locked Two-dimensional two-component (2D2C) particle image velocimetry (PIV) was used to investigate the wake response of a wind turbine model operating with three different tip speed ratios to streamwise gust. Furthermore, the wake response of the wind turbine model to a gust with a triangular temporal distribution is compared to the response to a top hat gust temporal while operating with the same tip speed ratio. Additionally, the influence of the gust on the dynamic thrust coefficient of the wind turbine model is studied for all the cases. The results will help understand the effects of tip speed ratio on the wake of a model wind turbine. In addition, it will offer insight into the effects of streamwise gusts on wind turbines.

The main conclusions can be listed below:

- The wind turbine model cases exhibit a more significant deficit in wake velocity compared to the porous disc cases at both levels of freestream turbulence. The porous disc cases recover more rapidly downstream of the models up until the tip vortices dissipate; after that, the wind turbine model's wake diffuses more quickly. The results also suggest that the rate of wake diffusion increases as freestream turbulence increases for the two models.
- The vorticity in the wake of the wind turbine model at low freestream turbulence intensity is stronger and covers a wider area close to the model and dissipates as one goes further downstream. In contrast, the vorticity generated by the porous disc is narrower near the tip and travels further in comparison to the wind turbine model. However, when freestream turbulence intensity is stronger, the vorticity in both models becomes more similar in magnitudes as well as spreading behavior.
- The far wake of porous discs and wind turbine models can be scaled to collapse on gaussian shaped profile using the wake half width and the maximum wake deficit as length scale and velocity scale, respectively. Furthermore, the decay of the maximum wake deficit can be curve fitted in a logarithmic curve. The slope of that curve can be used as the parameter to quantify the decay rate. In addition, the wake width of porous discs seems to get less affected by the inflow turbulence. However, the wind turbine wake width of the wind turbine is lower under lower turbulence intensity. This can be used as the basis for a new analytical model for the wake of wind turbines, but it needs more data on the effects of the thrust coefficient.
- The tip speed ratio affects the response of the wake to gust, as varying the tip speed ratio has proved to affect the wake evolution of the wind turbine despite the high inertial changes of the flow due to gust. Those effects could be partially attributed to the wake rotational inertia. Furthermore, the gust has been shown to enlarge the differences between different tip speed ratio cases.

- A new scaling methodology for scaling the wake under gust is developed. The scaled wake profiles show a collapsing wake profile. Furthermore, the scaling parameters were curve fitted to quantify the wake decay rate of the wind turbine at different instances relative to the gust. This can be the basis of an analytical model to determine the wake profile of wind turbines under gust. However, more investigation needs to be done in regard to the effects of thrust coefficient and higher tip speed ratio.
- Two gust profiles with the matching rise and dip times prove to have the same effect on the model wind turbine wake. This could be useful in simplifying complex temporal gust profiles by dividing them into simpler temporal distributions.

As future works:

- The far wake can be investigated under gust;
- Different complex streamwise gust profiles can be investigated;
- The effects of extreme wind shear on the wake of wind turbines can be investigated;
- An analytical model can be developed for the wake of wind turbines under streamwise gust.

REFERENCES

- [1] IEA (2022), Wind Electricity, IEA, Paris <https://www.iea.org/reports/wind-electricity>, License: CC BY 4.0
- [2] IEA (2022), Global Energy and Climate Model, IEA, Paris <https://www.iea.org/reports/global-energy-and-climate-model>, License: CC BY 4.0
- [3] Ueckerdt, F., Hirth, L., Luderer, G., and Edenhofer, O.: System LCOE: What are the costs of variable renewables, *Energy*, 63, 61–75, <https://doi.org/10.1016/j.energy.2013.10.072>, 2013.
- [4] Hu, W., Letson, F., Barthelmie, R. J. and Pryor, S. C.: Wind gust characterization at wind turbine relevant heights in moderately complex terrain, *J. Appl. Meteorol. Climatol.*, 57(7), 1459–1476, doi:10.1175/JAMC-D-18-0040.1, 2018.
- [5] L. J. L. Stival, A. K. Guetter, F. O. Andrade, 2017. “The Impact of Wind Shear and Turbulence Intensity on Wind Turbine Power Performance”. *ESPAÇO ENERGIA*, issue 27
- [6] ISMAIEL, A., YOSHIDA Sh., 2018. Study of turbulence intensity effect on the fatigue lifetime of wind turbines. *Evergreen* ISSN 2189-0420. vol.5, no 1, 25-32.
- [7] Branlard, E. Wind energy: On the statistics of gusts and their propagation through a wind farm. ECNWind-Memo-09-005 Master’s Thesis, Energy research Centre of the Netherlands, Petten, the Netherlands, February 2009.
- [8] Burton, T., N. Jenkins, D. Sharpe, and E. Bossanyi, 2011: *Wind Energy Handbook*. 2nd ed. John Wiley and Sons, 780 pp.
- [9] Germanischer Lloyd, 2010: *Guideline for the certification of wind turbines*. Germanischer Lloyd Industrial Services Tech. Rep., 389 pp.

- [10] Manwell, J. F., J. G. McGowan, and A. L. Rogers, 2010: *Wind Energy Explained: Theory, Design and Application*. 2nd ed. John Wiley and Sons, 704 pp.
- [11] International Electrotechnical Commission, 2005: *Wind turbines— Part I: Design requirements*. IEC Rep. 61400–1, 90 pp
- [12] Phillip Donely. Summary of information relating to gust loads on airplanes. Technical report, NASA, 1950.
- [13] Wilmer H. Reed III. Aeroelasticity matters: Some reflections on two decades of testing in the nasa langley dynamics tunnel. In *Intern. Symp. on Aeroelasticity*; 5-7 Oct. 1980 - 1 Oct. 1981; Nuremberg; Germany, 1981.
- [14] Yigili, I., Andirin, M.A., Kurban E., Baskan, O., Percin, M., 2021 “Design and experimental investigation of a wind tunnel gust generator”. Ankara International Aerospace Conference
- [15] Quinn, D. B., Watts, A., Nagle, T., Lentink, D. 2017. “A new low-turbulence wind tunnel for animal and small vehicle flight experiments”, *Royal Society Open Science*, 4(3), 160960.
- [16] Traphan, D., Wester, T. T. B., Peinke, J. & Gülker, G. 2018 On the aerodynamic behavior of an airfoil under tailored turbulent inflow conditions. In *Proceedings of the 5th International*
- [17] Neuhaus, L., Berger, F., Peinke, J. Hölling, M. 2021. Exploring the capabilities of active grids. *Exp Fluids* 62, 130. <https://doi.org/10.1007/s00348-021-03224-5>
- [18] Conference on Experimental Fluid Mechanics, Munich, Germany. Universität der Bundeswehr München.
- [19] Shirzadeh, K., Hangan, H., Crawford, C., and Hashemi Tari, P.: Investigating the loads and performance of a model horizontal axis wind turbine under reproducible IEC extreme operational conditions, *Wind Energy. Sci.*, 6, 477–489, <https://doi.org/10.5194/wes6-477-2021>, 2021.

- [20] S. M. Mohsen and J. C. Larue, "The decay power law in grid-generated turbulence," *J. Fluid Mech.*, vol. 219, pp. 195–214, 1990, doi: 10.1017/S0022112090002919.
- [21] Mydlarski, L. 2017 A turbulent quarter century of active grids: from Makita (1991) to the present. *Fluid Dyn. Res.* 49 (6), 061401. [CrossRefGoogle Scholar](#)
- [22] Tassa Y and Kamotani Y 1975 Experiments on turbulence behind a grid with jet injection in downstream and upstream direction *Phys. Fluids* 18 411–4
- [23] Gad-el Hak M and Corrsin S 1974 Measurements of the nearly isotropic turbulence behind a uniform jet grid *J. Fluid Mech.* 62 115–43
- [24] Makita H 1991 Realization of a large-scale turbulence field in a small wind tunnel *Fluid Dyn. Res.* 853–64
- [25] Larssen J V and Devenport W J 2011 On the generation of large-scale homogeneous turbulence *Exp. Fluids* 50 1207–23
- [26] Hearst R J and Lavoie P 2015 The effect of active grid initial conditions on high Reynolds number, turbulence *Exp. Fluids* 56 185
- [27] C. S. Shet, M. R. Cholemari, and S. V. Veeravalli, "Optimizing the performance of an active grid to generate high intensity isotropic free stream turbulence", *Physics of Fluids* 32, 095120 (2020) <https://doi.org/10.1063/5.0018932>
- [28] Cekli H E and van de Water W 2010 Tailoring turbulence with an active grid *Exp. Fluids* 49 409–16 Comte-Bellot G and Corrsin S 1966 The use of a contraction to improve the isotropy of grid-generated turbulence *J. Fluid Mech.* 25 657–82
- [29] Hearst, RJ, Ganapathisubramani, B. Tailoring incoming shear and turbulence profiles for lab-scale wind turbines. *Wind Energy*. 2017; 20: 2021– 2035. <https://doi.org/10.1002/we.2138>

- [30] F. C. Fuertes, C. D. Markfort, and F. Porté-Agel, “Wind turbine wake characterization with nacelle-mounted wind lidars for analytical wake model validation,” *Remote Sens.*, vol. 10, no. 5, pp. 1–18, 2018, doi: 10.3390/rs10050668.
- [31] L. M. Bardal, L. R. Sætran, and E. Wangsness, *Performance test of a 3MW wind turbine - Effects of shear and turbulence*, vol. 80. Elsevier B.V., 2015. doi: 10.1016/j.egypro.2015.11.410.
- [32] W. Zhang, C. D. Markfort, and F. Porté-Agel, “Wind-Turbine Wakes in a Convective Boundary Layer: A Wind-Tunnel Study,” *Boundary-Layer Meteorol.*, vol. 146, no. 2, pp. 161–179, 2013, doi: 10.1007/s10546-012-9751-4.
- [33] B. Öztürk, A. Hassanein, M. Tuğrul Akpolat, A. Abdulrahim, M. Perçin, and O. Uzol, “Effects of freestream turbulence on the wake growth rate of a wind turbine model and a porous disc,” *J. Phys. Conf. Ser.*, vol. 2265, no. 2, p. 022042, 2022
- [34] Aubrun S, Loyer S, Hancock P E and Hayden P 2013 Wind turbine wake properties: Comparison between a non-rotating simplified wind turbine model and a rotating model *J. Wind Eng. Ind. Aerodyn.* 120 1–8
- [35] Lignarolo L E M, Ragni D, Ferreira C J and Van Bussel G J W 2016 Experimental comparison of a wind-turbine and of an actuator-disc near wake *J. Renew. Sustain. Energy* 8
- [36] Camp E H and Cal R B 2016 Mean kinetic energy transport and event classification in a model wind turbine array versus an array of porous disks: Energy budget and octant analysis *Phys.Rev. Fluids* 1
- [37] Neunaber I 2019 Stochastic investigation of the evolution of small-scale turbulence in the wake of a wind turbine exposed to different inflow conditions (Oldenburg: Carl von Ossietzky University of Oldenburg)
- [38] Nakashima, S., Fujio, H., Nishio, N., Arakawa, C., & Iida, M. (2016). Influence of tip speed ratio on a real wind turbine wake profile using LiDAR. *intervals*, 3, 75.

- [39] Berger, Frederik, et al. "Experimental analysis of the dynamic inflow effect due to coherent gusts." *Wind Energy Science Discussions* (2022): 1-26.
- [40] I.Yigili, M.A. Andirin, M.T. Akpolat, O. Baskan, M. Percin and O. Uzol. Design of a gust generator and comparison of wind turbine model and porous disc wake flows in a transverse gust. *Journal of Physics: Conference Series*, Vol. 2265, Issue 2, Wind and Wind Farms; Measurement and Testing, 2022.doi:10.1088/1742-6596/2265/2/022108
- [41] El Makdah, A. M., Ruzzante, S., Zhang, K., & Rival, D. E. (2019). The influence of axial gusts on the output of low-inertia rotors. *Journal of Fluids and Structures*, 88, 71-82.
- [42] Andirin, M. A. (2022). GENERATION AND EXPERIMENTAL INVESTIGATIONS OF GUSTY FLOWS IN WIND TUNNELS [M.S. - Master of Science]. Middle East Technical University.
- [43] Knebel, P., Kittel, A., Peinke, J. 2011. "Atmospheric wind field conditions generated by active grids", *Experiments in Fluids*, 51(2), 47
- [44] L. J. Vermeer, J. N. Sørensen, and A. Crespo, "Wind turbine wake aerodynamics," *Prog. Aerosp. Sci.*, vol. 39, no. 6–7, pp. 467–510, 2003, doi: 10.1016/S0376-0421(03)00078-2.
- [45] A. Sciacchitano, "Uncertainty quantification in particle image velocimetry," *Meas. Sci. Technol.*, vol. 30, no. 9, 2019, doi: 10.1088/1361-6501/ab1db8.
- [46] L. H. Benedict and R. D. Gould, "Towards better uncertainty estimates for turbulence statistics," *Exp. Fluids*, vol. 22, no. 2, pp. 129–136, 1996, doi: 10.1007/s003480050030.
- [47] A. Sciacchitano and B. Wieneke, "PIV uncertainty propagation," *Meas. Sci. Technol.*, vol. 27, no. 8, 2016, doi: 10.1088/0957-0233/27/8/084006.
- [48] Ishihara, T., Yamaguchi, A., & Fujino, Y. (2004). Development of a new wake model based on a wind tunnel experiment. *Global wind power*, 6.

- [49] Bastankhah M and Porté-Agel F 2014 A new analytical model for wind-turbine wakes *Renew. Energy* 70 116–23
- [50] A. Niayifar and F. Porté-Agel, “A new analytical model for wind farm power prediction,” *J. Phys. Conf. Ser.*, vol. 625, no. 1, 2015, doi: 10.1088/1742-6596/625/1/012039.
- [51] Göçmen T, Van der Laan P, Réthoré PE, Diaz AP, Larsen GC, Ott S (2016) Wind turbine wake models developed at the technical university of denmark: a review. *Renew Sust Energy Rev* 60:752–769
- [52] Stein, V. P., & Kaltenbach, H. J. (2016, September). Wind-tunnel modelling of the tip-speed ratio influence on the wake evolution. In *Journal of Physics: Conference Series* (Vol. 753, No. 3, p. 032061). IOP Publishing.

APPENDICES

A. Appendix Title

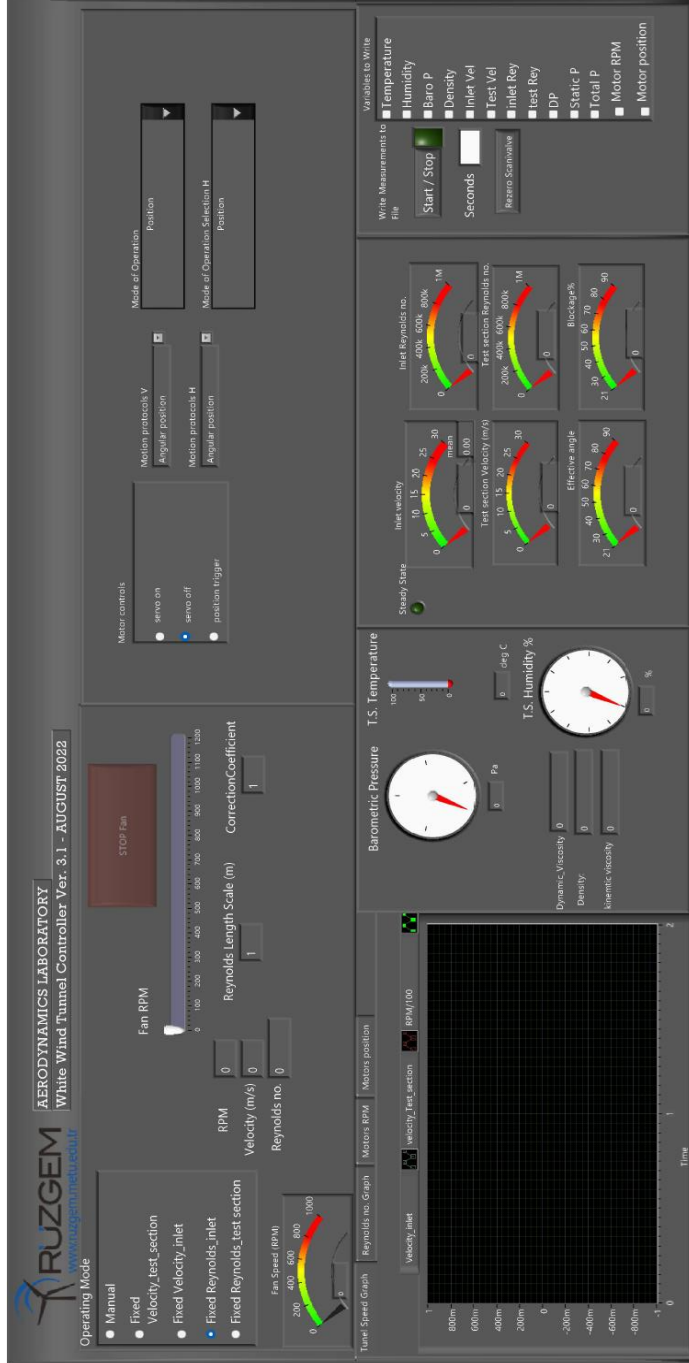


Figure A.1 The graphical user interface of the wind tunnel control software.

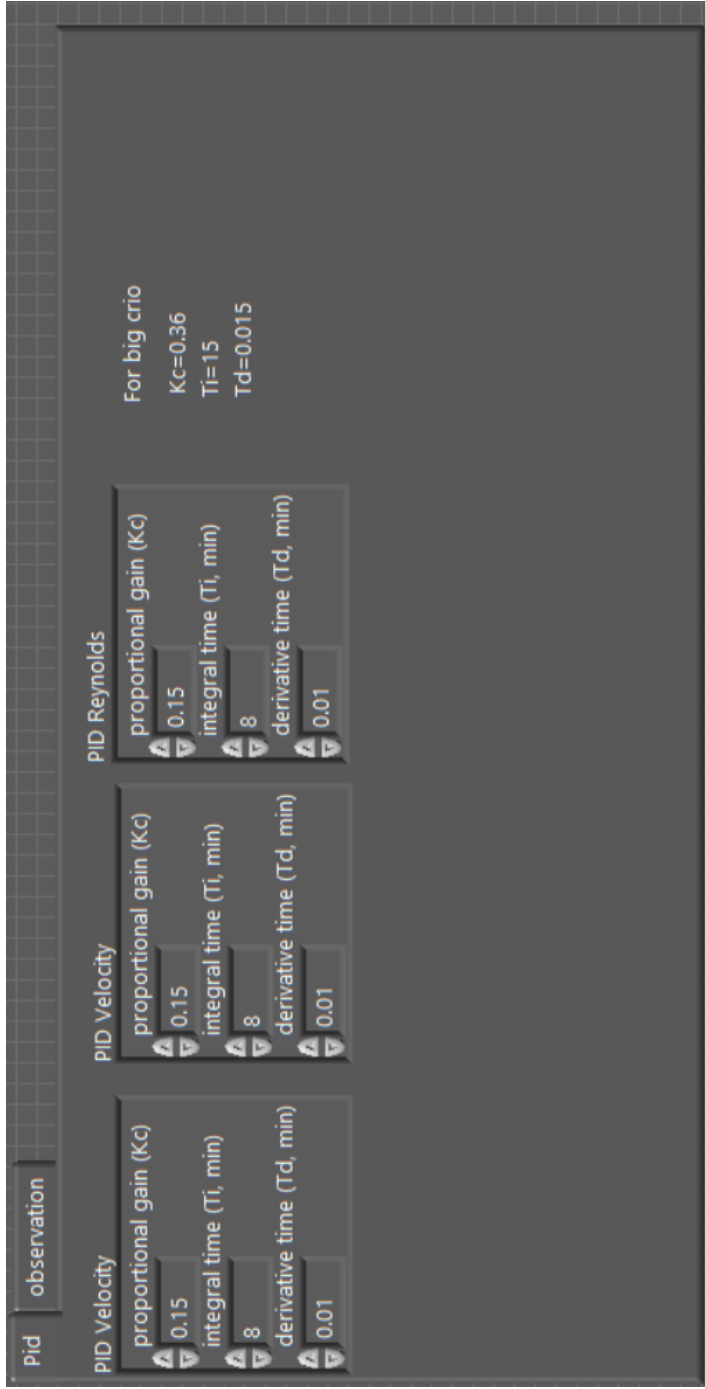


Figure A.2 The Tunnel Real-time control software.

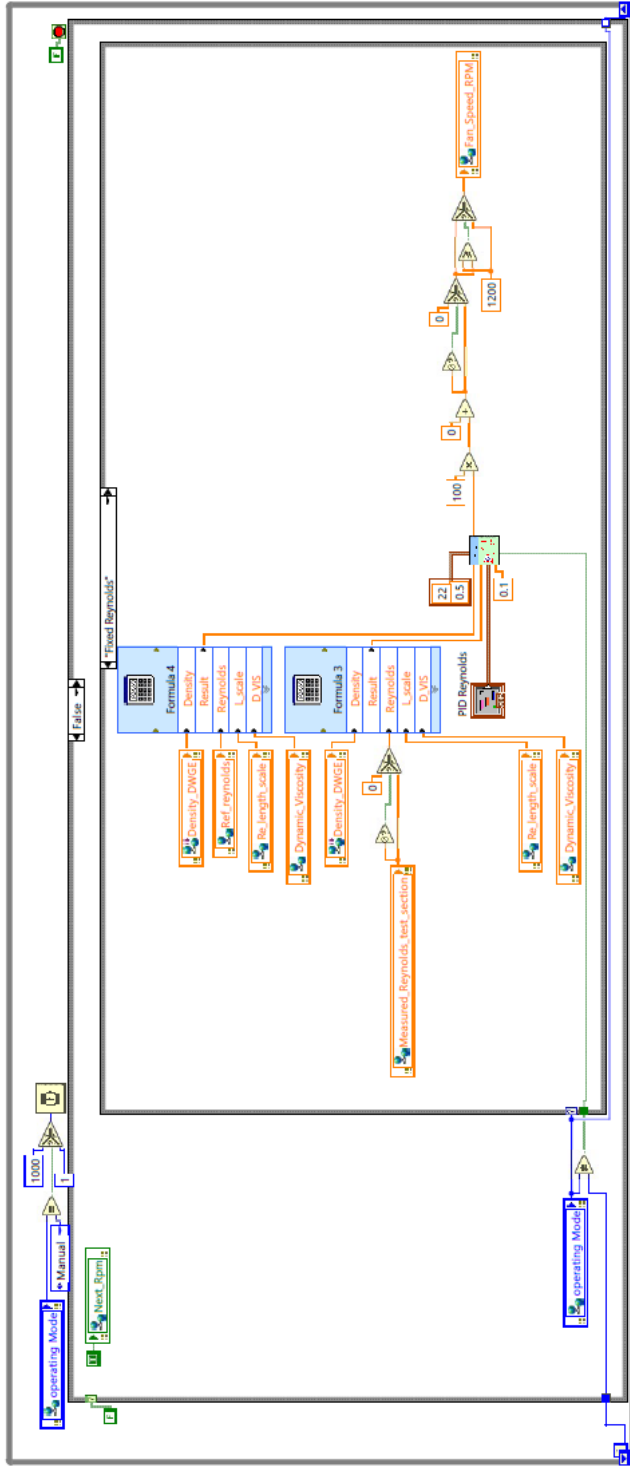


Figure A.3 The PID loop within the Real-time tunnel control software.

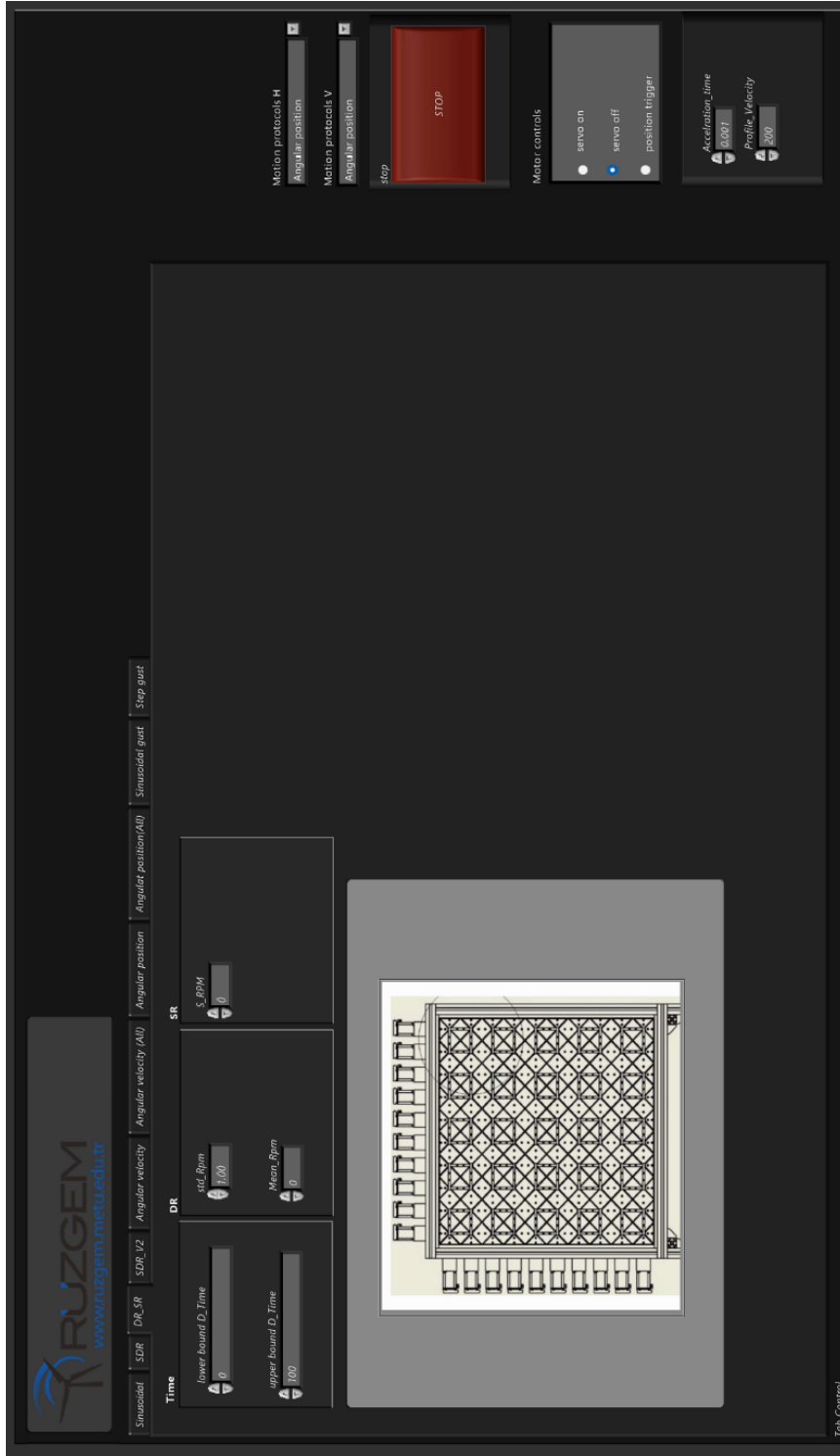


Figure A.4 The graphical user interface of the active grid motion control software for the random asynchronous modes.

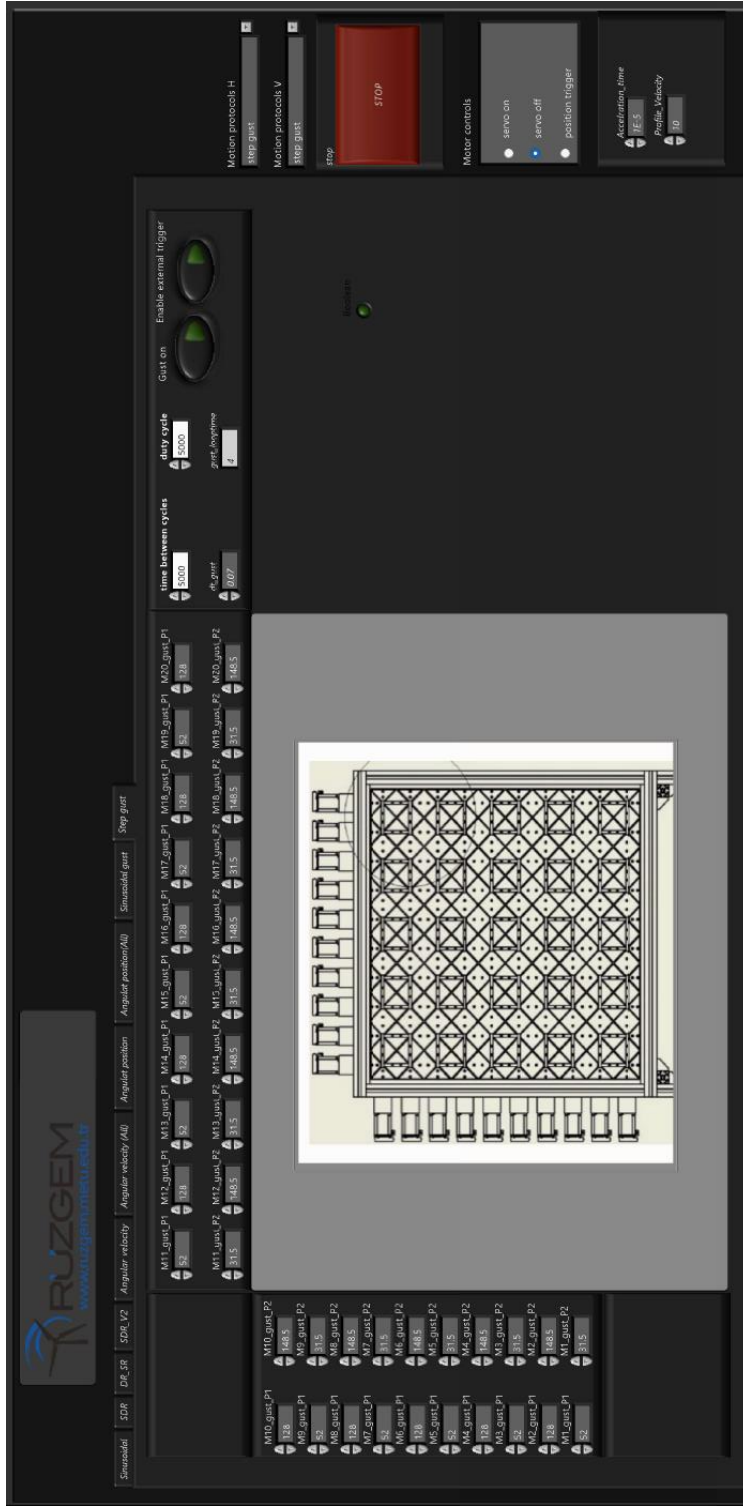


Figure A.5 The graphical user interface of the active grid motion control software for the step gust.

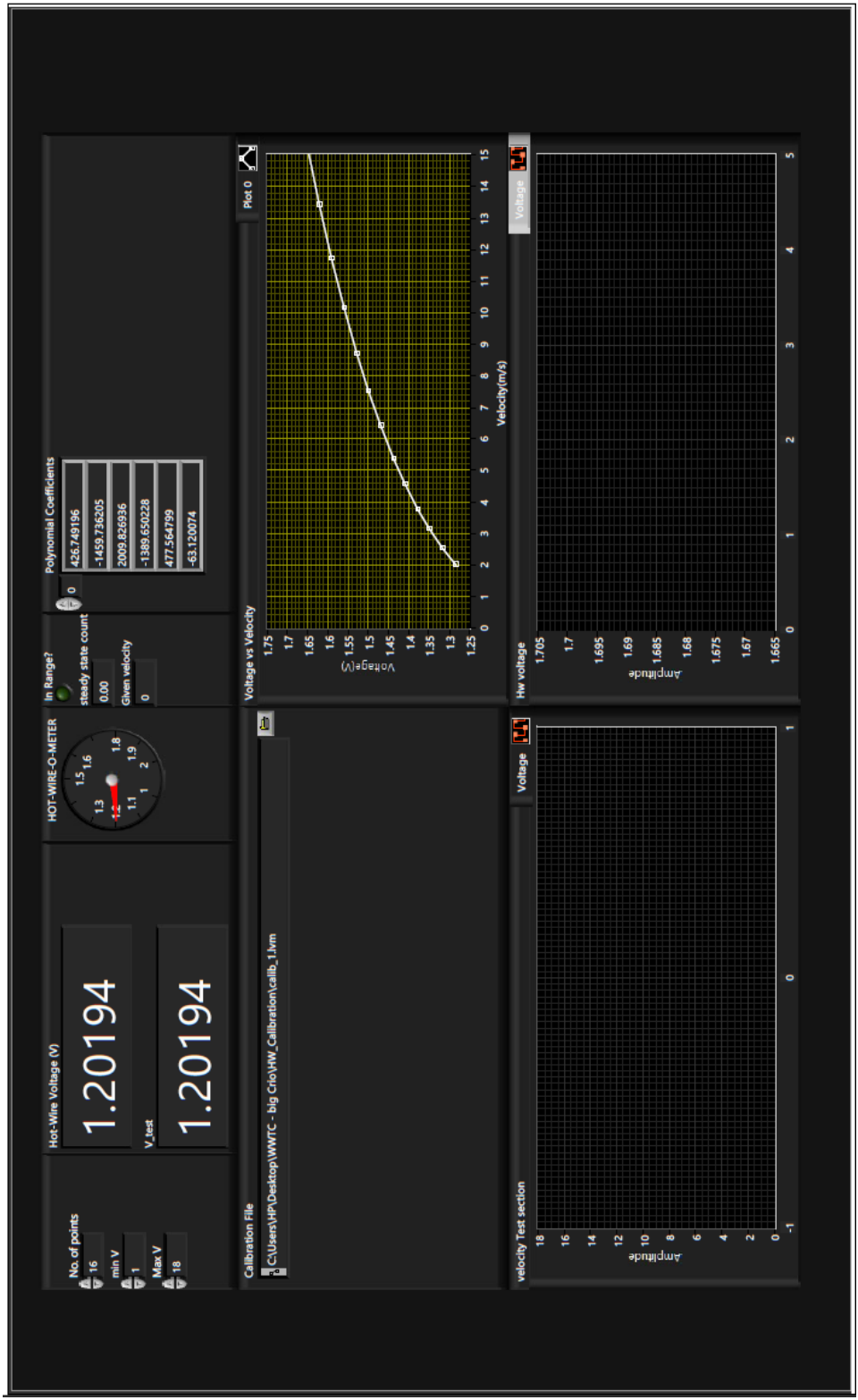


Figure A.6 The graphical user interface of the Hotwire calibration software.

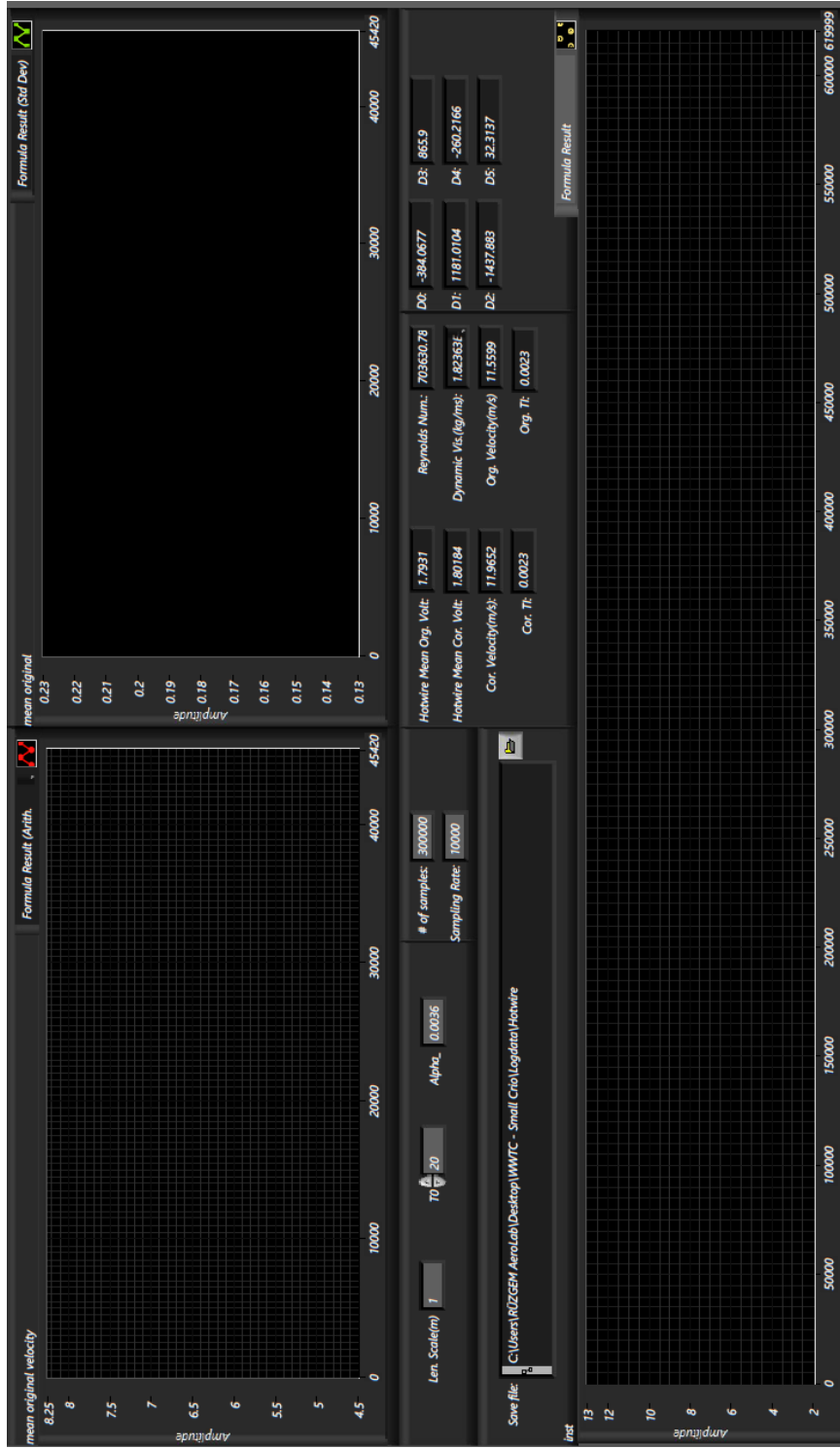


Figure A.7 The graphical user interface of the Hotwire measurement software.



Figure A.8 The graphical user interface of the Load measurement software.

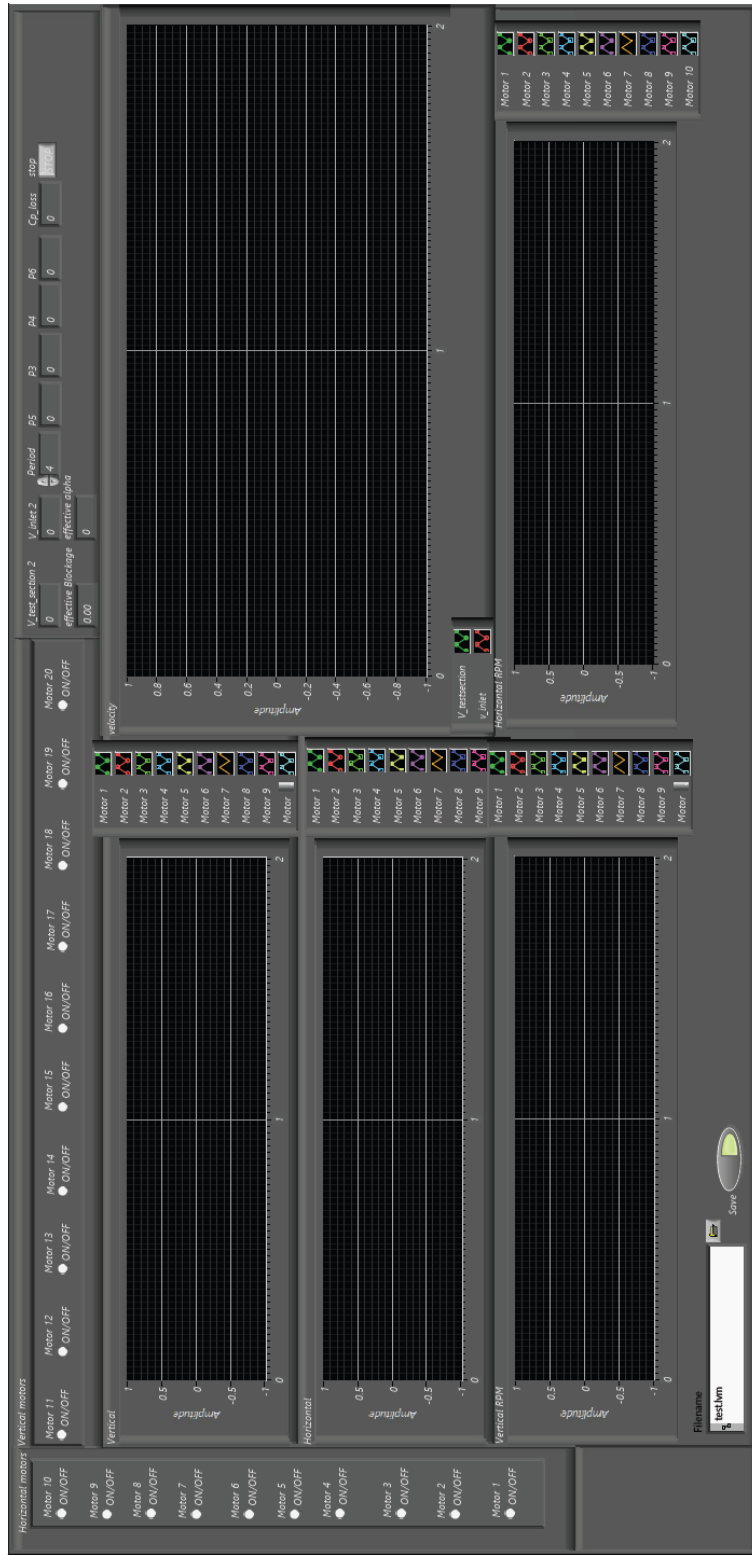


Figure A.9 The graphical user interface of the Flaps monitoring software.

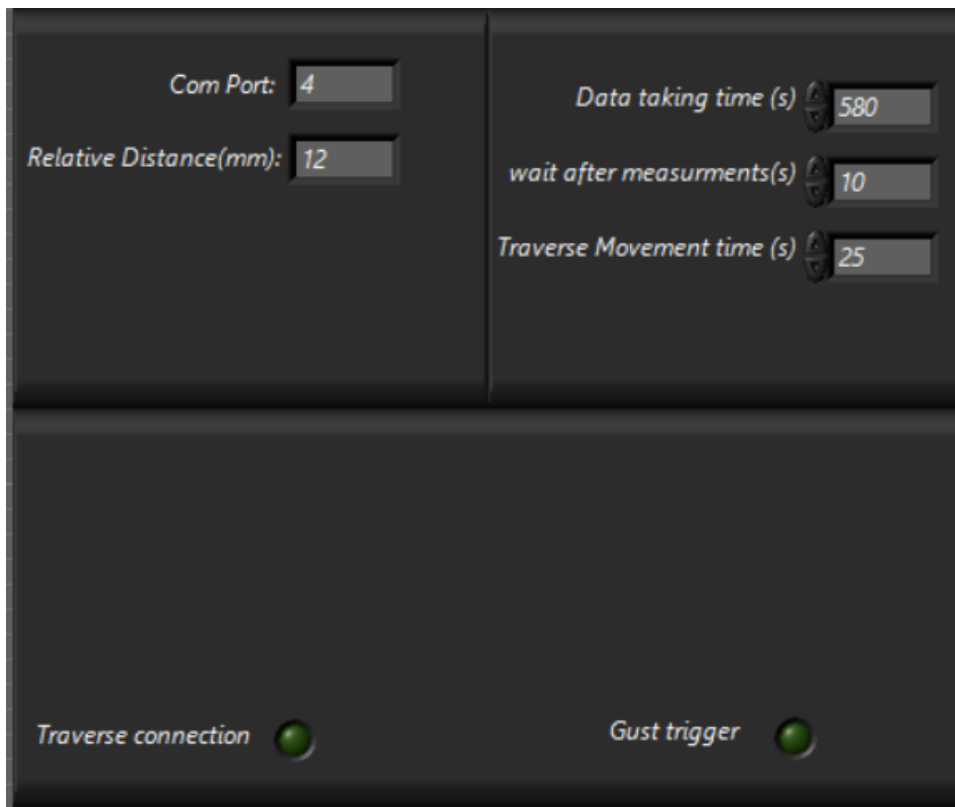


Figure A.10 The graphical user interface of the Automation software.

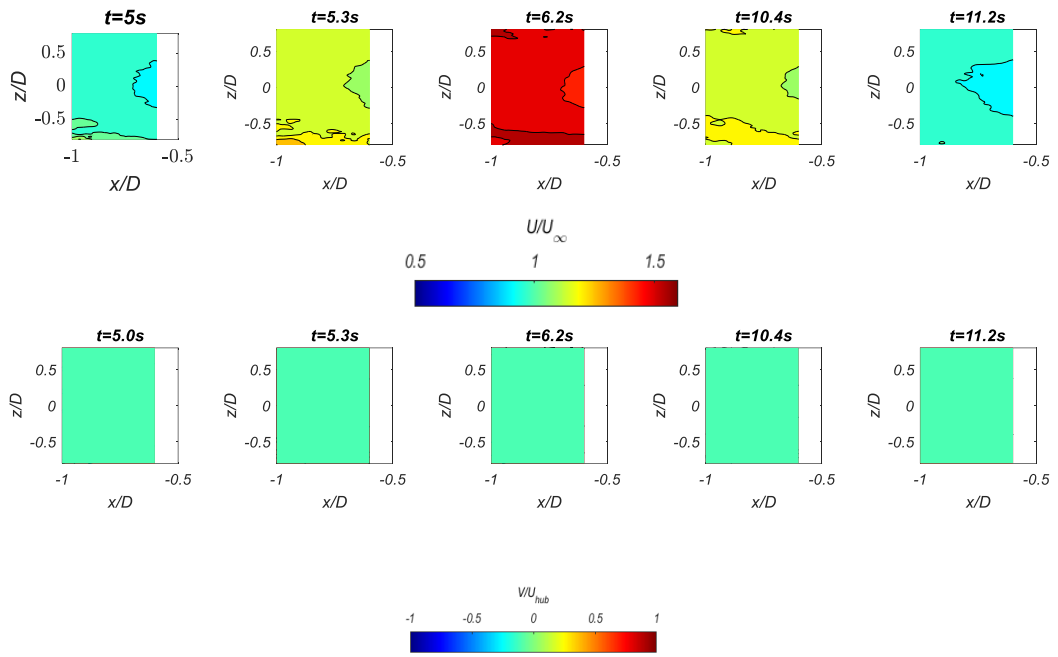


Figure A.11 Normalized stream wise and transverse velocity contour for top hat gust at different instances relative to the gust.